



Introduction of quasi-multilayer pulsed laser deposition for enhanced
superconducting properties of $\text{Ba}(\text{Fe}_{0.92}\text{Co}_{0.08})_2\text{As}_2$ thin films

Zur Erlangung des akademischen Grades eines
Doktors der Ingenieurwissenschaften (Dr.-Ing.)

von der KIT-Fakultät für Elektrotechnik und Informationstechnik des

Karlsruher Instituts für Technologie (KIT)

angenommene

Dissertation

von

M. Sc. Sven Meyer

geboren am 8. Januar 1988

in Recklinghausen

Hauptreferent: Prof. Dr. Bernhard Holzapfel

Korreferent: Prof. Dr. Kazumasa Iida

Tag der Promotionsprüfung: 03.12.2020

Kurzfassung

Diese Arbeit befasst sich mit der Implementierung von künstlichen Pinningzentren durch den Einsatz der Quasi-Mehrschichttechnik für die gepulste Laserabscheidung (PLD) in Kobalt (Co)-dotierten BaFe₂As₂ (Ba122)-Verbindungen. Das Ziel hierbei ist die Erhöhung der kritischen Stromdichten und der Pinningkräfte, welche entscheidende Parameter für elektrische Anwendungen sind, denn sie geben den Strom an, den diese Verbindungen in einem Magnetfeld führen können, ohne ihre supraleitenden Eigenschaften zu verlieren. Quasi-multilagige Schichten mit Perowskit-Pinningzentren aus BaHfO₃ (BHO) und BaZrO₃ (BZO), die mittels PLD hergestellt wurden, sind bereits für YBa₂Cu₃O₇-Verbindungen (YBCO) untersucht worden [1, 2]. Durch die Optimierung des epitaktischen Wachstums von Ba122-Verbindungen, wurde ein reproduzierbarer Prozess zum Experimentieren mit verschiedenen Mengen an künstlichen Pinningzentren etabliert, um eine - für den experimentellen Aufbau - optimale Ba122-Schicht ohne intrinsische Pinningzentren, wie Gitterdefekte oder Fremdphasen, zu erhalten.

Aufgrund der weniger intrinsischen Pinningzentren, hoher kritischer Stromdichten und kritischer Temperaturen von 20 K und einfach zu handhabenden Abscheidungstemperaturen von 700 °C, erwies sich Co-dotiertes Ba122 als bestgeeignetes Material für diesen Zweck. Phosphor (P)-dotiertes Ba122 zeigte Fremdphasen und Ausscheidungen an der Oberfläche, die als intrinsische Pinningzentren wirken. Obwohl die kritische Temperatur höher ist als bei Co-dotiertem Ba122, konnte die optimale Abscheidungstemperatur von 1050 °C zur Erzielung der Reproduzierbarkeit nicht durch die Substratheizung erreicht werden.

Ein weiterer beeinflussender Faktor auf das Wachstum ist das Substrat und seine Eigenschaften. Mehrere einkristalline Substrate mit einer Größe von 1 x 1 cm wurden auf ihre Eignung hin untersucht. Co-dotierte Schichten, die auf CaF₂ aufgewachsen wurden, zeigten die besten Ergebnisse unter Berücksichtigung der kritischen Temperatur, der kritischen Stromdichte und der geringen Menge an intrinsischen Pinningzentren. MgO war aufgrund niedriger Reproduzierbarkeitsraten kein geeigneter Kandidat als Substrat für optimales Wachstum, ebenso wenig wie LaAlO₃ (LAO) aufgrund hoher Mengen an intrinsischen Pinningzentren, verursacht durch Kristallzwillinge auf der Substratoberfläche. Die Laserparameter für das beste erreichbare Wachstum wurden auf 30 mJ (bzw. 3,0 J/cm²) und eine Repetitionsrate von 10 Hz eingestellt. Auf der Grundlage mehrerer Versuchsreihen mit unterschiedlichen Pulsanzahlen und Targetwechseln, wurde der Fokus dieser Arbeit auf die Implementierung von BHO als künstliches Pinningmaterial gerichtet, da BZO bereits in mehreren Studien untersucht worden ist, obwohl

die untersuchten Schichten nicht mit Quasi-Multilagen-Technik gewachsen wurden. Die beste Konfiguration der Quasi-Multilagen-Technik wurde bei 12 BHO-Pulsen pro Quasi-Schicht und einer Gesamtanzahl von 18.000 Pulsen auf dem Co-dotierten Ba122-Target erreicht. Die Anzahl der Targetwechsel unterschieden sich bei den untersuchten Proben, um die Menge des künstlichen Pinning-Materials mit einer möglichst gleichmäßigen Verteilung in der Schicht einzustellen.

Die untersuchten Proben wiesen 0 Mol-%, 1,03 Mol-%, 1,59 Mol-% und 3,85 Mol-% BHO auf. Diese Gehalte wurden mit induktiv gekoppelter Plasma-Massenspektrometrie (ICP-MS) gemessen.

Sowohl die kritische Stromdichte als auch die Pinningkraftdichte konnten auf 10^6 A/cm² bzw. 50,6 GN/m³ für den höchsten getesteten Dotierungsgrad erhöht werden.

Weitere Untersuchungen zeigten, dass für niedrigere Dotierungsniveaus Nanopartikel und Nanosäulen für das Pinning verantwortlich waren. Mit zunehmendem Dotierungsgrad traten mehr Nanosäulen auf. Die Nanosäulen konnten durch energiedispersive röntgenspektroskopische Messungen (EDX) als BHO identifiziert werden.

Vergleichbare Experimente mit vergleichbaren, auf LAO gewachsenen Schichten zeigten ein erwartetes Verhalten. Die kritischen Stromdichten und Pinningkraftdichten streuten aufgrund des starken intrinsischen Pinning im Co-dotierten Ba122. Die zusätzlichen künstlichen Pinningzentren führten zu mehr Störungen im Gitter, ohne die supraleitenden Eigenschaften zu verbessern.

Diese Untersuchungen wurden mit der Implementierung von InAs als künstliches Pinning-Material wiederholt. Der Sphalerit-Halbleiter InAs wurde bisher noch nie als künstliches Pinning-Material untersucht. Um die optimale Zusammensetzung zu erhalten, wurden verschiedene Untersuchungsreihen durchgeführt.

Für die beste Zusammensetzung wurden 39 Targetwechsel durchgeführt, wobei nur die Anzahl der Laserpulse auf InAs verändert wurde, die zwischen 10 und 30 Pulse pro Wechsel lag.

Der Gehalt des Pinning-Materials der vorherigen Experimenten konnte nicht reproduziert werden, da der Gehalt an InAs, gemessen durch ICP-MS, nicht mit der Anzahl der Laserpulse korrelierte. Eine mögliche Erklärung ist die Bildung von Droplets auf der Oberfläche der Schicht. Ein weiterer Grund können die großen Agglomerationen von InAs sein, die nicht Teil des Pinning-Mechanismus sind, aber in den ICP-Messungen angezeigt werden. Transmissive Elektronenmikroskopie (TEM) konnte kein InAs in der Schicht nachweisen, was möglicherweise auf die Flüchtigkeit von InAs unter Elektronenbeschuss zurückzuführen ist. Die kritischen Stromdichten zeigten ein Maximum bei 468 InAs-Pulsen.

Es wurde festgestellt, dass der Pinning-Mechanismus durch Punktdefekte verursacht wird, die jeweils nur mit einer Flusslinie interagieren können. Daher führte ein Anstieg des InAs-Gehalts in der Schicht zu einer zunehmenden Anzahl von Punktdefekten, die mit einer Flusslinie interagieren, bis ein Optimum der kritischen Stromdichte erreicht wird. Jenseits dieses Optimums verursachte der zunehmende InAs-Gehalt lediglich Un-

ordnung im Gitter und die kritische Stromdichte nahm wieder ab.

Abstract

This work focuses on the implementation of artificial pinning centers by deploying the quasi-multilayer technique for pulsed laser deposition (PLD) in cobalt (Co)-doped BaFe_2As_2 (Ba122) compounds. The objective of this is to enhance the critical current densities and the pinning forces, which are crucial parameters for electrical applications, as they indicate the current these compounds can carry in a magnetic field, without losing their superconducting properties. Quasi-multilayered films with perovskite pinning centers consisting of BaHfO_3 (BHO) and BaZrO_3 (BZO) made via PLD have been already investigated for $\text{YBa}_2\text{Cu}_3\text{O}_7$ -compounds (YBCO) [1, 2]. By optimizing the epitaxial growth of Ba122 compounds, a reproducible process for experimenting with various amounts of artificial pinning centers was established, in order to obtain the optimal possible Ba122 film for the experimental setup, without intrinsic pinning centers, such as lattice defects or foreign phases.

Co-doped Ba122 proved to be the most suitable candidate, exhibiting less intrinsic pinning centers, high critical currents and critical temperatures of 20 K and easy-to-handle deposition temperatures of 700 °C. Phosphorus (P)-doped Ba122 showed foreign phases and precipitates at the surface acting as intrinsic pinning centers. Although its critical temperature is higher than for Co-doped Ba122, the substrate heater could not provide the optimal deposition temperature of 1050 °C, in order to obtain reproducibility.

As the growth also depends on the substrate and its properties, several single-crystalline substrates with a size of 1 by 1 cm were investigated towards their suitability. Co-doped films grown on CaF_2 showed the best results considering critical temperature, critical current density and low amount of intrinsic pinning centers. MgO was not a suitable candidate as a substrate for optimal growth due to low reproducibility rates as well as LaAlO_3 (LAO) due to high amounts of intrinsic pinning centers, caused by crystal twins on the substrate surface. The laser parameters for best achievable growth were set to 30 mJ (respectively 3.0 J/cm²) and a repetition rate of 10 Hz. Subsequent to various experiments with different numbers of pulses and target exchanges, the decision was made to focus on the implementation of BHO as the artificial pinning material, since BZO had already been investigated, although the investigated samples were not grown with quasi-multilayer technique. The best configuration was found at 12 pulses of BHO for each quasi-layer and a total amount of 18,000 pulses on the Co-doped Ba122 target. The number of exchanges differed from sample to sample in order to adjust the amount of artificial pinning material with a preferably equal distribution in the film.

The investigated samples exhibited 0 mol%, 1.03 mol%, 1.59 mol% and 3.85 mol% of BHO. These contents were measured with inductively coupled plasma mass spectrometry (ICP-MS).

The critical current density as well as the pinning force density could be enhanced to 10^6 A/cm² respectively 50.6 GN/m³ for the highest tested doping level.

Further investigations proved that nano-particles asided by nanocolumns were responsible for the pinning in lower doping levels. With increasing doping levels, more nanocolumns appeared. The nanocolumns could be identified to consist of BHO by energy dispersive X-ray spectroscopy measurements (EDX).

Identical experiments with identical films grown on LAO showed an expected behavior. The critical current densities and pinning force densities scattered due to strong intrinsic pinning in the Co-doped Ba122. The additional artificial pinning centers led to more disturbance in the lattice, without enhancing the superconducting properties.

These investigations were repeated with the implementation of InAs as the artificial pinning material. The sphalerite semiconductor InAs has never been investigated before as an artificial pinning material. Several experiments were performed to obtain the optimal composition. For the best composition, 39 target exchanges were performed, only changing the number of pulses on InAs, ranging between 10 and 30 pulses per exchange.

The contents of pinning material of the previous experiments could not be reproduced due to contents of InAs measured by ICP-MS, which were not corresponding to the number of pulses. A possible explanation was the formation of droplets on the surface or large agglomerations of InAs, which were not part of the pinning mechanism but were displayed in the ICP measurements. Transmissive electron microscopy (TEM) could not show any InAs in the film, which may be due to the volatility of InAs under electron bombardment. The critical current densities showed a maximum at 468 pulses of InAs.

It was found that the pinning mechanism was caused by point defects, which can only interact with solely one flux line at a time. Hence, an increase of InAs content in the film resulted in an increasing number of point defects interacting with one flux line, until an optimum of critical current density was reached. Beyond this optimum, the increasing InAs content solely caused disorder in the lattice and the critical current density decreased again.

Contents

1	Introduction	1
1.1	Motivation	1
1.2	Background of superconductivity, pinning and growth	5
1.2.1	Fundamentals of superconductivity	5
1.2.1.1	Type I superconductor	5
1.2.1.2	Type II superconductor and pinning	8
1.2.1.3	Pinning	9
1.2.1.4	Anisotropy measurements	10
1.2.1.5	Determination of flux pinning mechanisms in type II superconductors after Dew-Hughes	11
1.2.2	Technical applications for superconductors	12
1.2.3	Ba122	16
1.2.4	Epitaxy and growth	19
1.2.4.1	Ba122 film growth	21
1.2.4.2	Substrates	21
1.3	Preparation and experimental setups	23
1.3.1	Target preparation and properties	23
1.3.1.1	Ba122	23
1.3.1.2	BaZrO ₃ (BZO)	23
1.3.1.3	BaHfO ₃ (BHO)	23
1.3.1.4	InAs	24
1.3.2	Pulsed laser deposition (PLD)	24
1.3.2.1	Quasi-multilayer technique	26
1.3.3	Chemical etching	27
1.4	Characterization	28
1.4.1	Physical property measurement system (PPMS)	28
1.4.2	X-ray diffraction (XRD)	29
1.4.3	Scanning electron microscopy (SEM)/energy dispersive X-ray spec- troscopy (EDX)/transmission electron microscopy (TEM)	31
1.4.4	Atomic force microscopy (AFM)	33
1.4.5	Inductively coupled plasma mass spectrometry (ICP-MS)	34
2	Experimental results	35
2.1	Experimental realization	35

2.2	PLD of Ba122 films with frequency tripled Nd:YAG laser	36
2.2.1	Formation of Fe interlayer	36
2.2.2	Irreproducibility on MgO	41
2.2.3	LAO and CaF ₂ as substrates	42
2.2.4	Conclusion	45
2.3	Pulsed Laser Deposition of quasi-multil. supercond. Ba(Fe _{0.92} Co _{0.08}) ₂ As ₂ - BaHfO ₃ and Ba(Fe _{0.92} Co _{0.08}) ₂ As ₂ - BaZrO ₃ nanocomposite films	47
2.3.1	Experiments for optimization of homogenous distribution of BHO nanoparticles on CaF ₂	50
2.3.2	Experiments for optimization of homogenous distribution of BHO nanoparticles on LAO	63
2.3.3	Conclusion	66
2.4	Ba122 with incorporated InAs	70
2.4.1	Conclusion	79
3	Summary	81
4	Outlook	85
	Bibliography	87

1 Introduction

1.1 Motivation

An exciting development in solid state physics was the discovery of the iron-based superconductors (FBS) by Kamihara et al. [3] with transition temperatures up to 55 K in 2008 for fluorine (F)-doped LaOFeAs. It was believed that iron based superconductors would not be possible since the magnetic properties of the included iron would cause Cooper pairs to spin flip and therefore destroy possible superconductivity.

After the discovery of FBS, more and more reports of other FBS compounds were issued. The iron-based class of superconductors is basically divided into so-called families such as “11” (e.g. FeSe, FeTe), “111” (e.g. LiFeAs), “122” (e.g. BaFe₂As₂, SrFe₂As₂), “1111” (e.g. LaOFeAs, NdOFeAs) [4] (for an overview see fig. 1.1).

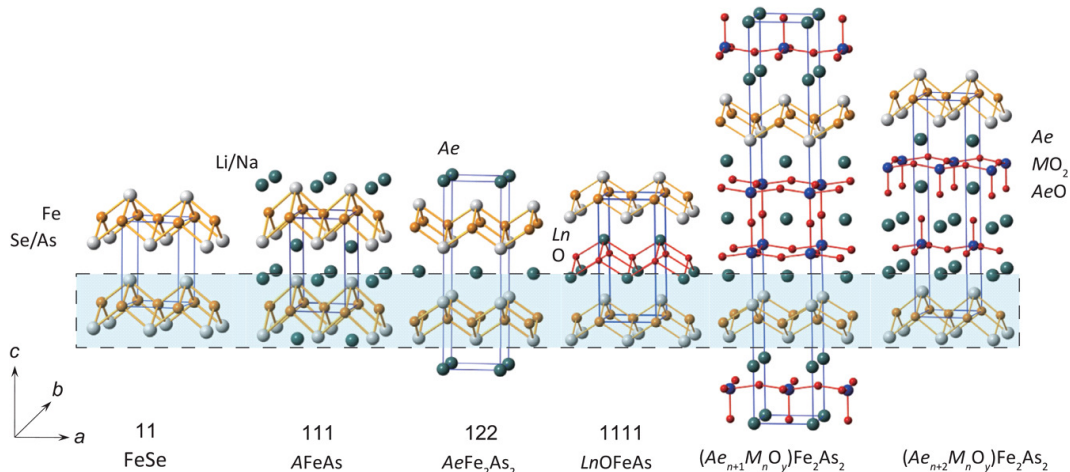


Figure 1.1: Schematic view of the crystal structures for several types of iron-based superconductors, in which A, Ae, Ln, and M stand for alkali, alkali-earth, lanthanide, and transition metal atoms [5].

In these compounds tetrahedrally ordered layers of iron (Fe) and phosphorus (P), arsenic (As), selenium (Se) or tellurium (Te) are characteristic. In the class of iron-based superconductors these layers, e.g. FeAs or FeSe layers (in fig. 1.1 indicated by the light blue area) [6, 7], carry the superconductivity comparable to CuO planes in cuprates. With their properties, they can be seen as in between cuprates (layer-type crystal structure, high upper critical fields, 2D-behaviour [7]), the low temperature superconductors (LTS), such as NbTi and Nb₃Sn [8] (few thermal fluctuations, low anisotropies [9]) and magnesium diboride (MgB₂) (multi-band superconductivity [10]). BaFe₂As₂ (Ba122)

compounds are quite stable in air or water vapor [11]. Ba122 shows high crystalline quality such as flat surface and a sharp transition of the critical temperature $\Delta T_c = 1.1 - 1.3$ K. Critical current density (j_c) values up to 4 MA/cm² for cobalt (Co)-doped Ba122 on (La,Sr)(Al,Ta)O₃ (LSAT) and magnesium oxide (MgO) were reported [12, 13].

It is this combination of different properties, especially low anisotropies and high critical fields, which makes iron-based superconductors interesting candidates for high field applications such as wires and tapes for superconducting magnets and coils.

To realize these applications, the production of long tape samples must be reliable and affordable, flux pinning mechanisms must be understood correctly and the transport properties must be adjustable to all needs of applications. The research is still in its infancy, requiring several model experiments on thin films which are not possible in bulk samples and can be upscaled and transferred to electronic applications. Applications that have already been produced and examined are superconducting wires and tapes using the powder-in-tube (PIT) technology. For potassium (K)-doped Ba122 (Ba122:K) [14, 15], Co-doped Ba122 (Ba122:Co or Co:Ba122) [16] wires the critical current density values in a magnetic field are already above the critical application level for NbTi cables and coils used by CERN of 0.15 - 0.23 MA/cm² at operating temperatures of 4.2 K and magnetic fields of 4 respectively 6 T [17, 18]. Nevertheless, these values are still fairly low indicating the need for flux pinning improvement. An additional challenge is the stoichiometric distribution of volatile atoms such as fluorine and potassium. These elements tend to distribute unequally in the film causing a decrease of superconducting properties due to lattice defects.

A solution model-system for pinning improvement is the realization and characterization of nano-structured thin films, because of its multi-phased, self-organizing heteroepitaxial layer growth, as seen in Ba122 films. The growth mode of Ba122 films is -under right conditions- a layer growth mechanism with $c/2$ -ledges [19]. Additionally, it does not contain volatile atoms such as potassium or fluorine and is therefore optimal for quasi-multilayer deposition with equally distributed nanoparticles between closed layers of superconducting compound. The synthesis and characterization of effective pinning centers by targeted insertion of nanoscale defect structures in epitaxial thin films is an essential, central goal of this work.

Co-doped Ba122 films exhibit relatively high j_c values above 1 MA/cm² at 4.2 K without applied external magnetic field due to low misorientation angles at grain boundaries [20]. However, j_c decreases rapidly in applied magnetic fields. To avoid this effect, it is therefore necessary to pin flux lines within the superconductor. In order to achieve that the quasi-multilayer pulsed laser deposition is deployed. This technology enables growing single material films, as well as multilayered and quasi-multilayered films, in combination with a buffer layer. The quasi-multilayer technique is used e.g. for implementing nanoparticles as pinning centers. When a high energetic, pulsed and focused laser beam hits a target of the deposition material, the irradiation of the laser beam leads to a strong local heating and ablation of the target material. The target material

is accelerated towards a substrate and condenses on its surface, creating a thin film. Several targets can be switched during the process. A shutter allows precise adjustment of the number of pulses even down to a single pulse and shuts the laser beam during target switch. Thus, this technique enables the deposition of closed layers of the superconducting material and non-closed layers of the pinning material in between the superconducting layers, in order to achieve equally distributed nanoparticles as pinning centers.

Quasi-multilayered films made via pulsed laser deposition (PLD) with two targets by implementing nanoparticles of BaHfO₃ (BHO) [21, 22] or BaZrO₃ (BZO) [1, 2] have been already reported for YBa₂Cu₃O₇-compounds (YBCO) to increase critical current density j_c and pinning force density F_P .

Films made with pre-mixed Co-doped BaFe₂As₂ (Ba122)/BZO targets were also already studied [23] and published in 2017 as well as films with pre-mixed P-doped Ba122 and BZO targets [20, 24]. These investigation show promising results for the increase of pinning force density and therefore critical current density with values of 170 GN/m³ for 2 mol% and 30 GN/m³ for 4 mol% at 11 T and 4.2 K for BaZrO₃-added Ba(Fe,Co)₂As₂ [23] and 58 GN/m³ at 9 T and 5 K for BaZrO₃-added BaFe₂(As,P)₂ films [20] and recently 189 GN/m³ at 9 T and 4 K [24].

In this study, the multi-target technique for the fabrication of Ba122 thin films is combined with the usage of different perovskites such as BZO, BHO and the sphalerite semiconductor InAs as nanoparticle material since this has the advantage of easy adjustment and control of the doping level during deposition. BHO and BZO are structurally very similar and have already been investigated as artificial pinning centers in YBCO compounds using the quasi-multilayer technique. This technique, however, has never been investigated in Ba122.

InAs has never been used before as a pinning material providing beneficial As for possible As loss during deposition acting as intrinsic pinning centers [25]. In the well investigated Ba122 compounds Ba(Fe,Co)₂As₂ and BaFe₂(As,P)₂ are suitable model systems for those investigations due to their heteroepitaxial layer growth with low misorientation angles at grain boundaries and few intrinsic defects, high critical temperatures, high critical current densities and low anisotropies.

This work is structured as follows.

Chapter 1 introduces the fundamentals and the physical background of superconductivity, pinning, thin film growth and material properties.

In the middle part of chapter 1, the preparation of the PLD targets is explained, followed by a brief introduction of the experimental setup and method of the pulsed laser deposition. The last part of this chapter provides an insight into the process of structuring the samples, which is crucial for the measurement of electrical transport properties.

Chapter 2 introduces the experimental stages, characterizations and investigations of this work - from optimization of Ba122 growth to implementation of perovskites

and InAs as artificial pinning centers, with the objective to achieve improved electrical transport properties. In the beginning, the experimental realization and the first steps towards reproducible growth of Ba122 samples is explained. Thereafter, the first experiments with implementation of BHO and BZO as pinning material, the optimization and also in comparison for different substrates are presented. Finally, the experiments of the implementation of InAs as pinning center material and the associated investigations are described.

Chapter 3 retrospects this thesis and connects the different topics, thereby summarizing the findings of this work with regards to improvements for future electrical applications and investigations of these.

Finally, chapter 4 presents an outlook of possible improvements and further investigations as well as practical applications of the findings of this work.

1.2 Background of superconductivity, pinning and growth

The research performed in this work focused on the introduction of the quasi-multilayer technique in combination with Ba122 superconductor thin films implementing artificial pinning centers for improvement of electrical transport properties of these films towards possible applications.

This chapter gives a general introduction to the fundamentals and the physical background of superconductivity, thin film growth and material properties, which are crucial for the understanding of the scope of this work.

1.2.1 Fundamentals of superconductivity

The effect of superconductivity was discovered in 1911 by Heike Kamerlingh Onnes. He found that the resistance of mercury decreased to immeasurable values below a temperature of ca. 4 K. This temperature is called critical temperature T_c .

In the superconducting state an external magnetic field will be ejected from the material (Meissner-Ochsenfeld-effect, discovered in 1933) due to shielding currents.

There are two types of superconductors depending on their behaviour in an external magnetic field.

1.2.1.1 Type I superconductor

In type I superconductors an external magnetic field will be displaced to a thin layer located at the surface of the material. So it is considered as a perfect diamagnet. This phase is called the Meissner-phase (see fig. 1.3). The thickness of this layer is named the London penetration depth λ .

For a type I superconductor temperatures above T_c , an external magnetic field above the critical magnetic field H_c or a current density above j_c cause break up of the cooper pairs which leads to a loss of the superconducting state. This is shown in the following figure 1.2

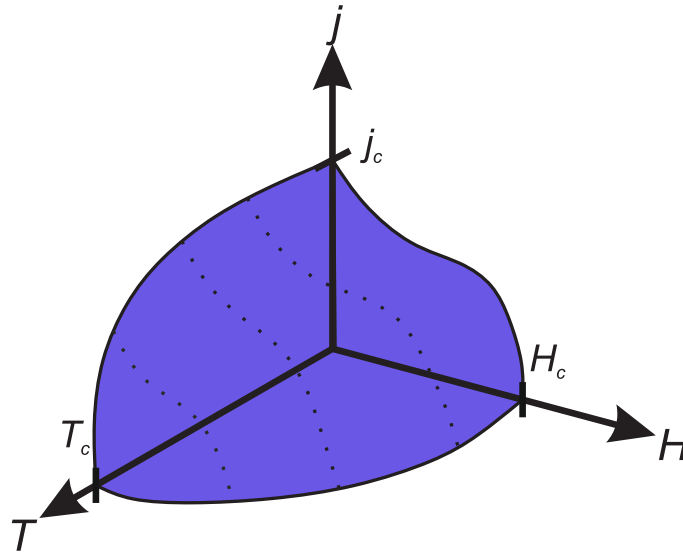


Figure 1.2: Phase diagram of a superconductor. The superconducting state vanishes when one parameter of temperature T , magnetic field H and current density j exceeds the blue colored volume. This image is based on [26].

E.g. a critical current density drives the electrons to move faster than the critical velocity causing the Cooper pairs to break up [27, p. 269].

The charge carriers in type I superconductors are so called Cooper pairs. Cooper pairs consist of two electrons with opposite spin and momentum, so a Cooper pair can be considered a boson and can be described by one macroscopic wave function.

Bosons are described by the Bose-Einstein-statistics, so all Cooper pairs travel with the same velocity and direction through the material. The distance over which the attractive interaction between the two electrons of a Cooper pair acts is called coherence length ξ .

To classify the two types of superconductors the relation of the London penetration depth λ and the coherence length ξ is used and called the Ginzburg-Landau parameter [28]:

$$\kappa = \frac{\lambda}{\xi}. \quad (1.1)$$

Superconductors type I exhibit a $\kappa < 1/\sqrt{2}$. Superconductors type II on the other hand show a $\kappa > 1/\sqrt{2}$.

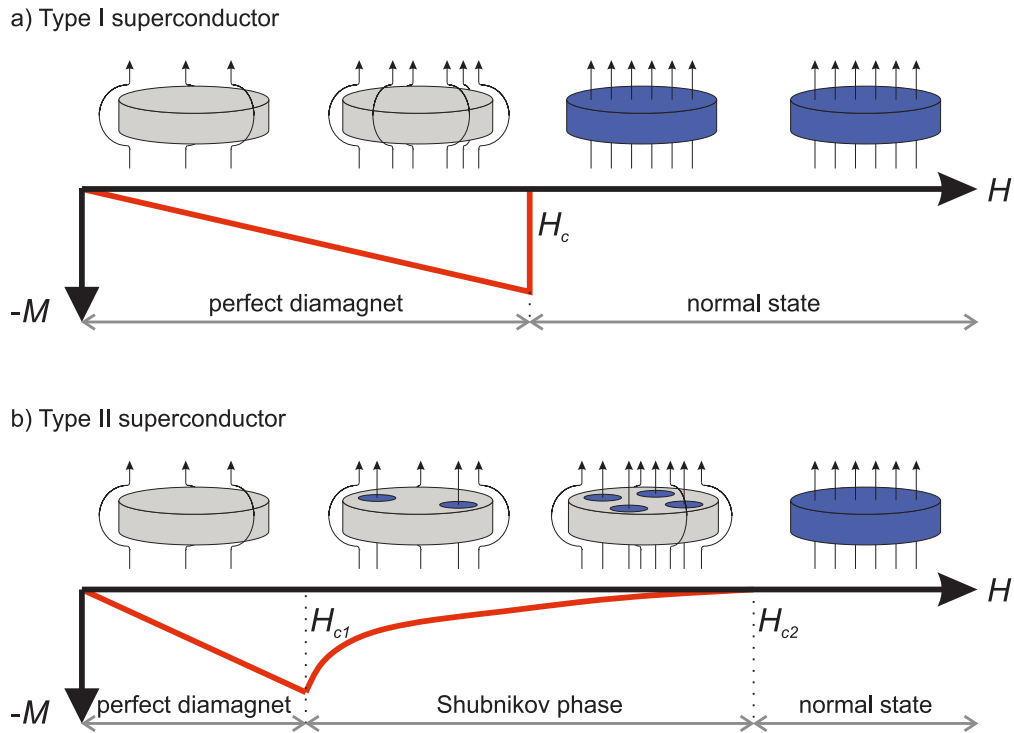


Figure 1.3: Difference in the magnetic behaviour for type I and type II superconductors. a) Type I superconductors are perfect diamagnets until a certain field strength is reached. At the critical magnetic field H_c superconductivity is destroyed and the flux penetrates the superconductor. b) Type II superconductors are perfect diamagnets until a certain magnetic field H_{c1} is reached. With increasing magnetic fields flux partially penetrates the superconductor (Shubnikov phase). The superconductivity collapses beyond a critical magnetic field H_{c2} . This image has been drawn after [29, p. 7].

1.2.1.2 Type II superconductor and pinning

Type II superconductors do not become normalconducting above an external critical magnetic field H_{c1} . Magnetic vortices start to penetrate the superconducting material (as shown in fig. 1.3) and the Cooper pair density at the location of a magnetic vortex decreases to zero. Shielding currents decelerate and focus the entering magnetic field lines to a flux line system in the shape of a triangular lattice (in an ideal homogenous superconductor type II).

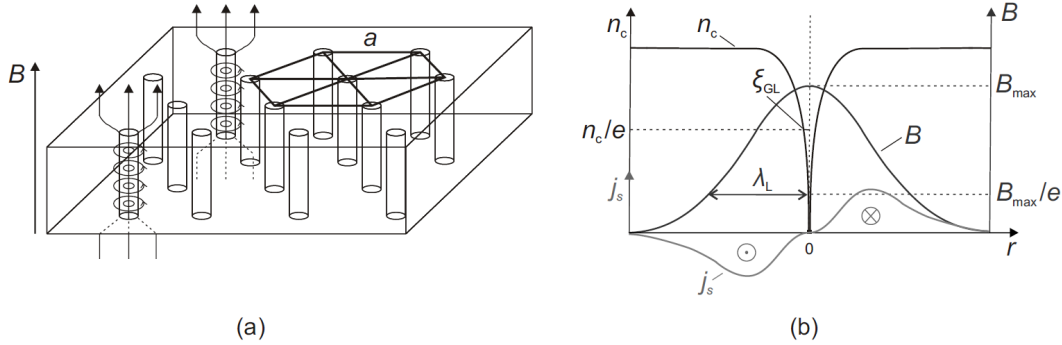


Figure 1.4: a) In the Shubnikov phase the vortices arrange in a hexagonal grid. Each flux line is surrounded by a circulating current, which shields the superconducting area from the normal conducting area. b) Local variation of Cooper pair density n_C , flux density B and super current density j_s around a vortex [30, p. 8].

Each magnetic vortex carries a magnetic flux quantum Φ_0 and is located at the corners of the already mentioned triangular lattice. The flux lines are surrounded by circulating currents, which together with an external magnetic field, generate a magnetic flux inside the flux line, thereby decreasing the magnetic field in between the flux line system. This is called the Shubnikov phase. If the external magnetic field increases, the distances between the flux lines decrease. A crucial parameter in the Shubnikov phase is the irreversibility field H_{irr} . Flux vortices start to move, the critical current density j_c reduces to zero but the superconductivity is still preserved. This phase is stable until a certain critical magnetic field H_{c2} is reached where superconductivity vanishes completely [27, p. 23].

When a current, with the density j , is applied to a superconductor in the Shubnikov phase, it creates a movement of the flux lines due to the Lorentz force

$$F_L = j \cdot \Phi_0 \cdot l \quad (1.2)$$

with the flux quantum

$$\Phi_0 = n \frac{h}{2e} \quad (1.3)$$

, where n is an integer, h is Planck's constant ($6.6207015 \cdot 10^{-34} \text{ J s}$) and e is the

elementary charge of $1.602176634 \cdot 10^{-19} C$ and the length l of the vortex, causing an electrical resistance. The movement of the flux lines causes Cooper pairs to break up and reassemble, which costs energy. To prevent the flux lines from moving the flux lines have to be pinned. This can be achieved by defects in the crystal lattice, grain boundaries with small angles, impurities or variations of the homogeneity. The diameter of flux vortices is in the range of the coherence length ξ of a material.

Larger defects will hinder the superconducting current flow.

A distinction must be made between intrinsic, growth-induced and extrinsic pinning [31]. Intrinsic pinning results from lattice properties itself, whereas growth-induced pinning results from lattice defects, small angle grain boundaries, precipitates, twin boundaries. Extrinsic pinning centers are intentionally included defects such as nanoparticles, secondary phases or impurities. High T_c superconductors show shorter coherence lengths than conventional superconductors [32], thus small spheric defects such as nanoparticles can already act as pinning centers.

1.2.1.3 Pinning

Implementing defects or material in the superconducting compound which locally destroys the superconductivity might seem detrimental, but it is in fact energetically more advantageous. Pinning the vortices saves energy, because it prevents break up and reassembling of Cooper pairs (see chapter 1.2.1.2). This allows higher current flow in the material [27, p. 282], even though in most materials pinning slightly decreases T_c because of the worse lattice properties like density, elasticity and electron-phonon coupling due to the defects in the lattice [33, p. 199].

The force created by the pinning centers holding the vortices in place is called pinning force density

$$F_p = j_c \cdot B \quad (1.4)$$

with

$$j_c = \frac{I_c}{A}. \quad (1.5)$$

B is the magnetic flux density, I_c is the critical current and A is the cross section passed by the current. It is highly dependent on the microstructural system e.g. size and shape of the pinning centers. Therefore, the pinning force density may exhibit anisotropic behavior.

In order to determine the pinning force density and the critical current density the critical current can be calculated from measurement data of a U - I -measurement and the following equation [34]:

$$E(I) = E_c \cdot \left(\frac{I}{I_c} \right)^N. \quad (1.6)$$

where $E = U/d$ is the electrical field defined by the equation for a plate capacitor [35,

p. 20 ff] and $E_c = 1 \mu\text{V}/\text{cm}$ is the critical electric field criterion. The length d and the cross section area A of the superconductor have to be determined for the calculation to be able to calculate the critical current density from U - I -measurements:

$$U(I) = E_c \cdot d \cdot \left(\frac{I}{j_c \cdot A} \right)^N. \quad (1.7)$$

In order to calculate j_c from equation 1.5 I_c is determined from the intersection of a linear fit for a logarithmic plot of U as a function of I and the critical electric field E_c as shown in the following figure 1.5.

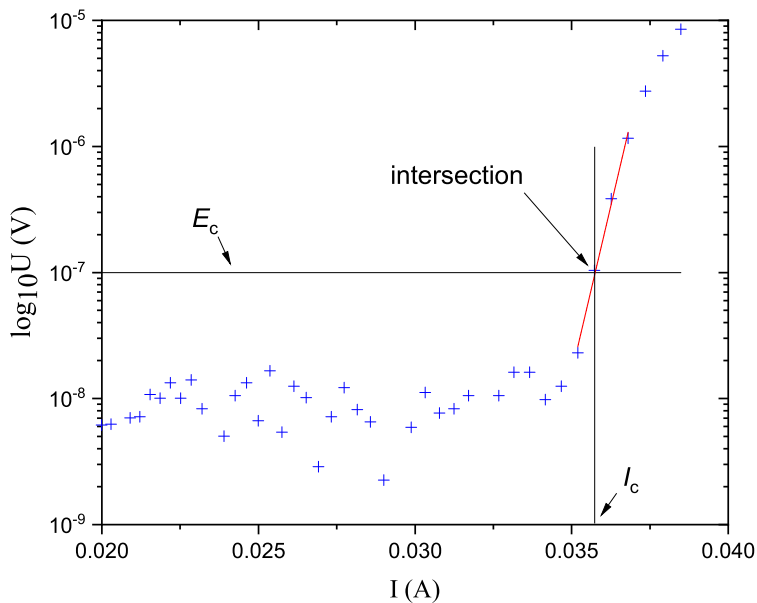


Figure 1.5: Graphical representation of determination of the critical current from U - I -measurement.

1.2.1.4 Anisotropy measurements

Anisotropy measurements are important tools to investigate pinning and transport properties of superconducting samples.

U - I -measurements are performed at various levels of applied magnetic fields while changing the angle of the sample surface to the magnetic field direction after each U - I -measurement.

As a result, the critical current densities are plotted over the angle to the applied magnetic field direction.

These results can be interpreted in which crystal lattice direction the critical current density is enhanced or decreased. These values exhibit also pinning in different crystal lattice directions, even intrinsic pinning by the lattice itself.

High-temperature superconductors (HTS) show large deviations of critical current density flowing in c -direction in comparison to critical current density flowing in a/b -direction of the crystal lattice [36, p. 330]. The critical current density in c -direction

is significantly lower than in a/b-direction. “This anisotropy is larger for a more two-dimensional superconductor” [36, p. 330].

1.2.1.5 Determination of flux pinning mechanisms in type II superconductors after Dew-Hughes

As already shown in chap. 1.2.1.3, the critical current density is determined experimentally as a function of F_p and H (see eq. 1.4). “The function of F_p deduced from these measurements must be zero at $H = 0$, pass through at least one maximum and return to zero at H_{c2} ” [37, p. 293]. Dew-Hughes presented an alternative approach to elaborate theoretical models for predicting different pinning mechanisms in type II superconductors. In contrast to other works, this alternative approach considered:

- “The superconducting nature of the pinning centres, as it is the difference between their superconducting properties and those of the matrix which determines the strength of the local interaction.
- The size and spacing (or ‘wavelength’) of the pinning microstructure compared to the superconducting penetration depth λ , as only if this is greater than λ can the local equilibrium value of B be established.
- The size of the pinning centres compared with the flux-lattice spacing, as this determines the total length of interacting flux-line, and the geometrical nature of the interaction.
- The rigidity of the flux lattice, as this determines whether displacements of flux-lines under local pinning forces are purely elastic, resisted by neighbouring flux lines, or the pinning forces are sufficiently strong to completely disrupt the lattice and allow each flux-line to act individually” [37, p. 295].

The equations for different pinning mechanisms were plotted and can be compared to the measured pinning force data in order to determine the acting pinning mechanism.

As an example the three pinning mechanisms are shown in fig. 1.6.

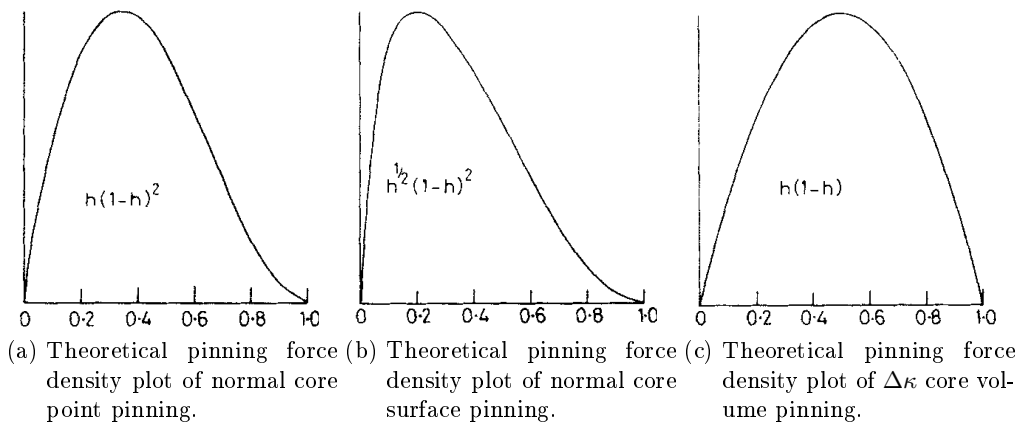


Figure 1.6: Three types of theoretical models by Dew-Hughes for (a)) normal core point pinning, (b)) normal core surface pinning and (c)) $\Delta\kappa$ core volume pinning [37, p. 300]. h is the parameter of the magnetic field normalized to the value of null represented on the x-axis.

The plots fig. 1.6 show

- a) normal core point pinning.
Reasons for that pinning mechanism are point defects [37, p. 295].
- b) normal core surface pinning.
This mechanism can be explained by grain boundaries, step defects and similar [37, p. 298, 300].
- c) $\Delta\kappa$ core volume pinning.
This is especially suitable for materials with a high κ and mixed microstructure [37, p. 298, 300, 301] for larger pinning centers such as nanocolumns.

1.2.2 Technical applications for superconductors

Since the discovery of superconductivity, people attempt to use that phenomenon for technical applications. Today there are already lots of applications in use in normal life and science. There are e.g. superconducting cables and tapes, superconducting magnetic coils, superconducting magnets, superconducting permanent magnets, particle accelerators, nuclear fusion nuclear, magnetic resonance, magnetic resonance imaging, energy storage devices, motors and generators, levitated trains, transformers and current-limiting devices.

In the field of electrical power distribution, installation of superconducting cables over the distance between the power station and private consumers can be imagined. Losses in the cable network would be reduced in comparison to the current solution with copper cables. Yet, superconducting cables are still expensive and the peripheral cooling equipment must be considered energetically, financially and from the construction point of view. There has to be enough space to build cooling stations. Superconducting

cables have to be prevented from quenching. That means they locally become normal conducting and this quench spreads throughout the cable. Since the current densities are too high, the overflow current has to be detected at the quench spot and be dumped in due time. Consequently, the quench detection and protection is a very important point regarding safety, especially in inhabited areas or in applications such as transportation devices. The installation of superconducting cables may become worth if larger currents must be carried by a fixed cable cross-section, especially with predicted increasing power consumption of big cities in the future. The superconducting cable can be installed in the already existing cables pits consuming less space for the same current transport. This will be interesting, especially with the extensive introduction of electrical cars and their charging infrastructure. The change to sustainable energy sources and sustainable transportation will also increase the power consumption and the current load of the power grid making smart solutions, such as superconducting applications, necessary.

In 2014 the world's longest superconductor cable was integrated in the power grid of Essen, Germany (see fig. 1.7).

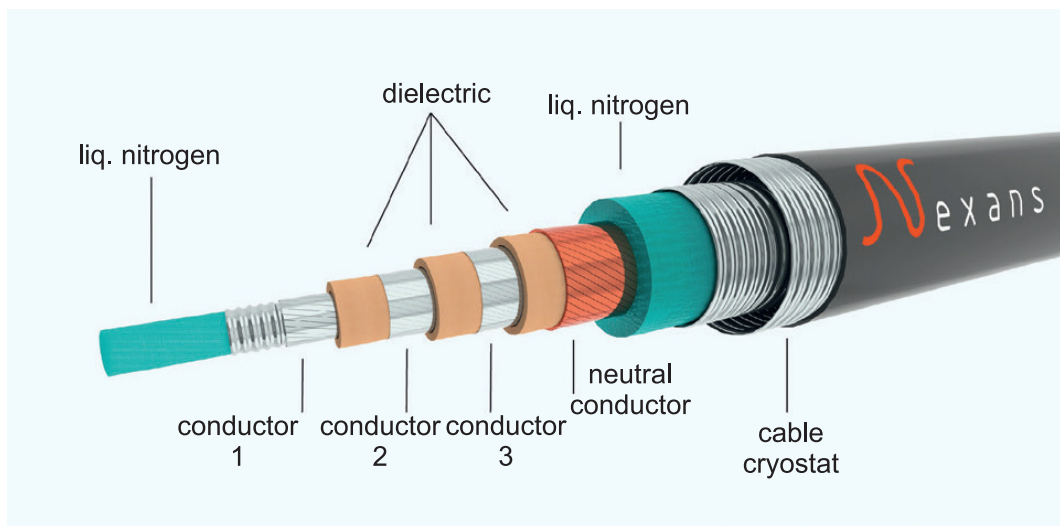


Figure 1.7: Schematic view of the concentric structure of the HTS AmpaCity cable by Nexans.

The project named AmpaCity was realized by RWE, Nexans and the Karlsruhe Institute of Technology. It costed € 13.5 million. It is a 10 kV superconductor, carrying 40 MW of power and replacing five copper cables. It is a concentric cable with three conducting phases, a neutral conductor and an integrated liquid nitrogen cooling cycle. It is a field trial to investigate the long-term performance of operating a power grid with changing current loads with the usage of a superconducting cable [38, 39].

It is necessary to take a look at the whole system in order to identify where and when superconducting applications offer advantages. Some possible application may be impossible with conventional technology. Superconducting technology finds a niche in these applications. This is e.g. already realized in high magnetic fields in large volumes

or levitating transportation.

Large experiments, like the Large Hadron Collider (LHC) at CERN in Geneva, would be impossible without superconducting technology and superconducting magnets. LHC gives mankind the opportunity to explore research fields in sub-atomic physics in order to understand the origin of the universe and quantum mechanics, which were impossible to investigate before. The 1232 dipole magnets (see fig. 1.8) at LHC supply 8.33 T each. 160 superconducting cables form a coil, each housing 36 strands of superconducting wire. Each strand consists of 6500 superconducting filaments of NbTi (with 47 Wt% of Ti) [40]. The dipole magnets keep the particle beam on track, forcing the beam to the center of the collider.

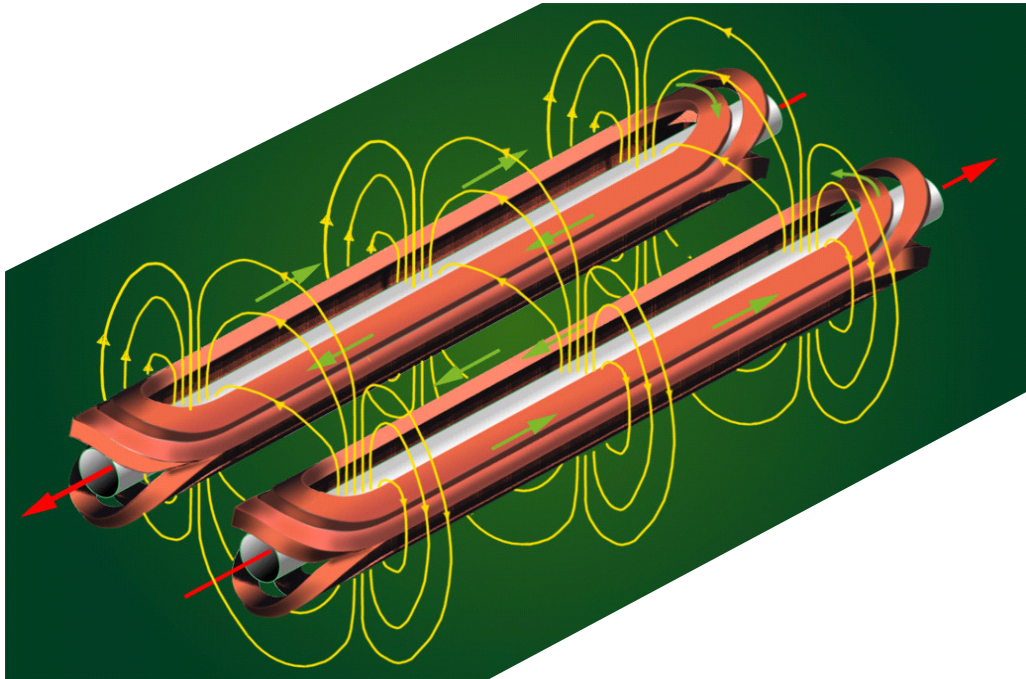


Figure 1.8: Schematic view of the LHC dipole magnets with emphasis on the superconducting NbTi-racetrack coils. LHC features up & down dipoles side by side [40].

Another example is the friction-free levitating and self-positioning property of superconductors enable the application of magnetic levitation trains, such as the Japanese JR-Maglev (fig. 1.9).



Figure 1.9: Photograph of the JR-Maglev MLX01 on track [41].

It reaches a top speed of 500 km/h, travelling 30 km between the station Tokio and Osaka [41, 27, p. 379 f]. In December 2018 the Central Japan Railway Company announced an improved vehicle, which will be put into operation in 2027 [42].

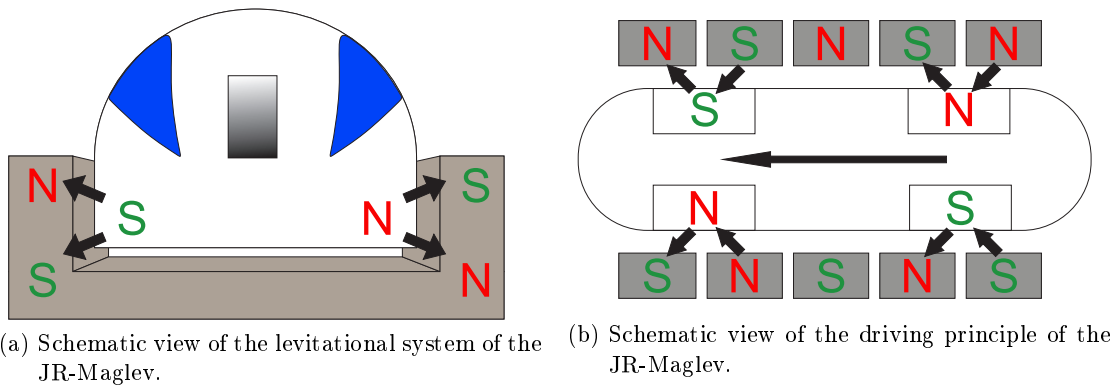


Figure 1.10: Schematic view of the (a) levitational system and (b) driving principle of the JR-Maglev.

The magnets are inside the side rails keeping the train afloat and stabilized in its position (see fig. 1.10a). It will be pulled towards the upper magnetic pole and is pushed away by the lower magnetic pole. The train is propelled by the magnetic forces of the rails to the magnetic poles inside the train (see fig. 1.10b). Same magnetic poles push the train, whereas counter poles attract each other pulling the train in the moving direction.

1.2.3 Ba122

In the past 10 years, many different FBS compounds have been discovered. They are divided into groups called families. There are “11” (e.g. FeSe, FeTe), “111” (e.g. LiFeAs), “122” (e.g. BaFe₂As₂, SrFe₂As₂) and “1111” (e.g. LaOFeAs, NdOFeAs) [4].

This work focuses on Co- respectively P-doped BaFe₂As₂. It is called Ba122 because of the first element it contains and its affiliation to the 122-family.

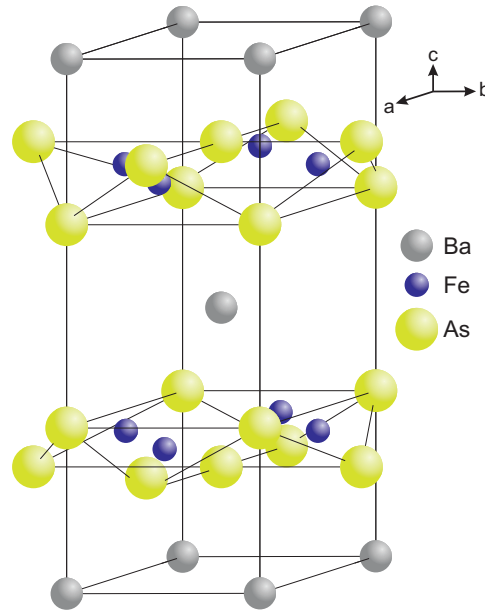


Figure 1.11: Illustration of a unit cell of the Ba122 compound to emphasize the positions of the elements in the compound.

This group of the FBS are also called pnictide superconductors because they consist of iron (Fe) and an element of the pnictogen group (group 15 of the periodic table, also known as nitrogen family or in semiconductor physics group V) [43]. In this work, the pnictogen of choice is arsenic (As).

At room temperature, Ba122 forms a tetragonal lattice structure (see fig. 1.11) with lattice parameters of $a = b = 3.963 \text{ \AA}$ and $c = 13.017 \text{ \AA}$ [44, p. 1]. At temperatures of 140 K, a structural phase transition takes place. The square net of iron atoms (see fig. 1.11) becomes rectangular with distances of 2.97 respectively 2.81 \AA , resulting in an orthorhombic structure [44, p. 2].

Ba122 compounds are quite stable in air or water vapor [11]. They show high crystalline quality such as flat surface and a sharp transition of the critical temperature $\Delta T_c = 1.1 - 1.3 \text{ K}$. Critical current density (j_c) values up to 4 MA/cm² for Co-doped Ba122 on (La,Sr)(Al,Ta)O₃ (LSAT) and magnesium oxide (MgO) were reported [12, 13]. Many investigations showed good growth for Ba122 compounds by pulsed laser deposition to achieve smooth surface films with fairly high j_c and T_c values [12, 13, 45].

Properties such as layer-type crystal structure, high upper critical fields, 2D-behaviour [7], few thermal fluctuations, low anisotropies [9] and multi-band superconductivity [10]

make these compounds interesting candidates for power applications such as cables and coils as well as for electronic applications such as single-photon detectors [46]. It already has been reported that cables and wires have been produced with the industrially interesting PIT technology [16, 15]. Ground FBS powders are filled into a silver (Ag) tube, pressed and annealed at high temperatures, enabling the Ba122 compound to grow in the flattened tube, which resulted in a superconducting cable.

Conclusively, superconducting Ba122 compounds such as well-investigated $\text{Ba}(\text{Fe},\text{Co})_2\text{As}_2$ and $\text{BaFe}_2(\text{As},\text{P})_2$ are suitable model systems for investigations of synthesis and characterization of effective pinning centers by targeted PLD insertion of nanoscale defect structures in epitaxial thin films due to their heteroepitaxial layer growth on various substrates with low misorientation angles at grain boundaries and few intrinsic defects, high critical temperatures, high critical current densities and low anisotropies. Additionally, they do not contain volatile atoms such as potassium or fluorine in comparison to compounds of the 11-family and are therefore optimal for quasi-multilayer deposition with equally distributed nanoparticles between closed layers of superconducting compound.

BaFe_2As_2 itself is not superconducting. There are several methods to create superconducting Ba122 compounds:

Strain/pressure

Strain or pressure in the lattice can help to suppress magnetism and subsequently induce superconductivity in the compound. Strain due to “interfacial bonding between Fe and the FeAs sublattice increases the Fe–Fe distance due to the lattice misfit, which leads to a suppression of the antiferromagnetic spin density wave and induces superconductivity” [47]. For example, external pressure reduces the spin density wave order and preserves the tetragonal structure instead of changing to orthorhombic symmetry causing superconductivity with values comparable to values achieved with doping [48].

Hole-doping

For hole doping, the number of electrons in the FeAs-planes has to be decreased to create an excess of charge carriers (in this case holes). This is reported to be achievable by doping e.g. with potassium (K). K^+ is exchanged for Ba^{2+} . The samples show a maximum T_c of 38 K at a doping level of $x = 0.4$ while superconductivity already appears at a doping level of $x = 0.16$ [49]. Due to the high volatility and reactivity, potassium-doped thin films are difficult to prepare [50].

Isovalent doping

Isovalent doping for example, is realized by using phosphorus (P) to substitute arsenic (As). There is no change in number of charge carriers such as holes or electrons. The only change happens in the ionic radius. As^{3-} has a slightly larger ionic radius of 0.12

nm than P^{3-} (0.106 nm), causing a lattice distortion that induces superconductivity - comparable to superconductivity induced by strain [51].

The successful preparation of P-doped Ba122 thin films has been reported, showing T_c values up to 25 K. Due to growth temperatures above 1000 °C, the preparation of P-doped Ba122 films nevertheless is challenging [52].

Adachi et al. [53] showed that PLD grown P-doped Ba122 films exhibit $T_{c,0}$ of 24 K and high j_c values of 3.5 MA/cm² at 4.2 K.

Electron doping

Electron doping is the opposite of hole doping. The number of electrons must be increased to achieve an excess of charge carriers. This can be achieved by using cobalt as a doping material. Fe^{2+} is partially substituted by Co^{3+} . The maximum T_c of 22 K is obtained at doping levels between $x = 0.06$ and 0.08 [25], whereas superconductivity already appears at doping levels of $x = 0.04$ [54]. In this work, Ba122 with $x = 0.08$ of Co (see chapter 1.3.1.1) is used for quasi-multilayer technique, since it provides high T_c values and lower, easier-to-handle deposition temperatures than P-doped Ba122, besides the positive properties of the mother compound (mentioned in 1.2.3) . The T_c will be reduced by disorder, caused by implemented nanoparticles.

1.2.4 Epitaxy and growth

Epitaxy describes the controlled growth of materials on surfaces (substrates). In this growth process, the deposited layer is oriented to the crystal structure of the substrate and itself forms a certain structure. There are basically two different types of epitaxy: homoepitaxy, where the same material as the substrate is deposited on the substrate, and heteroepitaxy, where substrate and applied material differ. In the case of homoepitaxy, the given structure of the substrate usually forms in the applied layer. In heteroepitaxy, the probability that this will not happen is significantly higher. Due to differences in the lattice constants of the different materials, defects, distortions and/or dislocations can occur during film growth [55]. With some materials, the ratio of the two lattice constants is integer, so that the layers can assume a similar periodic structure. However, ordered layer growth is also dependent on other parameters, such as substrate temperature. If the temperature is too low, the layer may not close. At high temperatures the atoms and molecules are very mobile and move across the substrate surface. It is then possible that the film closes due to the mobility. Unordered growth can also occur [56]. If temperatures are too high, the desorption of the materials to be applied can also prevent growth. The mobility of atoms on surfaces varies from material to material. The type of bonds and the bond energies between the substrate and the layer and between the individual layer atoms also play an important role for the growth mode. In general, a distinction is made between three different growth modes (see fig. 1.12).

- Frank-v.d. Merwe growth (layer growth)
- Volmer-Weber growth (island formation)
- Stranski-Krastanov growth (mixed form of layer growth and island formation)

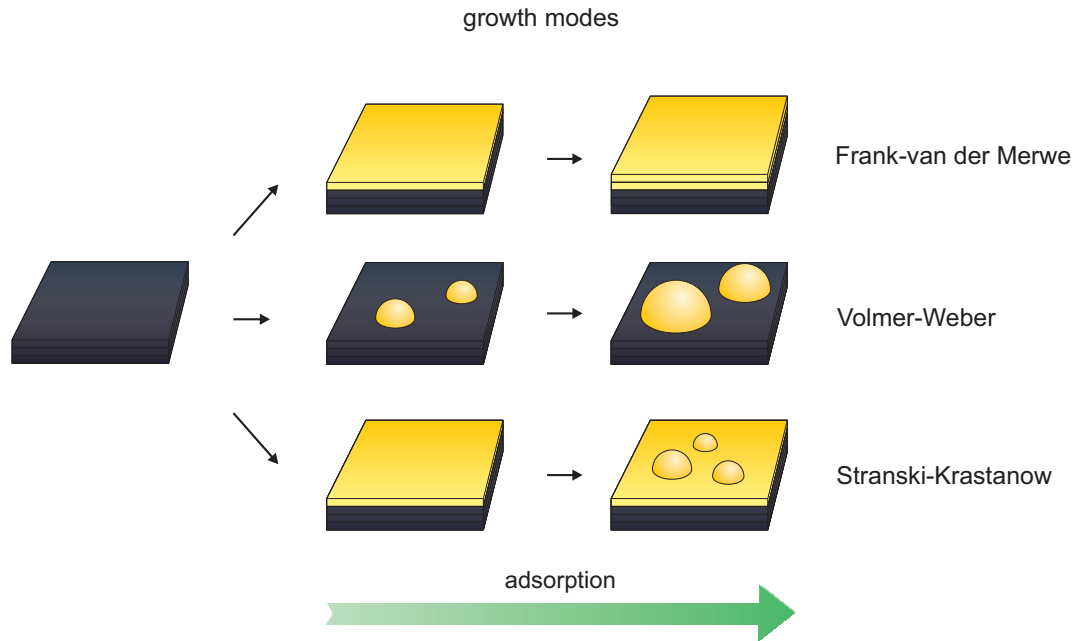


Figure 1.12: Illustrated diagram of the different modes of growth.

In Frank-v.d. Merwe growth, the layer material successively forms monolayers on top of each other, enabling a closed film growth. This is due to the binding energies, which in this case are greater between substrate and film than the binding energy between the layer atoms. This growth also occurs when the bond energy is small compared to the surface energy [57, 58, 59].

In Volmer-Weber growth, the layer material forms islands on the surface of the substrate, since the binding energy of the layer atoms is greater among each other, than the binding energy to the atoms of the substrate. Therefore it is energetically more favorable for the layer atoms to accumulate together [60].

Stranski-Krastanov growth is a hybrid of both above mentioned growth modes. First, the layer material forms one or more monolayers (the so-called wetting layer), whereupon islands are formed. This is due to the change in the ratio of binding energies with increasing layer thickness. At first, the binding energies between substrate and layer atoms are larger than the binding energies between the layer atoms. At a certain layer thickness (the so-called strained layer), the binding energies of the layer atoms outweigh each other due to the tension in the applied material and it is energetically more favorable to form islands. This growth mode should take place when the stress energy is large compared to the surface energy [61].

1.2.4.1 Ba122 film growth

The most common deposition method for Ba122 compounds is pulsed laser deposition (PLD). It features fast and good growth of thin films with great reproducibility of the process parameters. It shows high crystalline quality such as flat surface, low misorientation angles at grain boundaries [20] and a heteroepitaxial layer growth mechanism with $c/2$ -ledges [19]. The use of krypton monofluoride (KrF) excimer lasers as well as neodymium-doped yttrium aluminum garnet (Nd:YAG) lasers have been reported to successfully grow high quality superconducting Ba122 films [12, 13, 45].

According to Lee et al. [62] BaFeO₃ nanopillars appeared in the Ba122 matrix after employing STO or BaTiO₃ template layers and therefore angle dependence of j_c showed a strong c -axis peak. The films exhibit high crystalline quality and high j_c values of 4.5 MA/cm² at 4.2 K.

Thersleff et al. [63] found that an Fe buffer layer between substrate and film provides high crystalline quality growth because the bcc-structured Fe interacts directly with the FeAs tetrahedron in the Ba122 compound and fairly high j_c values of 0.45 MA/cm² at 12 K can be reached.

Adachi et al. [53] reported PLD grown P-doped Ba122 films to exhibit $T_{c,0}$ of 24 K and high j_c values of 3.5 MA/cm² at 4.2 K. Whereas Sato et al. [64] experimented with higher deposition temperatures and optimized film growth in c direction and observed pinning centers in this direction. Hiramatsu et al. [52] found optimal deposition temperature to be at 1050 °C for P-doped Ba122 films with T_c values of 25 K.

1.2.4.2 Substrates

In this work, three different substrates are used. All of them are commercially available. The surface of all substrates has (100)-orientation.

MgO

Magnesium oxide (MgO) has been reported to be a suitable substrate for Ba122 growth [65, 66, 67]. It is mechanically and chemically stable and exhibits a cubic crystal structure with a lattice parameter of 0.421 nm [68]. The substrates have a thickness of 1 mm and a size of 10 by 10 mm.

LaAlO₃

Lanthanum aluminate (LAO) has a cubic perovskite structure with a lattice parameter of 0.382 nm [69]. The substrates have a size of 10 by 10 mm and a thickness of 1 mm. As already mentioned in chapter 1.2.4.1 Co-doped Ba122 has been successfully grown on LAO [70]. Additionally, LAO is mechanically and chemically stable and shows crystal twinning morphology at the surface visible even to the eye [71].

CaF₂

Calcium fluoride (CaF₂) also has a cubic structure [72] with a lattice parameter of 0.546 nm. Substrates have a size of 5 by 10 mm and a thickness of 1 mm [73]. Growth of Co-doped Ba122 with fairly high T_c values has been reported [74, 19] due to strain induced by formation of BaF₂ in the matrix [19]. CaF₂ is brittle and therefore not as mechanically stable as MgO or LAO.

1.3 Preparation and experimental setups

The complex preparation of samples and the method for investigation can differ widely. Therefore it is necessary to explain the experimental setups as well as the measurement setups and the chosen measurement methods. In the first part of this chapter the preparation of the PLD targets is explained, followed by a brief introduction of the experimental setup and the pulsed laser deposition. In order to measure electrical transport properties, the samples need to be structured. This process is presented in the last part of this chapter.

1.3.1 Target preparation and properties

1.3.1.1 Ba122

The $\text{Ba}(\text{Fe}_{0.92}\text{Co}_{0.08})_2\text{As}_2$ targets were prepared according to [25].

Prior, the precursor materials FeAs, Fe_2As , Co_2As , BaAs first have to be prepared under argon (Ar) atmosphere. The materials are milled, mixed and pressed in the right stoichiometric ratio. They are sealed under Ar pressure in a glass tube. During high temperature exposure, the materials react to the precursor materials. These are milled, mixed, pressed and heat treated to obtain the superconducting material of Co-doped Ba122 [25, p. 5].

The doping level of $x = 0.08$ has been reported to provide optimal superconducting properties [25] and was therefore chosen.

The $\text{BaFe}_2(\text{As}_{0.6}\text{P}_{0.4})_2$ targets were prepared at LMU Munich [49]. The doping level of $x = 0.4$ has been reported by Rotter et al. [75] to be optimal for achieving best superconducting properties.

1.3.1.2 BaZrO₃ (BZO)

The BZO target with a purity of 99.9 % is commercially bought [76]. BZO is a perovskite with a cubic lattice ($a = 4.192 \text{ \AA}$) [77]. BZO has already been used in YBCO compounds as a pinning material forming nanoparticles [78] as well as nanorods [79]. Lee et al. [23] and Miura et al. [20] used it as a pinning material in Co-doped respectively P-doped Ba122. In Co-doped Ba122 BZO forms nanorods parallel to c-axis with a diameter of 4 nm. This is a suitable size for pinning centers because it is almost double the size of the coherence length $\xi = 2.5 \text{ nm}$ of Ba122 [23].

1.3.1.3 BaHfO₃ (BHO)

BHO is used to implement nanoparticles acting as pinning centers in the superconducting film. The material has a perovskite structure [80, p. 779] with a crystal constant of 4.1717 \AA and was already used as a pinning center material for the well-studied high temperature superconductor $\text{YBa}_2\text{Cu}_3\text{O}_{7-x}$ -compounds [81].

The BHO targets were prepared from BaCO_3 and HfO_2 powder at Institute for Technical Physics (ITEP) of the Karlsruhe Institute of Technology (KIT). The powders are mixed, pressed and sintered up to 1150 °C. The result is ground and pressed again in an isostatic press and sintered again up to 950 °C. Since BHO and BZO are structurally similar BHO could be a suitable pinning material for Ba122 as well.

1.3.1.4 InAs

InAs is a semi-conductor with cubic symmetry and a lattice constant of 6.06 Å. It should be stable within the film when implemented as nanoparticles during quasi-multilayered deposition since it is an arsenide. It has been reported that deficiency or vacancies of As in Co-doped Ba122 films increases the critical current density [47] and acts as pinning centers [25]. Furthermore, it does not contain oxygen which might replace As atoms causing a decrease or even destruction of superconductivity.

The only disadvantage is the low re-evaporation temperature of around 570 °C [82].

The 99.99 % purity InAs target with a diameter of 25.4 mm and a thickness of 5 mm was commercially bought [83].

1.3.2 Pulsed laser deposition (PLD)

Pulsed laser deposition (PLD) is physical method for film preparation from the gas phase and usually takes place in vacuum. The advantages of PLD are the large flexibility regarding the materials, possible deposition conditions and stoichiometric material transfer.

A high energetic, pulsed (10 - 25 ns) and focused laser beam hits a target of the deposition material (see fig. 1.13), which is mostly a stoichiometric sintered or melt-processed bulk. The irradiation of the laser beam leads to a strong local heating and ablation of the target material. This generates a plasma plume which extends nearly perpendicular from the target surface towards a heated substrate and causes the film deposition [84, 85]. Deposition parameters, such as laser energy, energy density at target, repetition rate of laser, substrate temperature, target-substrate distance and surface constitution of the target influence the film growth. Higher laser energies as well as higher laser frequencies result in higher growth rates and lower re-evaporation rates of the deposition material. For Co-doped Ba122 grown by this Nd:YAG laser it was found that growth rates near the maximum of 0.9 Å/s (energies of around 30 mJ and at frequencies of 10 Hz) show best results [19]. The substrate temperature influences the molecules or atoms condensing on the substrate surface. In order to achieve optimal film growth, the thermal energy needs to be high enough to provide enough kinetic energy for the molecules or atoms to move on the surface, agglomerate and form a closed layer. If the temperature is too high, the deposition material can also re-evaporate from the substrate, thereby having a disturbing effect on the growth mode and on the thickness of the film. The optimal growth temperature depends on the physical properties of

substrate and deposition material and their relation to each other such as binding and surface energy (e.g. see chap. 1.2.4). Further, the distance and position between target and substrate has an effect on the quality of the film. Depending on the material, different stoichiometries and particle sizes could be obtained. The target material can also degrade or the stoichiometry at the surface can change with time. Therefore, the ablation of the target surface has to be as even as possible. This can be achieved by wobbling the target during deposition. Additionally, the laser energy has to exceed a material specific threshold. Otherwise, the so called preferential ablation occurs, only ablating certain molecules or atoms. In this case, the stoichiometry of the target is not transferred to the deposited film.

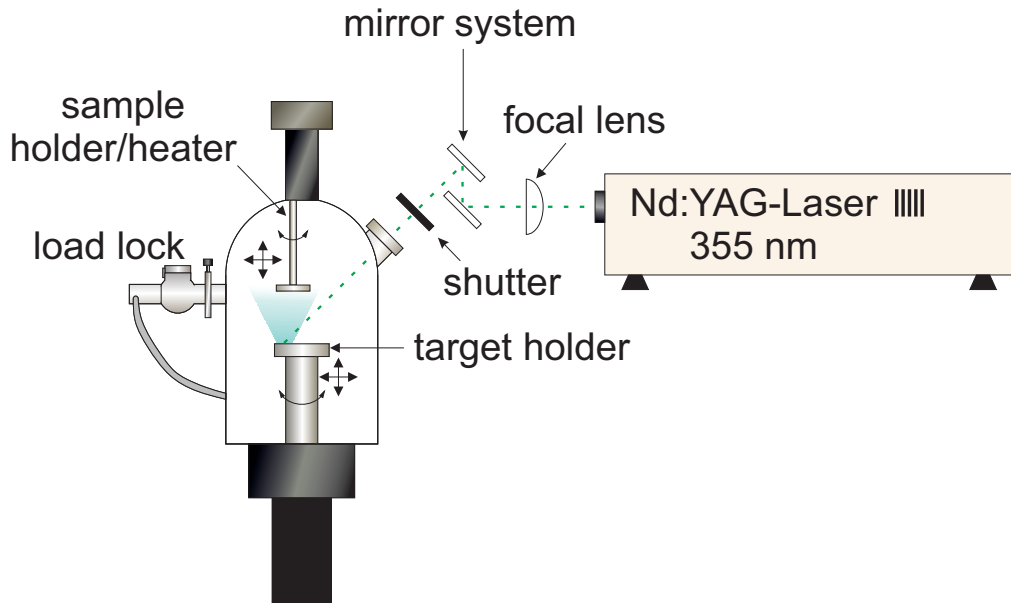


Figure 1.13: Schematic image of the principle working mechanism of the PLD chamber.

The experimental setup is schematically shown in fig. 1.13.

An ultra-high vacuum (UHV) chamber with a base pressure of $p = 10^{-9}$ mbar and a frequency-tripled Nd:YAG laser ($\lambda = 355$ nm, $f_{max} = 10$ Hz, $E_{max} = 150$ mJ, pulse duration < 10 ns) is the main part of the setup.

Target and substrate/heater positions are motorized and controlled by a LabView program. It is used to conduct the laser, the heater, the shutter and target carousel to deposit films on substrates in the ultra-high-vacuum chamber. The program provides the possibility to write, edit and save so called batch files which determine the sequence of film growth, such as heater-target distance, target wobbling, substrate rotation, substrate and target positioning, laser energy, laser frequency and usage of different targets during deposition (multi-layer deposition). To start a deposition the batch files can be edited beforehand and execute the whole deposition process for better reproducibility. The software is furthermore used to measure the remaining pressure at different positions in the vacuum chamber, to obtain reproducible conditions for film growth.

The chamber has a carousel type target holder, storing up to five targets. The usage of more than one target for a deposition is possible. This technology enables growing single material films, as well as multilayered and quasi-multilayered films, also in combination with a buffer layer (e.g. see fig. 1.14).

1.3.2.1 Quasi-multilayer technique

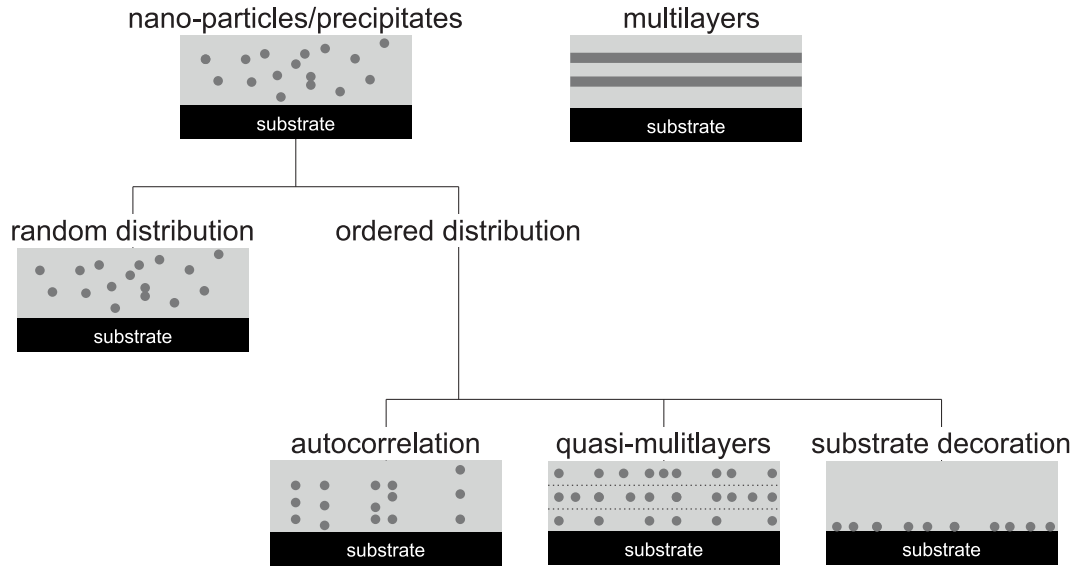


Figure 1.14: Variations in the arrangement of nanoparticles or precipitates for defect generation in the $\text{YBa}_2\text{Cu}_3\text{O}_{7-\delta}$ -matrix. This image has been drawn after [30, p. 23].

The distribution of nanoparticles in a PLD-grown film can be ordered or random. A random distribution e.g. can be achieved by usage of stoichiometric premixed targets [30, p. 22]. An ordered distribution happens e.g. if particles self-assemble in nanocolumns or the particles can be forced into order via a substrate decoration [30, p. 22]. The quasi-multilayer technique can be used e.g. for implementing nanoparticles as pinning centers in a superconducting film in an ordered distribution. The particles are formed from islands (see chap. 1.2.4) of unclosed interlayers of a non-superconducting material [30, p. 23]. They align in the same deposition layer, however without creating a closed layer. This is the reason why this technique is called **quasi-multilayer** technique.

Quasi-multilayered films made via PLD with two targets by implementing nanoparticles of BHO [21, 22] or BZO [1, 2] have been already reported for YBCO-compounds to increase critical current density j_c and pinning force density F_P . The goal of this work is to transfer the quasi-multilayer technique from YBCO-compounds to Ba122 compounds also in order to increase the critical current density and the pinning force density for future technical applications. Therefore, a lot of measures had to be taken. The experimental setup had to be versatile in order to provide a maximum of flexibility and reproducibility of the deposition parameters to enable the optimization of the

parameters for the implementation of nanoparticles in Ba122 compounds.

The targets can be switched by the software during the process. The shutter allows to precisely adjust the number of pulses even down to a single pulse and shuts the laser beam during target switch. Thus it is e.g. possible to deposit closed layers of the superconducting material and non-closed layers of the pinning material in between the superconducting layers, in order to achieve equally distributed nanoparticles as pinning centers. The number of pulses for the superconducting material are very high, to ensure a closed layer, and are followed by a small number of pulses for the pinning material, to ensure the layer is not yet closed. If the pinning material layer was closed and since the pinning material is not superconducting the result would be a stack of superconducting layers separated by non-superconducting layers (see fig. 1.14; multilayers).

Consequently, it is also possible to achieve multilayered films. Therefore, as already mentioned, the parameters have to be chosen to enable a closed layer of each target material.

The shutter is especially important for the deposition of material with high deposition rates. The number of pulses have to be exactly controlled in order to achieve the right composition or film thickness. The shutter has to close and shut a laser pulse repeatedly with a very high energy of 15 J/cm^2 under $1/10$ of a second.

1.3.3 Chemical etching

Wet chemical etching, respectively photolithography processes, are used to obtain bridges (normally of around $50 \text{ }\mu\text{m}$ width and 1 mm length) in the film. These bridges are necessary to have a defined length and area for the current to flow through, so the critical current density j_c can be calculated from I_c data. This is also necessary to enable applying smaller currents which can be supplied by common power sources.

First, a photoresist is spin-coated on the surface of a sample. After two minutes of dry-out process in a furnace at $200 \text{ }^\circ\text{C}$ the photoresist is illuminated by UV-light. For that, a mask covers the parts of the sample, which should not be cured by a developer solution afterwards. Immersion in a 1:1 mixture of H_2O_2 and HNO_3 acid, diluted 1:60 with deionized water, removes all areas covered by uncured photoresist.

The Ba122 layer can be dissolved by acid very quickly, therefore the sample is immersed for only two seconds and subsequently neutralized in deionized water. The remnant of the photoresist is removed by immersion in acetone.

1.4 Characterization

In this chapter the measurement setups as well as the principles behind the measurements are presented in order to create a deeper understanding of the different characterization methods.

1.4.1 Physical property measurement system (PPMS)

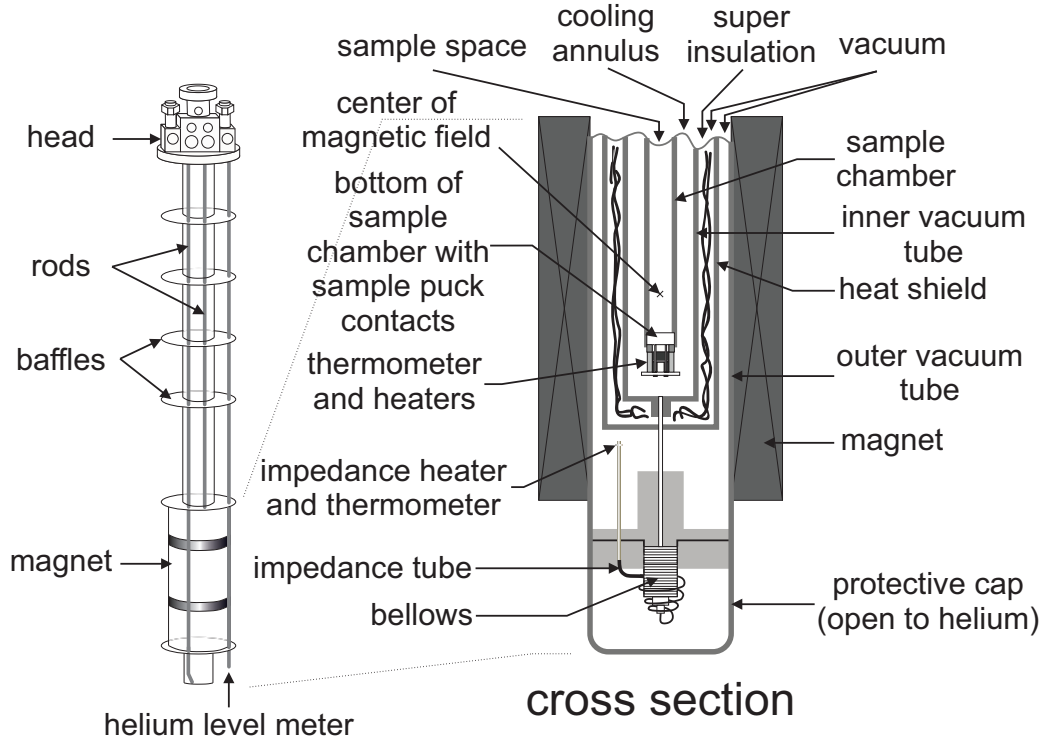


Figure 1.15: Schematic view of the principle of the physical property measurement system [86, p. 2-4]

The investigation of electric properties of superconducting samples requires an experimental setup, in which parameters such as sample temperature, magnetic field and sample orientation with respect to the magnetic field can be controlled while performing four-point resistivity measurements. The four-point resistivity measurement includes four aligned electrodes. Two outside electrodes lead a current through the sample or the bridge. The inner electrodes measure the voltage. This measurement type eliminates the contact resistances and allows for exact electric measurements [87]. With this measurement setup, it is possible to determine parameters such as I_c respectively $j_c(\theta)$, F_p (see chapter 1.2.1.3), $R(T)$, T_c , $R(T, B)$ (by using the definition of the resistance $R = U/I$), H_{irr} and H_{c2} (by calculating $T_{c,onset}$ and $T_{c;90}$ for $R(T)$ graphs for different applied magnetic fields). These measurements are performed in a Quantum Design Physical Property Measurement System (PPMS). The PPMS offers a sample environment with a temperature range from 1.5 to 350 K and magnetic fields up to 14 T. With

an optional rotator sample mount, the sample can be rotated around its horizontal axis - to measure the sample's properties in different angles to the magnetic field. Since the built-in voltage and current measurement options do not fit the necessary sensitivity requirements, four-point measurements are carried out by employing an external Keithley Model 2182A Nanovoltmeter and a Keithley Model 2460 Source Meter Unit. The current and voltage leads are coupled with a switch box into the sample chamber.

1.4.2 X-ray diffraction (XRD)

X-ray diffraction is a technique used to investigate the crystalline structure of a sample. It uses the wave characteristic of electromagnetic radiation diffracted on crystal lattice planes.

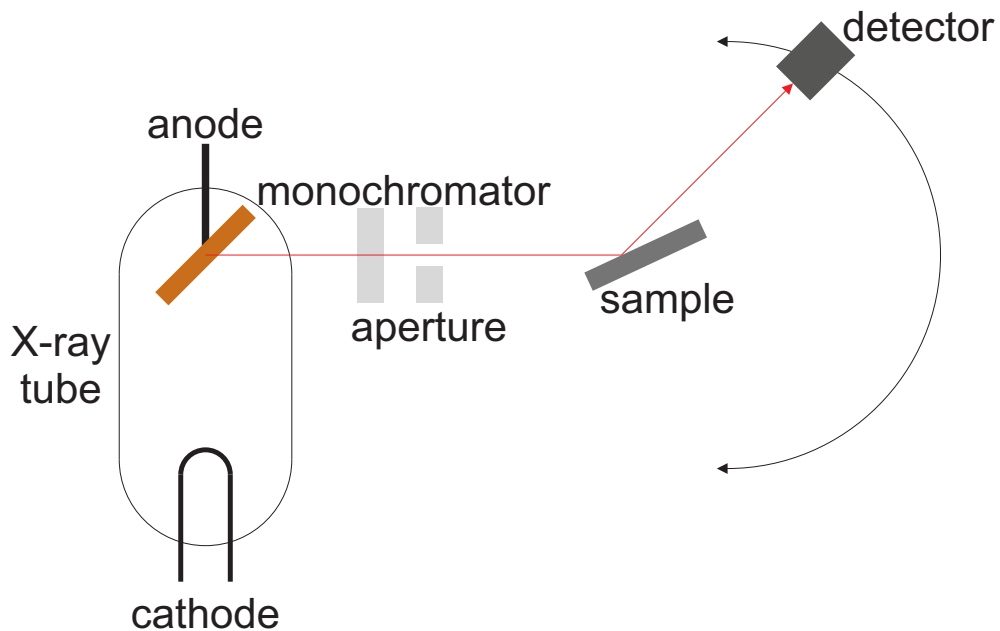


Figure 1.16: Schematic Illustration of an XRD setup and working principle.

The wavelength of X-radiation lies in the range between 1 pm and 10 nm - the same range for lattice plane distances in crystals. This is why crystal lattices work as diffraction grating. Therefore, constructive interference appears only for certain angles, fulfilling the Bragg law

$$2d \cdot \sin \alpha = n\lambda \quad (1.8)$$

where d is the lattice distance, α the angle between the lattice plane and the X-ray beam, n is a positive integer and λ the wavelength of the X-radiation (as shown in fig. 1.17)

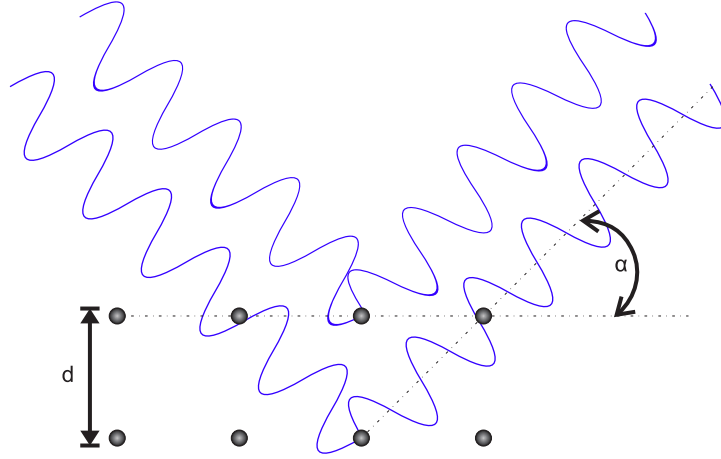


Figure 1.17: Graphic illustration of Bragg diffraction.

For orthorhombic lattices the lattice distance d is calculated to

$$\frac{1}{d^2} = \frac{h^2}{a^2} + \frac{k^2}{b^2} + \frac{l^2}{c^2} \quad (1.9)$$

, using Miller indices h, k, l [88]. Only the lattice distance d is observed due to measurement setup. So $h = k = 0$ simplifies 1.9 to

$$\frac{1}{d} = \frac{l}{c}. \quad (1.10)$$

Combining this equation 1.10 with the Bragg law 1.8 equals to

$$c(l, \alpha) = \frac{l \cdot \lambda}{2 \cdot \sin \alpha}. \quad (1.11)$$

The lattice parameter c can be determined by entering the positions in $^\circ$ of the (001)-reflections into the Nelson-Riley-equation [89]

$$NR(\alpha) = \frac{1}{2} \cdot \left(\frac{\cos^2 \alpha}{\sin \alpha} + \frac{\cos^2 \alpha}{\alpha} \right). \quad (1.12)$$

The resulting values are plotted and linear interpolated with $NR(\alpha) \rightarrow 0$. The y-intercept displays lattice parameter c .

The X-ray diffraction graphs show an out-of-plane growth orientation of the deposited film, since only the lattice distance d is observed. By determining the width of the peaks, the mosaicity - a tilt angle towards the a/b-plane - can be distinguished as well as the particle size of e.g. foreign phases by calculation with the Nelson-Riley-equation 1.12.

To investigate the crystalline structure, orientation of grains and lattice parameters (even strain can be observed by elongation of the lattice parameter c) of a sample, a Bruker D8 Discover X-ray diffractometer with a copper anode (monochromatic $\text{Cu-K}\alpha_{1,2}$ radiation, $\lambda = 0.15406$ nm) was employed for standard $\theta - 2\theta$ diffractograms. The incident beam is parallelized using a Goebel mirror in combination with an axial

0.4 Soller slit and a fixed-sized aperture of 0.6 mm. The angles between 10 and 120 ° were measured with a step width of 0.5 ° per second. The parameters were chosen to achieve the highest intensities without saturating the detector and the lowest possible background noise for the used Ba122 samples in order to be able to see small peaks rising for low concentration of pinning material in the films. The outgoing beam is detected by a 1-D line detector. The peak data is evaluated by using the ICSD database [90] to distinguish the different orientations of the different compounds and foreign phases.

1.4.3 Scanning electron microscopy (SEM)/energy dispersive X-ray spectroscopy (EDX)/transmission electron microscopy (TEM)

A SEM is used to investigate surfaces of conducting samples. The electron beam scans the surface. The interaction of the electrons and the surface is used to create an image of the sample.

The electrons are generated by a heated emitting cathode and are accelerated by an electric field of 0.5 to 50 kV to obtain an electron beam [91]. The electrons are guided and focused by magnetic field lenses to scan the surface of the sample. The inside of the electron microscope is evacuated to high vacuum for the electrons not to hit any gas molecules. The electron beam interacts with the atoms and secondary electrons (SE) are generated and detected. Thus a topography image of the sample surface is displayed [55, p. 24]. Another mode is to detect the backscattered electrons (BSE) to achieve a material specific contrast [92, p. 121]. For this work, all SEM images were taken with a LEO 1530 Scanning Electron Microscope by Zeiss with an acceleration voltage of 20 kV.

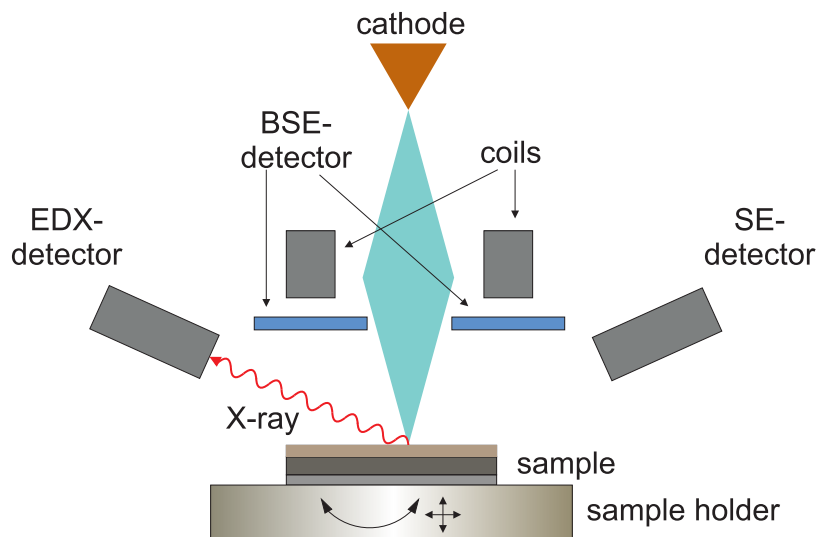


Figure 1.18: Simplified operating principle of a scanning electron microscope; BSE: back-scattered electron; SE: secondary electron; EDX: energy dispersive X-ray spectroscopy.

With an SEM it is also possible to perform EDX. It is a non-destructive way of

investigating the chemical composition of a sample surface. The electron shells of the atoms are excited by a high energy electron beam. Electrons falling back in their states emit an X-ray photon. This is characteristic for each element and is displayed as an image, by detecting the X-ray intensity in comparison to wavelength or energy [93].

TEM uses the same technique as an SEM, but in transmission. First, the sample has to be very thin for the electrons to pass the material. A lamella is cut from the sample via a focused Ga^+ -ion beam (beam energies from 2 keV to 30keV) in-situ lift-out technique in an FEI Strata 400S dual-beam respectively FEI Nova 600 Nanolab Dual Beam system. The incoming electron beam during imaging process points consequently parallel to the Ba122 (100) zone-axis (a-axis). For this work, TEM is used to show cross sections of the samples in order to investigate the distribution of pinning centers in the film. If the sample is scanned in transmission, it is called Scanning Transmission Electron Microscopy (STEM) [94]. The images taken were performed in the so-called High-Angle Annular Dark-Field STEM (HAADF-STEM) mode with a FEI Tecnai Osiris S with 200 kV and a FEI Titan³ with 300 kV.

EDX measurements in STEM were performed in a FEI Tecnai Osiris S TEM with 200 kV. To calculate the amount of the included elements of the sample the standardless Cliff-Lorimer qualification is used. The concentrations of elements are calculated from the relation of the intensities of the X-ray radiation by the software Bruker ESPRIT 2.1. To enhance the accuracy of the determination of concentrations multivariate statistical analysis was applied by the use of the software HyperSpy to increase signal-to-noise ratio in qualitative EDX mappings by means of dimensionality reduction of EDX datasets via principal component analysis (PCA). Especially the overlap of the F $K\alpha$ (677 eV) and Fe $L\alpha$ (705 eV) X-ray lines was resolved by multiple linear least squares fitting of Gaussians at their respective energies.

The SEM images were taken by Dr. Alexandra Jung from the Institute for Technical Physics (ITEP) at Karlsruhe Institute of Technology and TEM measurements were performed by Lukas Grünwald from the institute Laboratory for Electron Microscopy (LEM) at Karlsruhe Institute of Technology and Dr. Hannes Rijkaert from the SCRiPTS group of Ghent university in Belgium.

1.4.4 Atomic force microscopy (AFM)

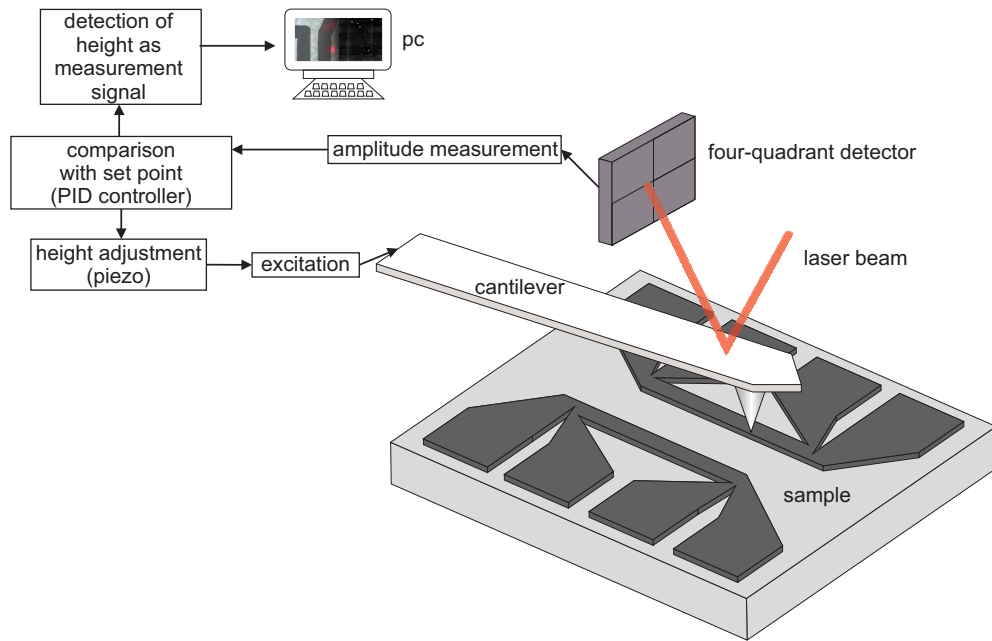


Figure 1.19: Schematic image of the operating principle of an atomic force microscope

The AFM (Atomic Force Microscope) is a method for the direct imaging of the sample surface in real space including height information (important for definition of bridge cross section area for j_c measurements). In this work, a Bruker Dimension Edge was used.

In atomic force microscopy, the sample surface to be examined is scanned with a measuring tip in a predefined scanning pattern. The measuring tip, the end of which should preferably have only one atom, is located at the end of an elastic lever arm, the so-called cantilever. The cantilever is mirrored on its backside. A laser beam is focused on it, projecting the reflection of the beam onto a four-quadrant detector. If the cantilever is deflected from its rest position, the position of the laser beam on the detector changes. The deflection can be measured without contact. It depends on the atomic interaction between the sample surface and the tip. Each pixel of the resulting image receives information about a certain interaction. A control loop is used to keep the height to the sample surface or the contact to the sample constant during the measurement, thereby avoiding contact loss or damage to the sample and the tip. When operating an AFM, the following measurement modes are available.

Contact mode

In this measurement mode, the tip is in direct mechanical contact with the sample surface during measurement. This creates an electrostatic repulsion between the electron shells of the sample atoms and the tip. In the controlled mode (constant force mode), the cantilever is kept at a constant bend by the control loop, allowing the tip keep contact with the sample. With the help of a piezo actuator, the cantilever can be adjusted in height at high speed, following the topography of the sample. The measuring signal here is the control of the piezo drive.

Non-contact mode (tapping mode)

In this mode, the cantilever is not in direct contact with the sample, in contrast to the previously mentioned mode. The cantilever is excited to vibrate close to its resonant frequency. Due to the interaction between sample surface and tip, the amplitude of the oscillation of the cantilever changes and the control electronics corrects this amplitude change to the previously set value. The control signal is the imaging measured variable. All AFM images contained in this thesis were taken in this mode and took place ex-situ.

1.4.5 Inductively coupled plasma mass spectrometry (ICP-MS)

ICP-MS is used to investigate the stoichiometry of a sample. The samples are ground and dissolved in material specific acids such as mixtures of nitric acid, hydrogen peroxide and hydrochloric acid under microwave, pressure vessel or graphite oven conditions at temperatures between 353 and 523 K to generate an aerosol which is heated in an argon-plasma, atomizing and ionizing it. An applied electric field accelerates the ions into a mass spectrometer. There, the ions are detected depending on their ratio of mass to charge [95]. ICP has a very low detection limit up to nanogram-per-liter [96]. The elements were determined by optical emission spectrometry (ICP-OES, iCAP 7600 DUO, Thermo Fisher Scientific) and mass spectrometry (ICP-MS, 7500ce, Agilent) by Dr. Thomas Bergfeldt at the Institute for Applied Materials - Applied Materials Physics (IAM-AWP) at the Karlsruhe Institute of Technology. The analysis of the components was accomplished with four different calibration solutions and internal standards (Sc for ICP-OES, Sc, In for ICP-MS). The range of the calibration solutions did not exceed a decade. Two or three wavelengths and one or two isotopes of the elements have been used for calculation.

2 Experimental results

The goal of this work is to achieve Co- or P-doped Ba122 nanocomposite films with enhanced superconducting properties for future applications. Hence, the growth parameters and conditions of the doped Ba122 have to be understood as well as the implementation of the pinning materials in order to combine the achieved knowledge and produce optimized nanocomposite samples. The used doping levels ($x_{Co} = 0.08$ and $x_P = 0.4$) have been reported to be optimal [25, 75] and were therefore chosen.

This chapter presents the experimental stages, characterizations and investigations of this work - from starting with the optimization of Ba122 growth to implementation of perovskites and InAs as artificial pinning centers to achieve improved electrical transport properties.

2.1 Experimental realization

To obtain optimal growth conditions for Co- and P-doped Ba122, the used substrates have to undergo the following procedures. First, the substrates are put into a beaker filled with isopropyl. This beaker is placed in an ultrasonic bath for 7 minutes. During this time, the sample holder is wiped with a lint-free wipe soaked with isopropyl. Both procedures are performed to remove dust or other contaminations located on the surface. After the ultrasonic bath, the substrate is placed in the sample holder and is dried by an argon flow. Immediately after, the sample holder with the substrate is placed onto the transfer stick in the load lock and which is then pumped. When the pressure reaches the range of $5 \cdot 10^{-7}$ mbar the load lock is opened towards the main chamber and the sample holder with the substrate is transferred into its position at the heater. The heater is already put into deposition position and is set to the characteristic deposition temperature. The substrate has to degas and reach the deposition temperature. During degassing, the pressure in the chamber increases up to pressures within the range of 10^{-6} mbar due to outgassing of the substrate and its holder. After 10 to 20 minutes it drops to values of around 10^{-8} mbar. This entire thermalization process takes approximately 45 minutes to an hour. During this time, the laser is already powered and thermally stabilized. Subsequent to the thermalization process, when the pressure of $3 \cdot 10^{-8}$ mbar has been reached, the deposition can be started via software. For all samples investigated in this work, the number of pulses per sample ranged approximately 18000 resulting in film thicknesses of about 60 to 100 nm. After deposition, the heater is turned off and the sample cools down to room temperature for 45 minutes to an hour.

2.2 PLD of Ba122 films with frequency tripled Nd:YAG laser

Hiramatsu et al. [70] deposited Co-doped Ba122 on LSAT using four different types of lasers:

- a ArF excimer laser with a wavelength of $\lambda = 193$ nm,
- a KrF excimer laser with a wavelength of $\lambda = 248$ nm,
- a second harmonic Nd:YAG laser with a wavelength of $\lambda = 532$ nm

and

- a fundamental harmonic Nd:YAG laser with a wavelength of $\lambda = 1064$ nm.

The frequency-tripled Nd:YAG laser ($\lambda = 355$ nm) used for this work had not been tested or reported on ablation of Ba122 before 2018. The first experiments of this work were performed in 2015. The closest version to the deployed laser in this work, was the frequency-doubled Nd:YAG laser with a wavelength of $\lambda = 532$ nm and an optimum pulse energy of 2.2 - 3.2 J/cm², tested by Hiramatsu et al. [70]. They however could not find any difference to films deposited with a KrF laser [70].

The reason for the use of a frequency-tripled Nd:YAG laser is its wavelength of 355 nm. The third harmonic of the Nd:YAG laser is located in the near ultraviolet spectrum, but is not as harmful to tissue or eyes as the first or the second harmonic.

The first harmonic of the Nd:YAG laser with 1064 nm lies within the near infrared spectrum and is very harmful.

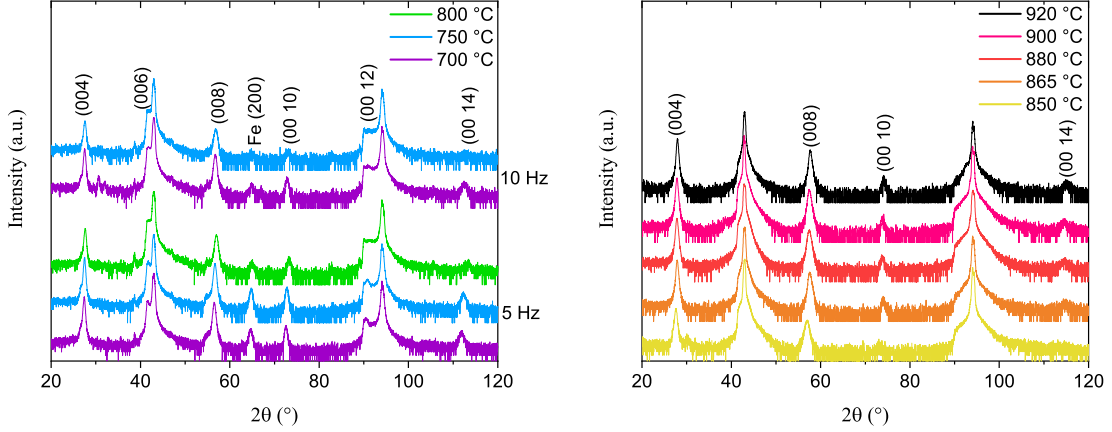
The second harmonic with 532 nm wavelength lies in the visible spectrum and is not only very harmful for the eyes but also difficult to handle regarding safety measures. The solid state medium, as opposed to the toxic gas medium used in KrF lasers, presented itself as a further advantage of the Nd:YAG laser.

Eventually the question arises, if a frequency-tripled Nd:YAG laser can be used to grow Ba122 compounds in good crystalline quality and with good superconducting properties. Therefore, several substrates had to be tested and the deposition parameters had to be optimized for each kind.

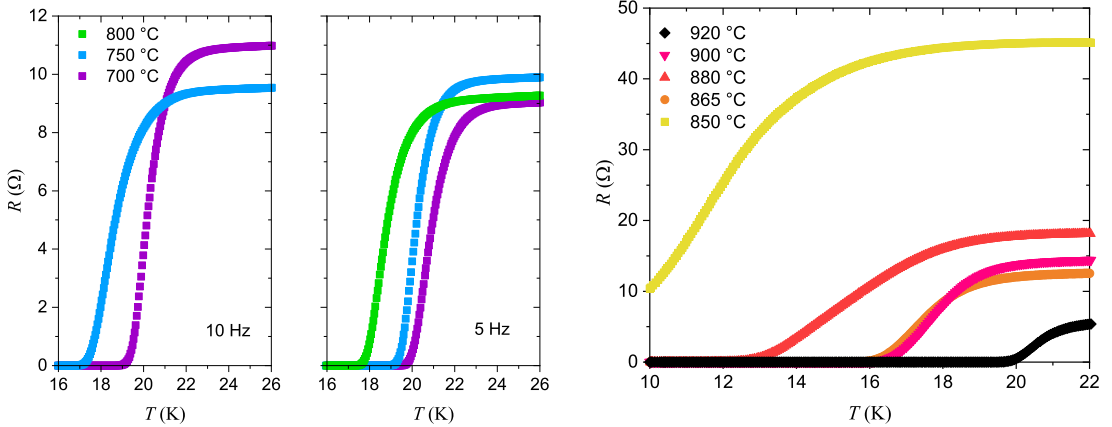
2.2.1 Formation of Fe interlayer

Initially, the first experiments were performed using MgO (100) as a substrate, due to its properties and low dielectric constant, which make it interesting for applications [65, 66, 67]. BaFe₂(As_{0.6}P_{0.4})₂ and Ba(Fe_{0.92}Co_{0.08})₂As₂ films with thicknesses of 45, respectively 50 nm were deposited on MgO (100) single crystalline substrates. The growth of P-doped Ba122 was also investigated due to its interesting properties such as high $T_{c,90}$ -values of approximately 28.3 K to 31 K and high j_c -values over 10 MA/cm² at 4.2 K, as reported by Iida et al. [97]. Deposition temperatures were in the range of

850 - 950 °C for P-doped and of 700 - 800 °C for Co-doped Ba122 films. Laser energies of 40 mJ (4. J/cm²) at target and repetition rates of 5 and 10 Hz for cobalt-doped samples and 35 mJ (3.5 J/cm²) at target and 10 Hz for phosphorus-doped samples were tested. Films grown with other values did not show superconducting properties. The growth rates were 0.75 Å/s for phosphorus-doped samples and 0.29 Å/s for cobalt-doped samples. The substrate target distance was 40 mm. The target diameter was 10 mm of size for both types of targets.



(a) $\theta - 2\theta$ scans of Co-doped Ba122 on MgO substrates prepared at three different deposition temperatures and two different laser frequencies. The intensity is plotted as a logarithmic function of the angle 2θ . (b) $\theta - 2\theta$ scans of P-doped Ba122 on MgO substrates prepared at five different deposition temperatures and a laser frequency of 10 Hz. The intensity is plotted as a logarithmic function of the angle 2θ .

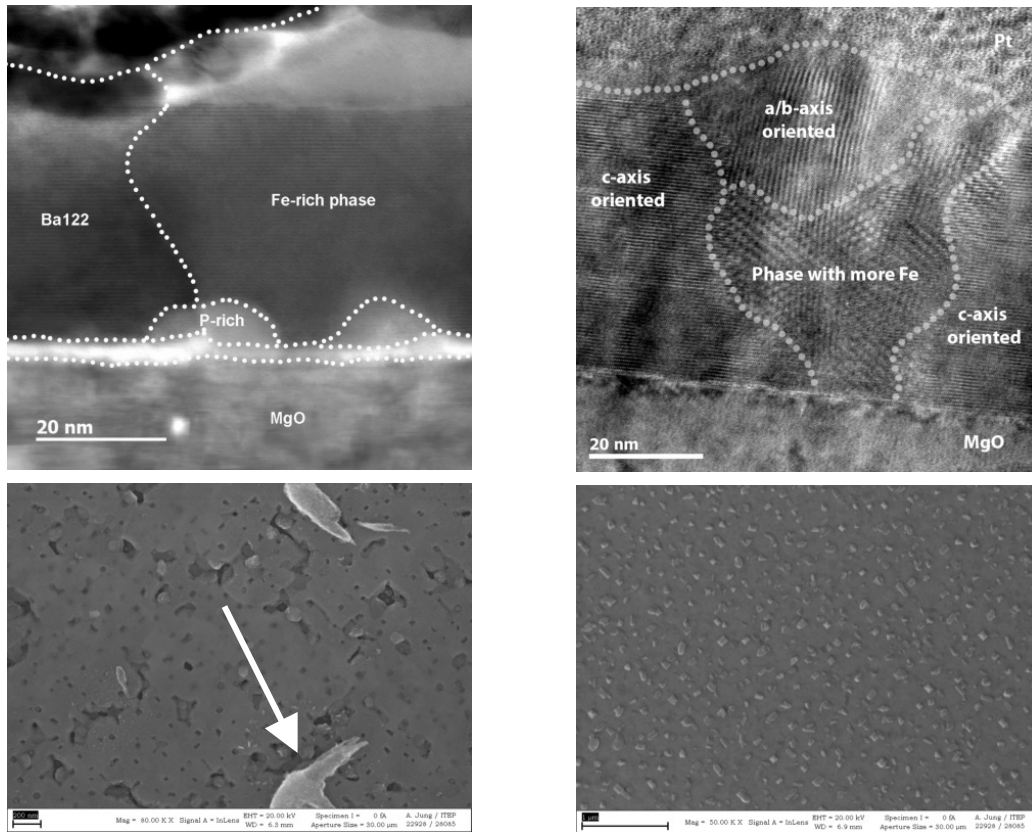


(c) Resistance R plotted as a function of the temperature T for Co-doped Ba122 on MgO substrates prepared at three different deposition temperatures and two different laser frequencies. (d) Resistance R plotted as a function of the temperature T for P-doped Ba122 on MgO substrates prepared at five different deposition temperatures and a laser frequency of 10 Hz.

Figure 2.1: Films of Co- and P-doped Ba122 were grown on MgO with 40 mJ respectively 35 mJ of laser energy with frequencies of 5 and 10 Hz at different growth temperatures which are listed in fig. 2.1.

As indicated in fig. 2.1c and fig. 2.1d, the $T_{c,0}$ -values of the films are up to 20 K. Those values correspond to the values reported in former investigations [98, 99, 100].

For the used experimental setup and using MgO as a substrate, the $T_{c,0}$ -values are the highest achievable. In case of Co-doped Ba122, a higher growth rate [64] is required, which can only be achieved with higher laser frequencies, since the maximum growth rate with this setup is 1 \AA/s . For P-doped Ba122, higher deposition temperatures above $1000 \text{ }^\circ\text{C}$ are necessary [52]. XRD patterns in fig. 2.1a show for $\text{Ba}(\text{Fe}_{0.92}\text{Co}_{0.08})_2\text{As}_2$ only (00l)-peaks, which indicate c-axis texture. Especially peaks of higher order (e.g. Ba122 (00 10) and (00 14)) are narrower and more visible at growth temperatures of $700 \text{ }^\circ\text{C}$ and 5 Hz . These films show a slightly higher critical temperature of above 19 K . For phosphorus-doped samples, the narrowest peaks can be achieved when depositing at $920 \text{ }^\circ\text{C}$ (see fig. 2.1b). Noticeable is the presence of the Fe (200) peak for Co-doped samples. This peak cannot be observed for samples doped with phosphorus.



(a) HR-STEM (top) and SEM (bottom) image of a P-doped Ba122 sample. Different phases are labelled in white. The precipitates on the surface are marked with the white arrow. The magnification level for the SEM image is a factor of 80,000 and the acceleration voltage is set to 20 kV .

(b) HR-STEM (top) and SEM (bottom) image of a Co-doped Ba122 sample. Different phases are labelled in white. The pyramidal precipitates on the surface are visible. The magnification level for the SEM image is a factor of 50,000 and the acceleration voltage is set to 20 kV .

Figure 2.2: Scanning electron microscopy and transmissive electron microscopy images of a P-doped Ba122 and a Co-doped Ba122 on MgO sample.

TEM investigations show different impurities, such as Fe-rich phases and a thin light grey Fe interlayer between substrate and film. For $\text{Ba}(\text{Fe}_{0.92}\text{Co}_{0.08})_2\text{As}_2$, TEM images

(see fig. 2.2 a) and 2.2 b)) show a thinner Fe interlayer than for $\text{BaFe}_2(\text{As}_{0.6}\text{P}_{0.4})_2$. Furthermore, more and bigger Fe-rich phases can be seen from the surface as pyramidal structures (SEM) as well as in the cross section (TEM) (see fig. 2.2 b and c). The formation of those phases happens most likely due to the high lattice parameter misfit of 6 % of MgO compared to Ba122 [101]. The observed (200) Fe peak in XRD patterns, however, cannot be caused by the Fe interlayer. A simple peak-width estimation with the Scherrer-formula [102, 103] results in an expected width of the Fe peak of around 6° for 2 nm thickness as measured for the Fe interlayer. The (200) Fe peaks show a full width at half maximum (FWHM) of around 0.8° . Therefore, the Fe-rich grains in the film must be the reason for the observed peak. On top of those Fe-rich phases, often a/b-oriented grains develop and are visible as pyramidal precipitates in the SEM image at the surface due to their orientation (fig. 2.2 b). In case of phosphorus doped films Fe-rich phases are visible as precipitates on the surface as indicated by the white arrow in fig. 2.2 a). A possible reason for not observing such an Fe-peak in phosphorus-doped samples on MgO may be the unoriented or amorphous growth of Fe-rich grains. C-oriented growth would result in a peak in the XRD pattern. Perhaps, different iron phosphate compounds form, due to phosphorus' high reactivity [104] and are included in the Ba122 matrix.

	Fe content (mol%)	Ba content (mol%)	ratio (Fe+Co)/Ba
A	65.93	28.56	2.44
B	41.68	14.26	3.04
C	41.50	19.90	2.25
Used target surface	36.94	19.57	2.05
Used target side	36.58	19.73	2.02
Unused target	36.39	19.97	1.98

Table 2.1: Iron and barium content displayed next to the ratio of iron and cobalt to barium for different Co-doped samples A, B, C and different spots on the $\text{Ba}(\text{Fe}_{0.92}\text{Co}_{0.08})_2\text{As}_2$ target.

The ICP-MS analysis of various samples found that the amount of iron and cobalt in the films is slightly increased, compared to the values of the target material (table 2.1). The average iron and cobalt to barium ratio is 2.57. This is 28 % higher than the nominal ratio of 2. This happens most likely because Barium re-evaporates from the sample surface due to its high vapor pressure [105] which leaves a Barium-poor film. Additionally, the correctness and stability of the ratio in the target material was verified, even after extensive usage.

Dai et al. [106], who also use the 355 nm laser, found in 2018 Fe^0 in their films by X-ray photoelectron spectroscopy (XPS) and correlated this with the appearance of the Fe peak in the XRD pattern. With a similar experimental setup through TEM and ICP-MS measurements, it was possible to show that their findings on strontium titanate (SrTiO_3 , abb.: STO) are reproducible with MgO and that the Fe peak in the

XRD patterns are caused by the Fe-rich phases within the superconducting film and not by the Fe interlayer between substrate and film.

2.2.2 Irreproducibility on MgO

After two series of Ba122 on MgO, it was not possible to reproduce the results mentioned before (see fig. 2.3). The T_c -values did not reach the expected values around 20 K again. The parameter window for good results is very narrow as shown in chapter 2.2.1. The T_c -values for small changes of temperature as well as for frequency show broad deviation.

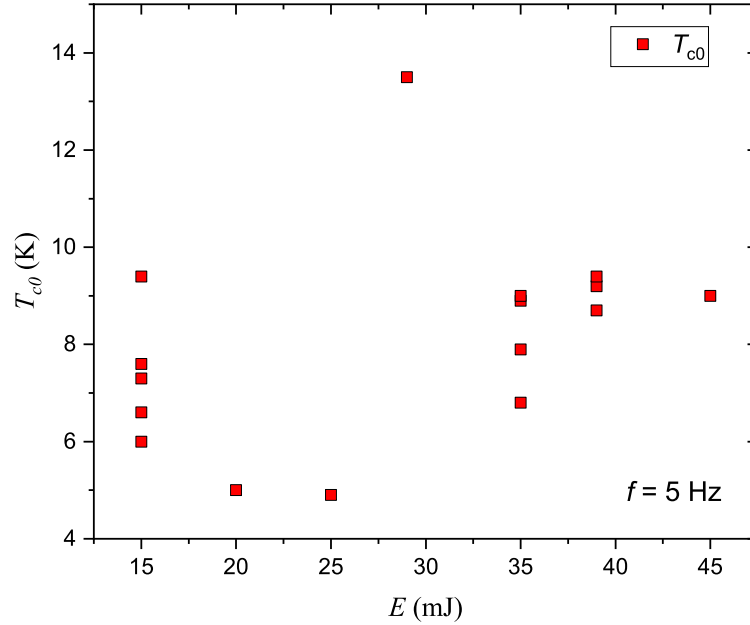


Figure 2.3: Critical temperature T_{c0} of several Ba122 samples grown on MgO as a function of the used laser energy E .

ICP measurements on MgO (see tab. 2.2) showed that the single crystalline substrate includes especially Fe, supposedly responsible for growth inhibition.

Element	detection limit	measured value
Fe	0.00068	0.00837
Co	0.00005	< 0.00005
As	0.00012	< 0.00012
Zr	0.0004	< 0.0004
Ba	0.00012	< 0.00012

Table 2.2: ICP measurement results of a blank MgO substrate; all values are specified in mass fraction.

This might explain the increased growth of Fe-rich precipitates inside the films (see fig. 2.2 a) and b)). A further consideration could be that the growth rates, which depend on laser frequency and energy are low in comparison to previous reports [98]. The growth rates correspond directly to the amount of material arriving at the substrate, thereby establishing a direct correlation between laser frequency - higher laser frequency means more often per time material is ablated- and laser energy -more energy results in more

material being ablated and arriving with higher speed and therefore with higher probability at the substrate surface. Consequently, due to low laser energy some molecules are more likely to arrive at the substrate surface than others or different molecules arrive at different times, creating a heterogeneous distribution of molecules and atoms or wrong stoichiometry in the film. In addition to this, it is possible that the applied MgO substrates had varying qualities and purities throughout different production batches.

2.2.3 LAO and CaF₂ as substrates

Since the deposition on MgO could not be reproduced, other substrates were tested. The decision was made to experiment with LAO and CaF₂. As described before in chapter 1.2.4.2, LAO and CaF₂ show comparable mechanical and chemical properties as MgO, despite the brittleness of CaF₂. Furthermore, ICP measurements on blank substrates showed no significant amount of impurities which could disturb the growth (see tab. 2.3). For CaF₂ the measured amounts were all below the detection limit. However, for LAO only the measured values of Fe and Ba were above the detection limit while the values for Co, As and In were below detection limit. The values for Fe and Ba in the LAO substrates were significantly low in comparison to the Fe and Ba values measured for MgO substrates (see tab. 2.2) and should not have any influence on the growth.

Element	detection limit	measured value
Fe	0.0004	< 0.0004
Co	0.00012	< 0.00012
As	0.0004	< 0.0004
In	0.000005	< 0.000005
Ba	0.00012	< 0.00012

(a) ICP measurement results of a blank CaF₂ substrate; all values are specified in mass fraction.

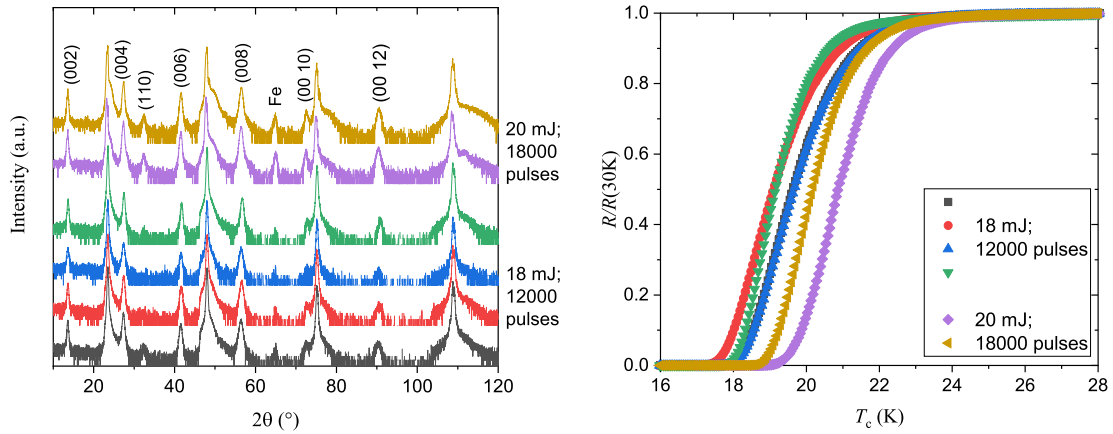
Element	detection limit	measured value
Fe	0.0002	0.0005
Co	0.00004	< 0.00004
As	0.0002	< 0.0002
In	0.0004	< 0.0004
Ba	0.000004	0.00009

(b) ICP measurement results of a blank LAO substrate; all values are specified in mass fraction.

Table 2.3: ICP measurement results of a) CaF₂ and b) LAO substrates.

Moreover, reports indicate that Ba122 was successfully grown on LAO [70] and CaF₂ [74, 19]. Based on these findings, the decision was made to focus on Co-doped Ba122 due to more manageable deposition temperatures around 700 to 800°C. The use of P-doped Ba122 with optimal deposition temperatures [52] could not be realized, as the heat shielding of the substrate heater cannot withstand temperatures over 900 °C.

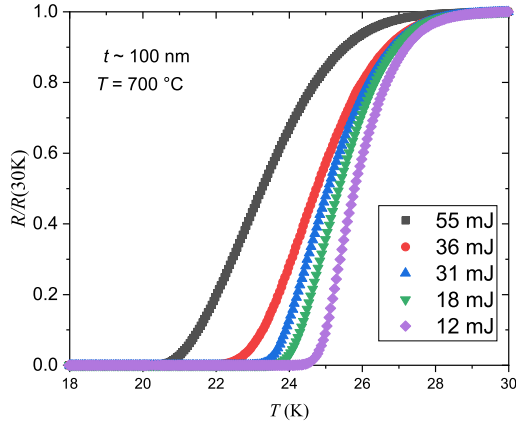
For the used experimental setup several temperatures and energy levels were examined for both substrates. For LAO, the best growth could be observed at deposition temperatures of 750 °C and laser energies of 20 mJ at the target. Since the growth rate was too low, the highest possible laser frequency of 10 Hz was chosen. The heater target distance was 40 mm.



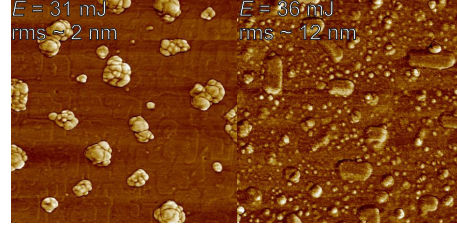
(a) $\theta - 2\theta$ scans of Co-doped Ba122 on LAO substrates, (b) Normalized resistance R plotted as a function of the temperature T for Co-doped Ba122 on LAO substrates, prepared with two different numbers of pulses and two different laser energies at deposition temperatures of 750 °C. The intensity is plotted as a logarithmic function of the angle 2θ .

Figure 2.4: a) $\theta - 2\theta$ scans of Co-doped Ba122 on LAO substrates; b) Resistance R plotted as a function of the temperature T for Co-doped Ba122 on LAO substrates.

Thicker films (18,000 pulses) (see fig. 2.4a) grown with slightly higher laser energy were observed to unveil sharper Ba122 peaks in the $\theta - 2\theta$ scan, especially for higher orders like (00 12). Remarkably, those films exhibited a (110)-orientation. There is currently no evidence whether “the growth mode transition from a layer growth mechanism with $c/2$ ledge heights to a three-dimensional growth with (110)-oriented precipitates is misfit-driven, supersaturation-driven or a mixture of both” [19, p. 7]. The (110)-orientation was observed in the plots for the films grown with 18 mJ, though not as prominent. The films with a higher amount of pulses and higher laser energy also showed higher T_c -values (see fig. 2.4b). For CaF_2 the best film properties were achieved with deposition temperatures of 700 °C and laser energies of 30 mJ. The laser frequency and the heater target distance was kept identical to 10 Hz and 40 mm.



(a) Normalized resistance R plotted as a function of the temperature T for Co-doped Ba122 on CaF_2 substrates prepared with different laser energies at deposition temperatures of 700 °C and thicknesses of around 100 nm.



(b) AFM images of two Co-doped Ba122 on CaF_2 substrates prepared with different laser energies at deposition temperatures of 700 °C and thicknesses of around 100 nm. The roughness rms and the laser energy E are displayed in white.

Figure 2.5: a) Resistance R plotted as a function of the temperature T for Co-doped Ba122 on CaF_2 substrates; b) AFM images of two Co-doped Ba122 on CaF_2 substrates.

For films on CaF_2 , T_c -values were observed to be higher and therefore more promising than films grown on LAO, since the planned implementation of BHO and BZO particles as pinning centers reduced the T_c -value according to the doping level. Thus, extensive work was performed on optimization and characterization of Co-doped Ba122 films on CaF_2 [19]. Lower laser energies, respectively lower growth rates, showed higher T_c values. However, films grown with lower energies unveiled more BaF_2 precipitates on the surface (see fig. 2.5b), creating strain and therefore possible growth-induced pinning centers. Examinations showed that the formation of BaF_2 increases the T_c -values due to strain (see fig. 2.5a), but also increases surface roughness (see fig. 2.5b). Therefore, a compromise was taken to apply the parameters mentioned above to obtain minimal strain in the film and maximum possible T_c -values. The growth mode of films grown at 31 mJ laser energy and 10 Hz repetition rate is a layer growth mechanism with $c/2$ -ledges [19] and therefore optimal for quasi-multilayer deposition with equally distributed nanoparticles between closed layers of superconducting compound. However, the superconducting current carrying capacity and pinning force enhancement by implementing nanoparticles should be examined further on, while the strain and other possible reasons for pinning center have to be eliminated. Finally, CaF_2 can be more easily acquired commercially than LAO, making it more favorable.

2.2.4 Conclusion

The first experiments aimed at ensuring the reproducibility of a superconducting Ba122 film on a suitable substrate for the existing experimental setup. It was possible to grow superconducting Co- and P-doped Ba122 films on MgO, however the reproducibility was limited by a very narrow parameter window and changing quality of the substrates.

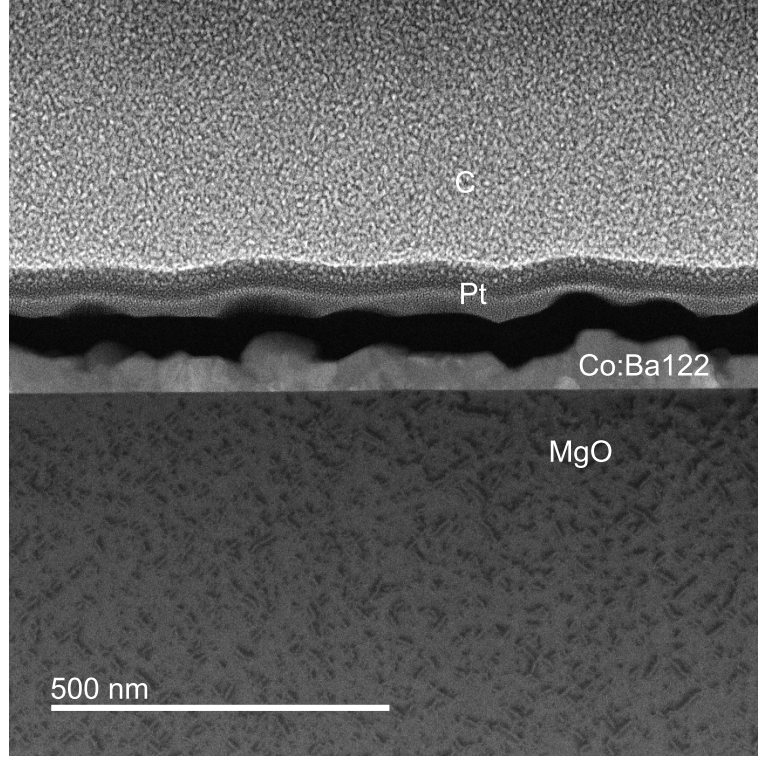


Figure 2.6: HR-STEM image of a Co-doped Ba122 sample grown on MgO. The film thickness varies throughout the whole film. Different phases, orientations and precipitates are visible.

The TEM measurements (see e.g. fig. 2.6) of the films on MgO often revealed impurity phases and orientations, due to the impurity atoms or elements present at the surface of the substrate. Lee et al. already found BaFeO_3 in BaTiO_3 template films [62]. The film thicknesses with 50 to 100 nm as well as their superconducting properties, such as T_c of around 20 K, were in the same range as reported in the literature [25, 107, 97]. The forming of a thin Fe layer could be observed, yet this layer was not linked to the visible Fe peak in the corresponding X-ray diffractograms. Large Fe phases formed in the films were the reason for the formation of such an Fe peak which could be proved by TEM measurements and Nelson-Riley calculations. Due to the experimental setup and the available temperatures and energies the decision was made to use Co-doped Ba122 since the deposition temperature is lower and can be easily handled with the heater.

To find a suitable substrate with satisfying properties to grow reproducibly good quality iron-based superconducting films, LAO and CaF_2 were tested. It was achieved to prepare and investigate reproducibly good quality films. The X-ray investigations

showed the expected c-axis oriented layer growth mode and $R(T)$ -measurements revealed the critical temperatures in the range of the samples reported in the literature. The chemical stoichiometry measurements showed less impurity atoms or elements in the substrates compared to MgO, thus maintaining the reproducibility of the substrate quality.

2.3 Pulsed Laser Deposition of quasi-multilayer superconducting $\text{Ba}(\text{Fe}_{0.92}\text{Co}_{0.08})_2\text{As}_2$ - BaHfO_3 and $\text{Ba}(\text{Fe}_{0.92}\text{Co}_{0.08})_2\text{As}_2$ - BaZrO_3 nanocomposite films

With the quasi-multilayer PLD technique Co-doped Ba122 films with the before mentioned optimal parameters were prepared, incorporating BHO and BZO as pinning material. Since the targets have to be exchanged quickly during deposition to avoid re-evaporation from the substrate, the right thickness parameters for each quasi-layer had to be identified as well. The number of pulses had to be adjusted, so the Ba122 layer is not too thick or too thin, enabling the nanoparticles to be equally distributed in the film. The same applies for the BHO and BZO deposition, because the quasi-layer of BHO or BZO should not be a fully closed layer, but consists only of particles with the optimal distance to each other. The installation of a laser shutter was very important to achieve an exact number of pulses for each target to obtain reproducibility. The installation in a very small space and the connection to the used deposition software and infrastructure was challenging since the laser, the target movement and the shutter had to be synchronized. The shutter has to close and shut a laser pulse repeatedly with a very high energy of 15 J/cm^2 under 1/10 of a second.

The first series of films were prepared with the following procedure:

125 pulses on the Ba122 target followed by 12 to 20 (one amount was chosen for each sample) pulses of BHO respectively BZO. This exchange pattern was repeated 99 times and was followed by a cap layer of Ba122, consisting of 125 pulses. The parameters such as energy, frequency, temperature and distance were taken from the optimal samples mentioned in the previous chapter. Since the laser is not capable of changing the energy during the deposition, the same energy, frequency, temperature, target heater distance was employed during the whole process.

The film thicknesses were determined ex-situ by AFM measurements to 13.4 - 20.6 nm. As exemplary displayed in fig. 2.8, the T_c -values decrease extremely for a small difference of pulses on the BHO or the BZO target. As Lee et al. [23] showed, the T_c -values should only decrease by a couple of Kelvin for significant changes in doping level. Thus, a possible explanation for the extreme decrease can be found in the film thickness of only maximum 20 nm. A small amount of nanoparticles can strongly disturb the lattice and therefore the superconductivity. Conclusively, the procedure was changed to 125 pulses on the Ba122 target followed by 12 to 80 pulses of BHO, respectively BZO. This was repeated 143 times, followed by a cap layer of Ba122 of 125 pulses. This amounts to an equivalent of 18,000 pulses of Ba122 and should ensure a constant film thickness of around 70 nm and a deposition rate of 0.6 \AA/s with a pulse energy of 20 mJ at target or 2.0 J/cm^2 .

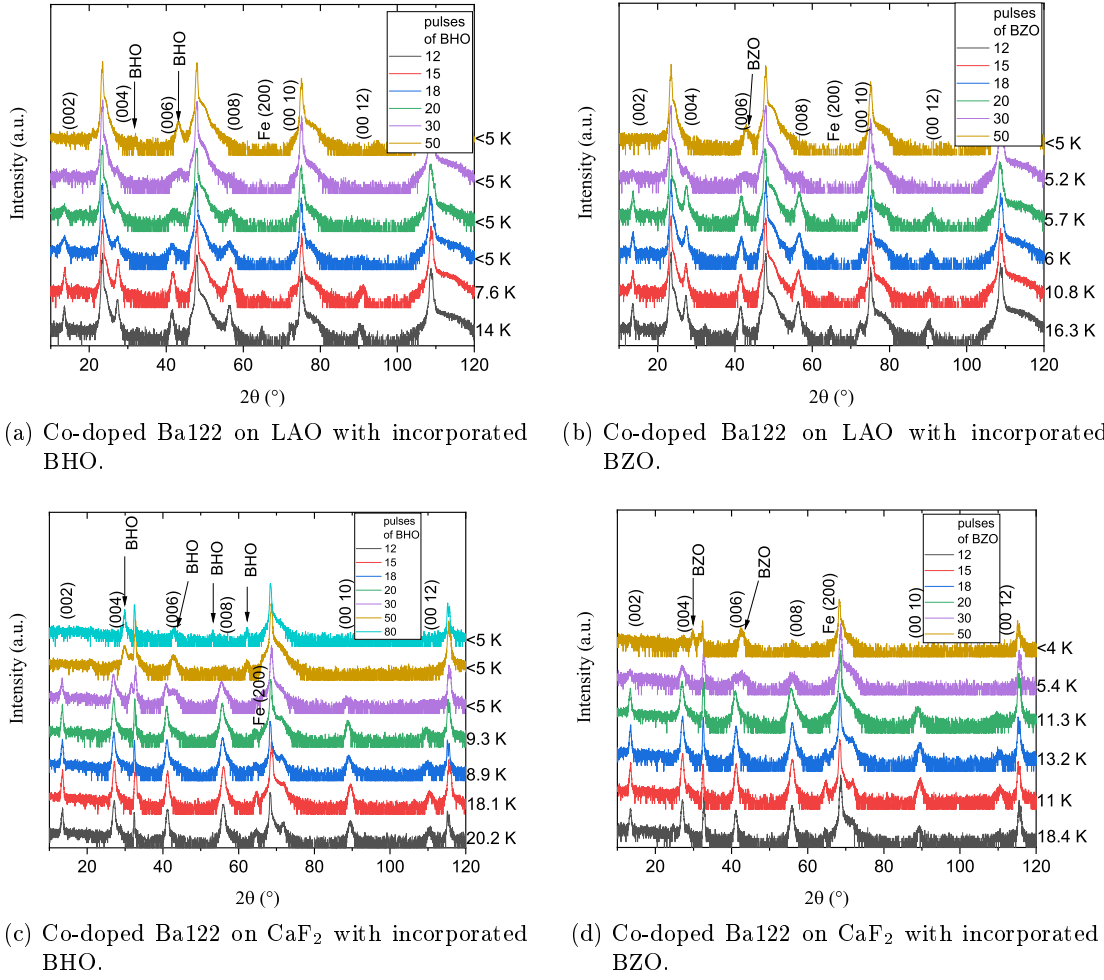


Figure 2.7: $\theta - 2\theta$ scans of Co-doped Ba122 on LAO (a) and b)) and CaF₂ (c) and d)) substrates with incorporated BHO (a) and c)) and BZO (b) and d)). The intensity is plotted as a logarithmic function of the angle 2θ . It was shown that the process of Ba122 growth is reproducible with the chosen substrates and shows high enough T_c -values, allowing perovskite implementation to not decrease the superconducting properties too strongly.

As shown by the $\theta - 2\theta$ scans the procedure was not successful. The BHO peaks (see fig. 2.7a) can only be observed at a pulse amount of 50 pulses of BHO. The structure of Ba122 is meanwhile no longer recognizable. For lower doping levels, the Ba122 structure is still maintained, but no BHO peak is visible.

A similar picture is observed for BZO (see fig. 2.7b). The BZO peak slightly appears at the highest tested doping level while the Ba122 structure vanishes with increasing doping level. The T_c decrease is again very high, even though it is slightly less steep for BZO than for BHO.

Measurements on CaF₂ result in similar findings (see fig. 2.7c and 2.7d). For BZO doping, the decrease of T_c is not as steep as for BHO. The Ba122 structure nevertheless vanishes at high doping levels for both pinning materials. However, there is a difference

in the $\theta - 2\theta$ scans in comparison to LAO. The BZO, respectively the BHO peaks appear more evident and sharp.

For both substrates, a vanishing iron peak as well as Ba122 peaks can be observed with increasing doping level. This happens most likely due to an increasing disorder in the films with increasing BHO and BZO content. The Ba122 no longer grows c-axis oriented at high perovskite contents, therefore c-axis oriented Fe-rich phases do not form either. Only BHO and BZO grow in c-direction.

The thicknesses of the films are determined by AFM to approximately 70 nm.

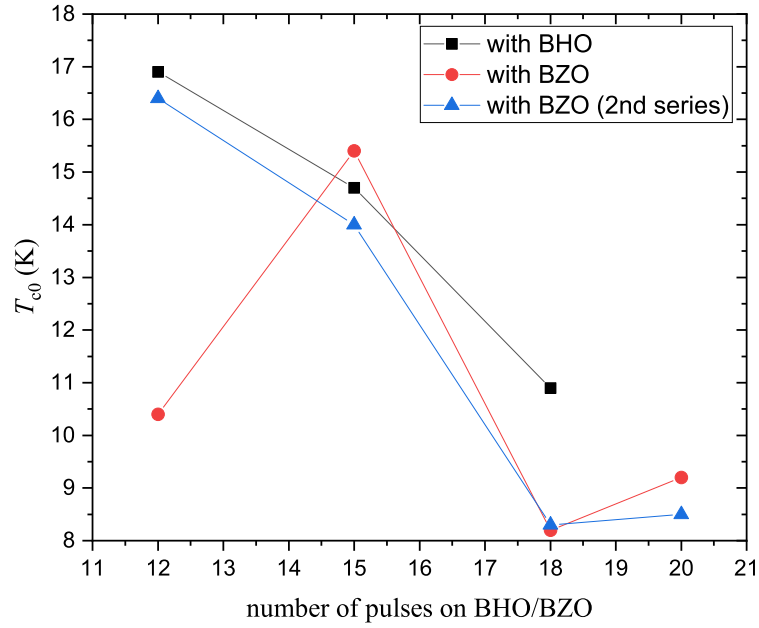
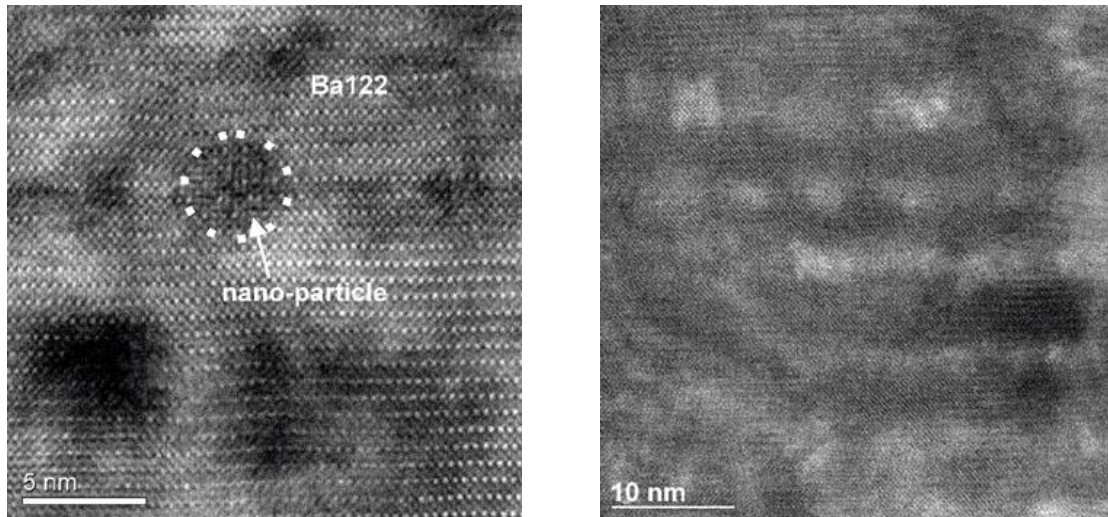


Figure 2.8: Critical temperature T_{c0} of several Ba122 samples grown on LAO with incorporated BHO and BZO as a function of the number of laser pulses on the BHO or BZO target of each iteration.

2.3.1 Experiments for optimization of homogenous distribution of BHO nanoparticles on CaF_2

Based on the knowledge of the previous results, nanocomposite films of $\text{Ba}(\text{Fe}_{0.92}\text{Co}_{0.08})_2\text{As}_2$ with BHO nanoparticles with film thicknesses between 35 and 110 nm were prepared by quasimultilayer pulsed laser deposition technique on CaF_2 substrates. Laser energy of 3.0 J/cm^2 , respectively 30 mJ at target, with a repetition rate of 10 Hz, was applied. The substrate-target distance was again 40 mm. The target diameter of the $\text{Ba}(\text{Fe}_{0.92}\text{Co}_{0.08})_2\text{As}_2$ was 10 mm and 1 inch (25.4 mm) for BHO. The deposition rate was 0.9 \AA/s .

Initially, the quasi-multilayer technique was used by implementing 2 mol% of BZO into the matrix. The results show that nanoparticles (see fig. 2.9a) form similar to the films of Lee et al. [23] in a nicely epitaxially grown Ba122 matrix. The BZO content was calculated from ICP measurements.



(a) HR-STEM image of a sample with 2 mol% of BZO in the Co-doped Ba122 matrix deposited on CaF_2 .

(b) HR-STEM image of a sample with 2 mol% of BHO in the Co-doped Ba122 matrix deposited on CaF_2 .

Figure 2.9: High Resolution-Scanning Transmissive Electron Microscopy (HR-STEM) image of two sample with 2 mol% of BZO (a)) and BHO (b)) in the Co-doped Ba122 matrix.

It could also be shown, that samples grown with 2 mol% of BHO, identically to the samples with implemented BZO, also exhibited nano-particles as cloudy artefacts in the TEM measurements (see fig. 2.9b).

After this finding, several quasi-multilayered films with different doping levels of BHO (0 mol%, 1.03 mol%, 1.59 mol%, 3.85 mol%) were prepared and investigated. The total number of $\text{Ba}(\text{Fe}_{0.92}\text{Co}_{0.08})_2\text{As}_2$ pulses of 18,000 was not changed in order to keep the (superconducting) film thickness constant. The total amount of BHO was controlled by the number of BHO interlayers of constant 12 pulses BHO per layer. For 1.03 mol% the targets were exchanged nine times and a cap layer of 1,800 pulses of Ba122 was

added. The number of exchanges for 1.59 mol% amounted to 39 and the Ba122 cap layer consisted of 450 pulses. For 3.85 mol% of BHO, 143 exchanges and a cap layer of 125 pulses was deposited. As shown in fig. 2.9b, the formation of nanoparticles in the Ba122 matrix could be observed at a doping level of 2 mol% of BHO, similar to BZO. The BHO contents were determined by EDX measurements in TEM.

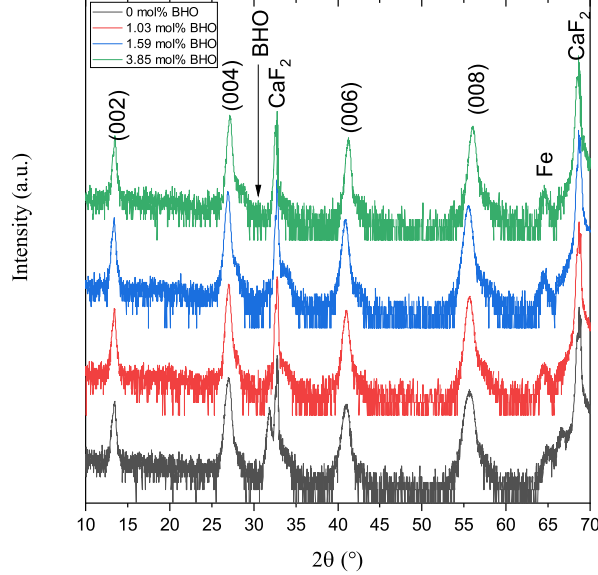


Figure 2.10: θ - 2θ scans of $\text{Ba}(\text{Fe}_{0.92}\text{Co}_{0.08})_2\text{As}_2$ films grown on CaF_2 with different doping levels of BHO.

The $\theta - 2\theta$ scans in fig. 2.10 indicate c-axis texture of each film. The pristine film shows some secondary phases at 33° and 67° . The original structure of the $\text{Ba}(\text{Fe}_{0.92}\text{Co}_{0.08})_2\text{As}_2$ is preserved throughout the different doping levels. A slight hint of a BHO peak can be observed for 3.85 mol% BHO at an angle of around 30° . The peaks tend to shift ca. 0.5° to higher angles at a doping level of 3.85 mol%, which indicates a reduction of the c-axis parameter (1.31972 nm to 1.31097 nm). The pristine film already grows a/b-strained due to lattice misfit of the Ba122 to the substrate surface, since the c-axis parameter of the pristine sample (1.31972 nm) is significantly higher than for unstrained Ba122 (see chap. 1.2.3). A possible reason can be found in the growth of c-directional nanocolumns throughout the whole film in the sample with 3.85 mol% BHO. The nanocolumns create a certain space for the film to grow in between, which apparently happens to have a better misfit than the substrate lattice to the film lattice and therefore creating a relaxation of the a/b-strain, which results in the observed decrease of the c-axis parameter.

The $T_{c,0}$ -values (see fig. 2.11) decrease with increasing doping level as expected and reported before [108]. Only at a very low doping level, the $T_{c,0}$ value slightly increases above the value of the pristine $\text{Ba}(\text{Fe}_{0.92}\text{Co}_{0.08})_2\text{As}_2$ film. The difference is just 0.9 K and therefore within the usual experimental scatter.

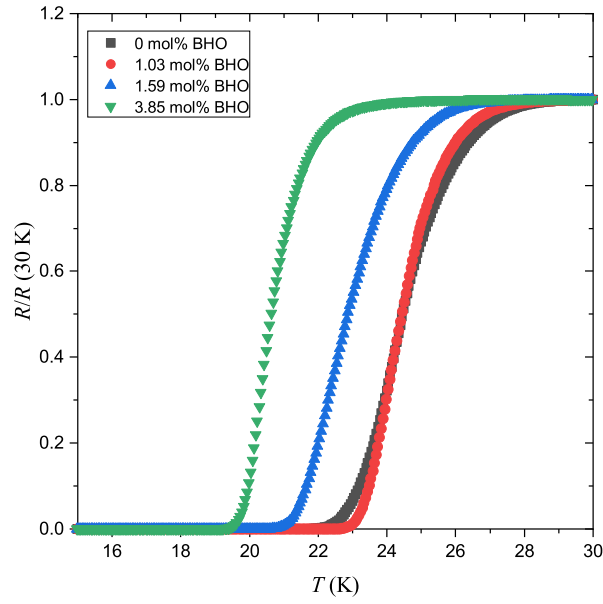
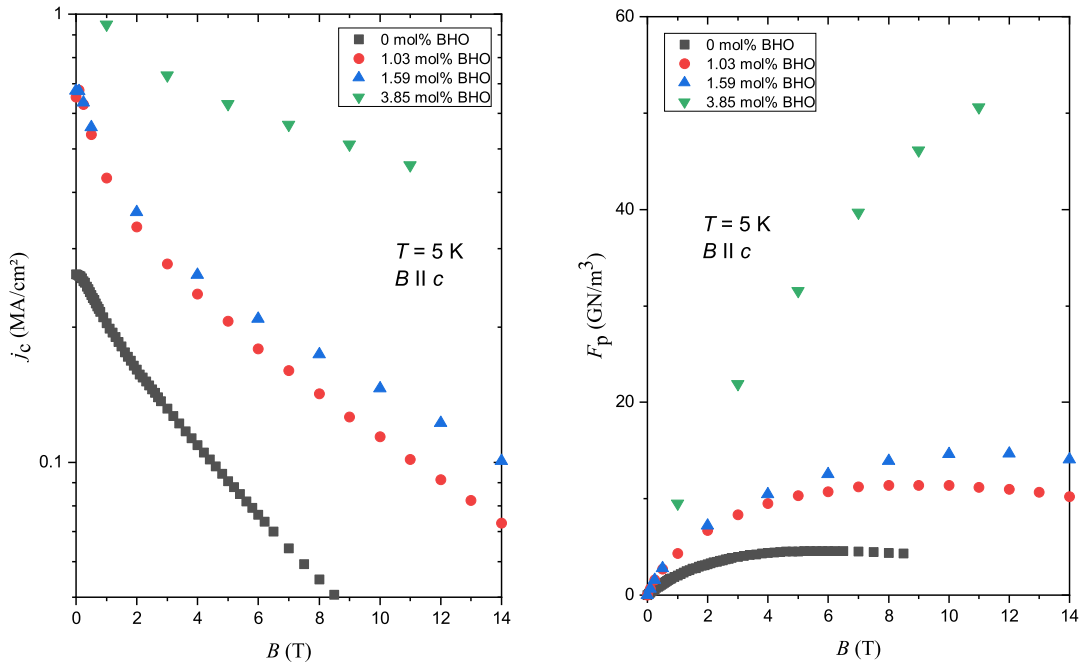


Figure 2.11: Temperature dependence of the resistance normalized to the value above 30 K for three different levels of incorporated BHO in Co-doped Ba122 films grown on CaF₂.



(a) Critical current density j_c plotted as a function of the external magnetic field. (b) The pinning force density F_p plotted as a function of the external magnetic field.

Figure 2.12: a) Critical current density j_c and the b) pinning force density F_p plotted as a function of the external magnetic field for three different levels of incorporated BHO in Co-doped Ba122 films grown on CaF₂. The samples were measured at 5 K with an applied external magnetic field parallel to the c-axis in the film.

The critical current density j_c reveals the expected behavior of the superconducting films caused by doping (see fig. 2.12a). The critical current density j_c increases significantly with increasing doping level and almost reaches 10^6 A/cm² for the highest doping level of 3.85 mol% and an external magnetic field of 0 T. Due to low growth rates, as explained in chap. 2.2.1 and reported by [64], j_c and $T_{c,0}$ of the pristine film are relatively low, but are the optimum which can be achieved with the deposition setup, since the laser frequency is already maximum of 10 Hz. The low growth rate has a negative influence on the crystal growth of the film and therefore reduces the superconducting properties. The pinning force F_p (see fig. 2.12b) also increases with the doping level and reaches 50.6 GN/m³ at 11 T and a doping level of 3.85 mol%. The literature data on BaZrO₃-added Ba(Fe,Co)₂As₂ reports values of 170 GN/m³ for 2 mol% and 30 GN/m³ for 4 mol% at 11 T and 4.2 K [23]. For BaFe₂(As,P)₂ films values of 58 GN/m³ at 9 T and 5 K [20] and recently 189 GN/m³ at 9 T and 4 K [24]) have been reported. The reported films were prepared with premixed targets. Maximum peaks in the pinning force densities were observed to shift to higher applied magnetic fields with increasing BHO content. The results, which have been mentioned so far in this chapter, have already been published (see [109]).

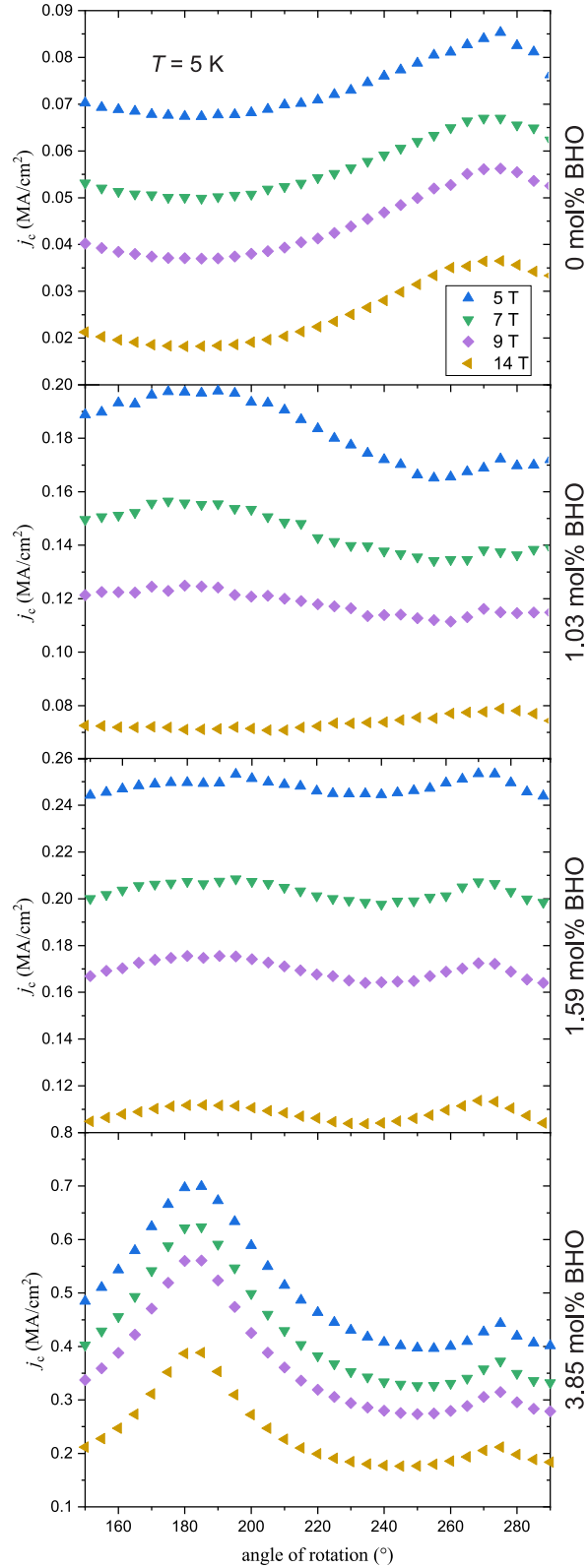


Figure 2.13: Anisotropy plots measured at 5 K for applied magnetic fields of 5, 7, 9 and 14 T for three different levels of incorporated BHO in Co-doped Ba122 films grown on CaF_2 . The critical current density j_c is plotted as a function of the rotation angle in an applied external magnetic field.

The j_c -values were also measured for different applied magnetic fields and for angles in the range of 150 to 290 ° in the magnetic field for all samples. For the pristine sample, a strong peak at 270 ° can be observed, which corresponds to the a/b-plane in the film, indicating intrinsic pinning. These peaks show in all samples. These findings fit to the results of the XRD measurements of these films (see fig. 2.10), indicating a pristine a/b-directional strain due to lattice misfit of the Ba122 to the substrate surface. However, with increasing BHO content a peak at 180 ° is appearing more and more significantly. This angle corresponds to the c-direction in the film. For a content of 3.85 mol% of BHO, the peak is evidently higher than the peak for the a/b-plane and significantly sharp in comparison to the other samples with lower BHO content. It has already been shown by XRD investigation (see fig. 2.10) that implementation of BHO results in c-axis parameter decrease. A possible reason is growth of c-directional BHO nanocolumns with lengths in the range of the film thickness. This means, the increasing BHO content results in a higher pinning force density in the c-direction and therefore a higher critical current density caused by the pinning effect of the perovskite, which can be observed in this anisotropy graph (fig. 2.13).

For 1.03 mol% of BHO the c-peak vanishes at high magnetic fields of 14 T. This happens most likely due to more non-directional pinning centers such as globe shaped nanoparticles. Thus, it can be hypothesized that with increasing BHO content the c-axis pinning increases, because of the increasing growth of columnar pinning defects.

With measurements of $R(T)$ at different applied magnetic fields, the irreversibility field H_{irr} and the critical magnetic field H_{c2} were determined as indicated in the following fig. 2.14.

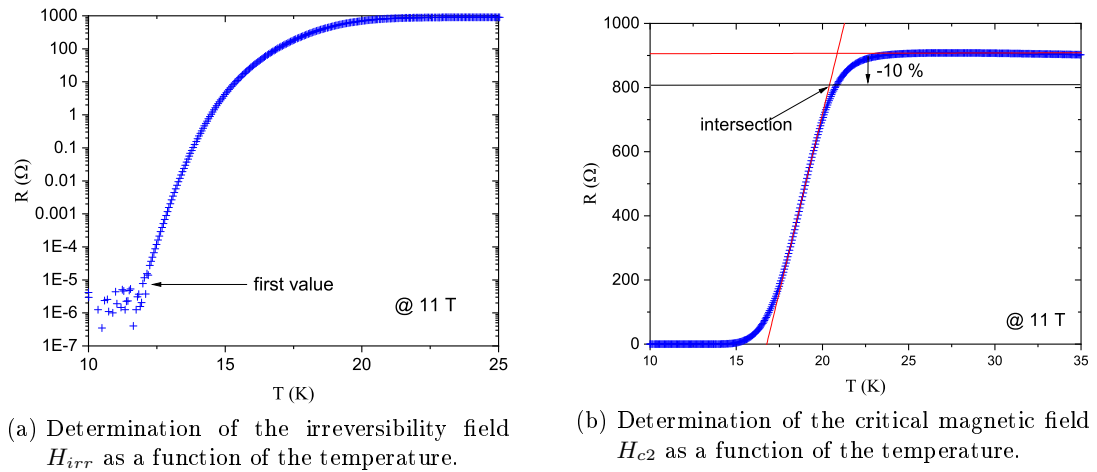


Figure 2.14: Graphic example of the determination of the irreversibility field H_{irr} and the critical magnetic field H_{c2} as a function of the temperature for a Co-doped Ba122 film grown on CaF_2 with 3.85 mol% BHO at 11 T.

H_{irr} is determined by plotting the resistance logarithmic as a function of the temperature for different applied magnetic fields. The first value that does not belong to the

noise of the superconducting state is the temperature corresponding to the value of the applied magnetic field (see fig. 2.14a). This is done for all used magnetic fields, with the magnetic field being plotted as a function of the determined temperature and the temperature normalized to $T_{c,90}$ (see fig. 2.15).

H_{c2} is determined with the same measurement data, but using a different analysis method. The resistance is plotted as a function of the temperature and a linear function is fitted to the slope. Thereafter, a linear function is fitted to the course of the normal conducting state and lowered to 90 %. The intersection of both linear functions is used to assign the temperature to the corresponding magnetic field (see fig. 2.14b). The magnetic field values are plotted as a function of the determined temperatures normalized to $T_{c,90}$ (see fig. 2.15).

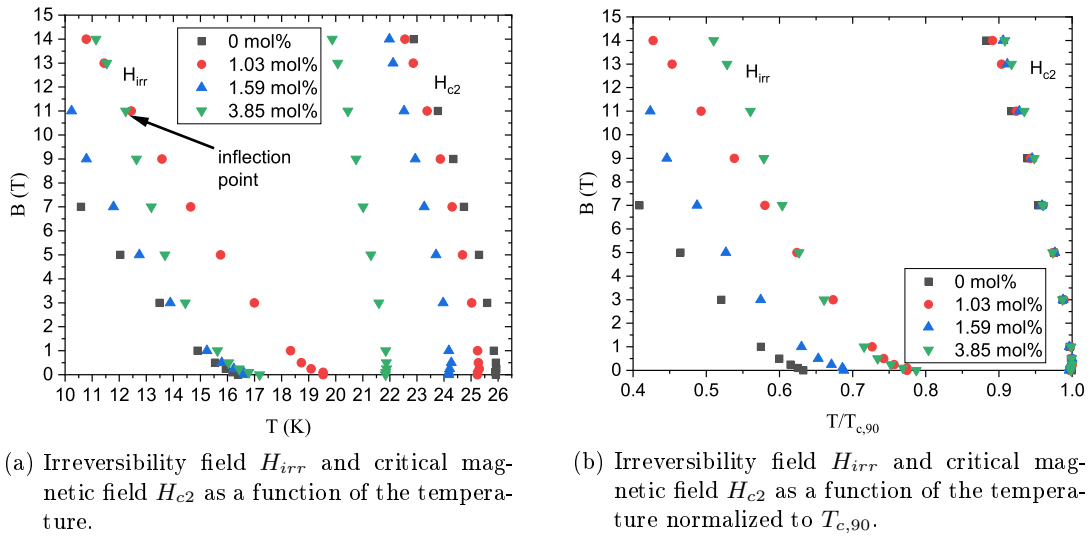
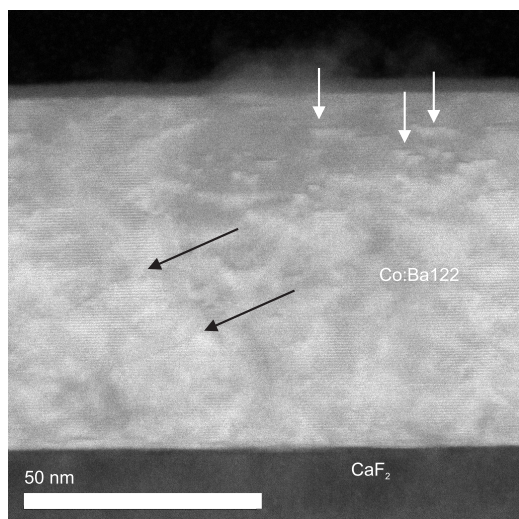


Figure 2.15: Irreversibility field H_{irr} and critical magnetic field H_{c2} as a function of a) the temperature and b) the temperature normalized to $T_{c,90}$ for three different levels of incorporated BHO in Co-doped Ba122 films grown on CaF_2 .

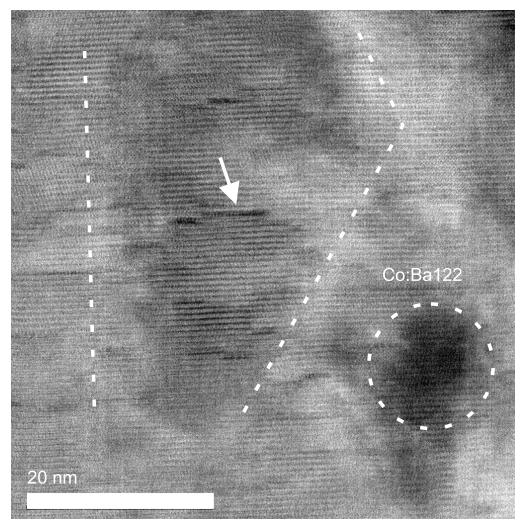
For H_{c2} , the values tend to decrease with a higher amount of BHO. The distances between the $H_{c2}(T)$ dependencies seem to correspond to the factors of BHO content increase. The normalized H_{c2} values rise with increasing doping level (see fig. 2.15b).

For H_{irr} curves a different picture emerges. The irreversibility line for 1.03 mol% is significantly higher than for the other samples (see fig. 2.15a). The normalized graph (fig. 2.15b) only shows the second highest irreversibility field. The highest T_c reduction takes place for the sample with the largest vortex glass phase (3.58 mol%). A possible reason for the higher irreversibility field of the 1.03 mol% sample, compared to the 1.59 mol% sample, might lie in the scatter of the quality of the films. 1.03 mol% may be an extraordinary good sample and 1.59 mol% may be an extraordinary bad sample for their BHO contents. More samples deposited with those parameters could show a better tendency. The other samples show an expected behavior and tend to produce

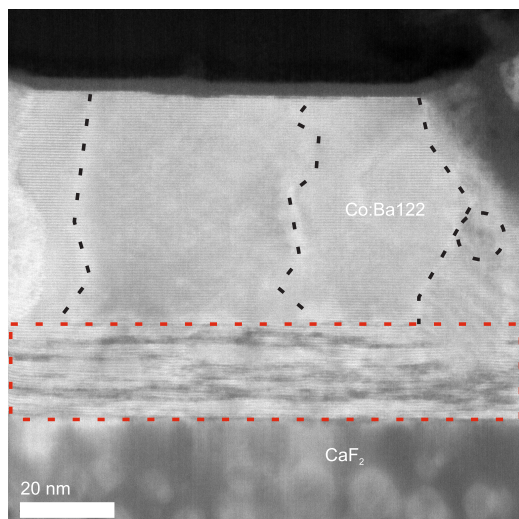
higher values with increasing BHO content. Furthermore, a bend or so called inflection point in the curve of the sample with the highest amount of 3.85 mol% is clearly visible (see fig. 2.15a). This behavior will be explained in the following sections.



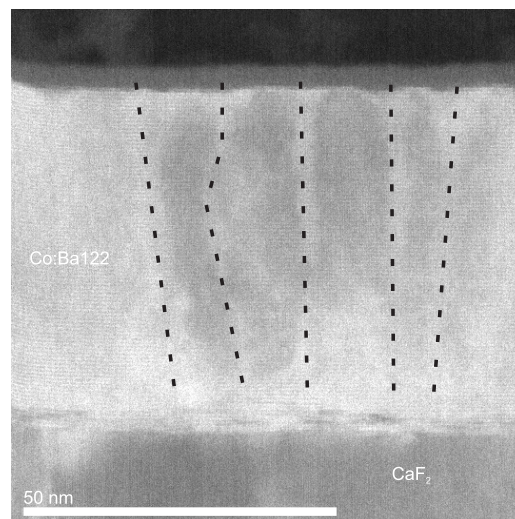
(a) HR-STEM image of a pristine Co-doped Ba122 sample deposited on CaF_2 . The cloudy contrast variations are due to the electron bombardment during the TEM investigation. White arrows indicate stacking faults and black arrows indicate grain boundaries.



(b) HR-STEM image of a Co-doped Ba122 sample with 1.03 mol% of BHO deposited on CaF_2 . White dashed lines indicate BHO nanocolumns. The white arrow points at stacking faults in the matrix and the white dashed circle indicates a BHO nano-particle.



(c) HR-STEM image of a Co-doped Ba122 sample with 1.59 mol% of BHO deposited on CaF_2 . Black dashed lines indicate BHO nanocolumns. The black dashed circle indicates a BHO nanoparticle. The area indicated by a red dashed line is a part of the sample which has been destroyed by electron bombardment during TEM investigation.



(d) HR-STEM image of a Co-doped Ba122 sample with 3.85 mol% of BHO deposited on CaF_2 . Black dashed lines indicate BHO nanocolumns.

Figure 2.16: HR-STEM images of Co-doped Ba122 samples with four different amounts of BHO deposited on CaF_2 .

The TEM images of all the investigated samples with different BHO levels are presented above in fig. 2.16. The pristine sample (fig. 2.16a) depicts some brighter areas and some cloudy contrast deviations, but the Ba122 structure is preserved throughout the whole film. The electron beam, creating the image, causes the contrast deviations, e.g. thickness variations in the lamella become visible. Some step defects and small angle grain boundaries can be observed, as indicated by the white and black arrows.

The sample with 1.03 mol% BHO content is exhibited in fig. 2.16b. Stacking faults, indicated by a white arrow, are visible in the whole film. Hints of non-directional nanocolumns (indicated by white dashed lines) are located in several spots next to nanoparticles with undefined shape (indicated here by a white dashed circle) with sizes of around 10 nm. Those nanocolumns cannot be grain boundaries, grain boundaries are displayed as sharper, thinner lines in the TEM images (e.g. see fig. 2.16a).

The image of the 1.59 mol% BHO sample (fig. 2.16c) displays a higher amount of c-directional nanocolumns aside nanoparticles of around 10 nm in diameter. The red dashed line indicates an area destroyed by the electron beam while taking the picture.

In fig. 2.16d, the sample with the highest amount of BHO, namely 3.85 mol%, is presented. Here, the nanocolumns are clearly visible in c-direction and with a defined diameter and distance to each other. This explains the very strong and sharp peak in the anisotropy graph in fig. 2.13, accounting for the strong c-axis pinning (see fig. 2.12b). These observations also fit to the hypothesis made on the basis of the XRD investigations, stating that a/b-directional strain relaxation is caused by long columnar defects. In addition to this, it could be shown that with increasing BHO content, the globe shaped defects reduce and more columnar defects appear as already presumed by the anisotropy results.

To prove that the nanocolumns consist of BHO EDX measurements were taken. As shown in fig. 2.17, the nanocolumns can be determined to consist of hafnium, oxygen and barium.

The samples with 1.03 mol% and 1.59 mol% slightly differ. The sample with more BHO in the film exhibits more nanocolumns, which are also accompanied by nanoparticles. This explains the small difference in their critical current density and pinning force density behavior.

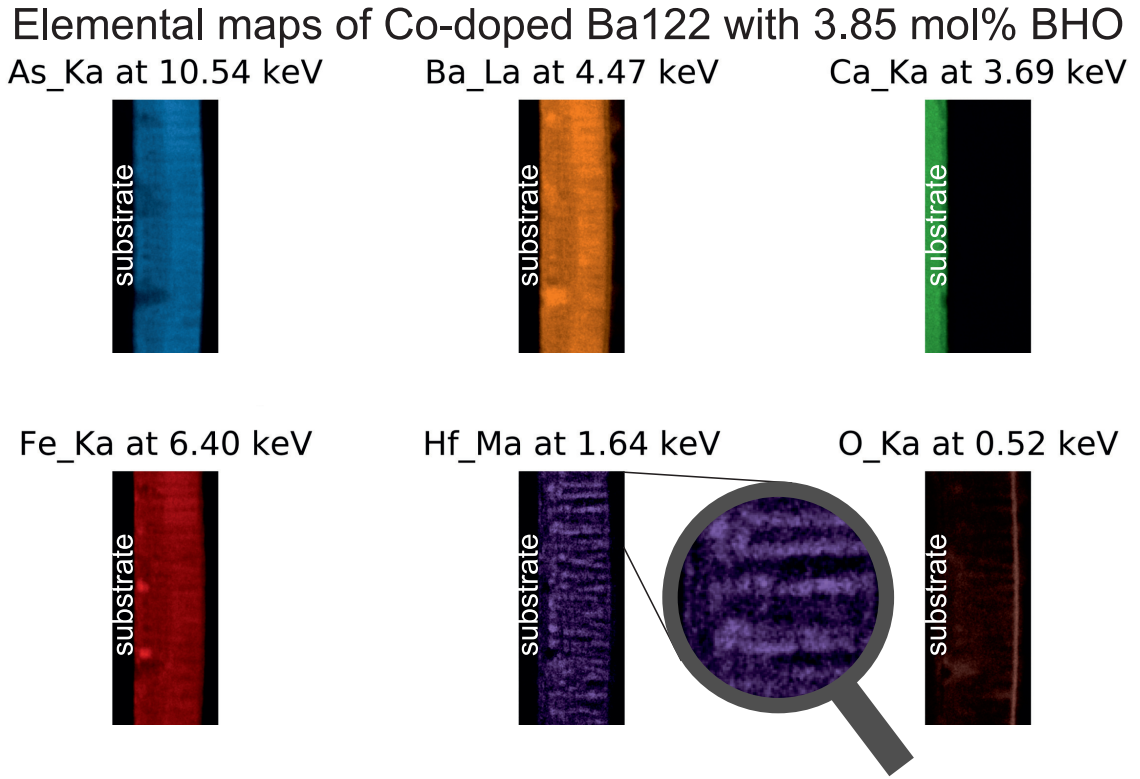


Figure 2.17: Elemental maps by EDX investigations on a Co-doped Ba122 sample with 3.85 mol% of BHO deposited on CaF_2 . The map features the different film elements displayed in various colours. The images are tilted clockwise. The substrate is located at the left edge of each image.

With the TEM images of these samples and the corresponding H_{irr} respectively H_{c2} graphs, it is possible to compare measured and calculated coherence lengths ξ and distances d between the pinning centers.

The calculation is explained in the following.

The upper critical magnetic field H_{c2} is defined as

$$H_{c2} = \frac{\Phi_0}{2\pi\xi^2}. \quad (2.1)$$

Considering the Werthamer, Helfand and Hohenberg model (WHH model) [110] the upper critical magnetic field at zero temperature can be estimated as

$$H_{c2}(0) = 0.69 \cdot m \cdot T_{c,90}, \quad (2.2)$$

where m is the slope of a linear fit of $H_{c2}(T)$ near T_c and $T_{c,90}$ is the critical temperature determined as described below fig. 2.15 in chap. 2.3.1.

Combining equation 2.1 and 2.2 yields in an equation for the coherence length

$$\xi = \sqrt{\frac{\Phi_0}{2\pi \cdot 0.69 \cdot m \cdot T_{c,90}}} \quad (2.3)$$

and finally with eq. 1.3, defining the flux quantum, the coherence length can be described as:

$$\xi = \sqrt{\frac{h}{4\pi \cdot e \cdot 0.69 \cdot m \cdot T_{c,90}}} \quad (2.4)$$

To determine the distance of pinning centers, a parameter has to be defined first. This parameter is called the matching field H_{Φ} [111]. The matching field describes a point, at which the density of the correlated pinning defects matches the density of the flux lines [2, p. 3]. Accordingly, the higher the matching field is, the higher the number of correlated columnar pinning defects becomes and vice versa. The matching field is the inflection point of the H_{irr} plot, which is due to the forming of vortex glass [111, 2, 112, 113, 114, 22]. Before reaching this point, flux lines are considered as liquid and can be depinned by thermodynamic fluctuations [115].

The matching field is defined as

$$H_{\Phi} = \frac{\Phi_0}{d^2}. \quad (2.5)$$

With the the equation for the flux quantum 1.3, the distance between pinning centers results in

$$d = \sqrt{\frac{h}{2e \cdot H_{\Phi}}}. \quad (2.6)$$

With the necessary data taken from the measurement data in the graphs fig. 2.15a and 2.15b, the following coherence lengths and distances between pinning centers result as shown in tab. 2.4a.

BHO content:	1.03 mol%	1.59 mol%	3.85 mol%
ξ (nm)	2.08	1.97	1.82
d (nm)	15.16	17.19	13.17

(a) Calculated coherence lengths ξ and distances d between the pinning centers for three different doping levels of BHO for Co-doped Ba122 samples deposited on CaF_2 .

BHO content:	3.85 mol%
\varnothing (nm)	3.50
d (nm)	12.19

(b) Measured diameter \varnothing of pinning centers and distance d between the pinning centers for a Co-doped Ba122 sample deposited on CaF_2 with 3.85 mol% of BHO.

Table 2.4: Calculated and measured coherence lengths ξ and distances d between the pinning centers for different doping levels of BHO for Co-doped Ba122 samples deposited on CaF_2 .

For comparison, the distances between the nanocolumns and their diameters in the TEM image of the sample with 3.85 mol% were measured within the TEM image and are displayed in tab. 2.4b.

The coherence length values decrease with increasing BHO content due to higher H_{c2} slopes (see tab. 2.4a and fig. 2.15b). An enhancement of H_{c2} with increasing doping

level has already been reported by Dou et al. [116] for MgB₂ films doped with SiC with minor effect on T_c . The distances decrease except for the sample with 1.59 mol%. The distance between pinning centers for the sample with 1.03 mol% is lower than for 1.59 mol% because the appearing columnar defects do not grow straight in c-direction. On average, this results in smaller distances than for the sample with 1.59 mol%, which exhibits more, but straight in c-direction growing columnar defects. 3.58 mol% shows the smallest distance due to formation of many big nanocolumns close to each other. This is confirmed by the small deviation of measured distance to calculated value.

The values for the distances are similar, especially if taken into account that distance and diameter are difficult to measure due to vanishing contrast at the edges of the nanocolumns. For the values in tab. 2.4b seven measurements were performed, of which the arithmetic average was taken. This average was converted into nanometers. Therefore, the error in calculating the average is multiplied by a factor during conversion. That is the reason why the measured distances exhibit a smaller error in the values in comparison to the measured diameters of the pinning centers. The error in the measurement of the distances reaches -converted to nm- a maximum of 1.44 nm. The error of diameters -converted into nm- reaches a maximum of 2.1 nm. Regarding the fact that the width of a flux line [117] is $2\xi = 3.64$ nm, the measurement of 3.5 nm is very close the calculation. Also regarding the error in the measurement of the distance of 1.44 nm, the maximum deviation of 0.98 nm from measured to calculated distance is within the error and therefore very similar.

The calculated distance values for the samples with 1.03 mol% and 1.59 mol% are uncertain because the inflection point can only be guessed and not be determined exactly. This is expected behavior since a proper inflection point can only be observed for the forming of vortex glass and therefore correlated nanocolumns as pinning centers [2]. For the sample with 3.85 mol% more data points would be useful, in order to determine a possibly more exact matching field.

However, the calculated diameter values match the reported coherence length values in Co-doped Ba122 of 2.5 nm [23]. The measured values are slightly higher, which explains the position of the peak of maximum pinning force at high magnetic fields. More than one flux vortex is able to enter a pinning center causing high pinning forces at high applied magnetic fields [118]. The calculated coherence lengths decrease with increasing BHO content due to enlargement of the pinning centers and compressing the Cooper pairs. The decrease of the nanocolumn distance with increasing BHO content happens for the same reason. More and larger pinning centers are located in the film. Consequently, the distance between them must decrease. For 1.59 mol% a small increase in distance can be observed in comparison to the value of the sample with 1.03 mol%. This is most probably because of the inhomogenous distribution of pinning centers in the sample with 1.03 mol%.

The sample with the highest content of 3.85 mol% BHO is the only sample which shows a proper inflection point in the irreversibility plot (fig. 2.15a). According to

Kiessling et al. [2], this means that this sample is the only one with a formation of vortex glass and a proper correlation between the columnar pinning defects. This finding is substantiated by the TEM investigations of those samples. The sample with the highest content of BHO shows equidistant BHO nanorods as pinning centers. The samples with other doping levels show a variation of nanoparticles and nanorods.

2.3.2 Experiments for optimization of homogenous distribution of BHO nanoparticles on LAO

The same BHO contents with optimized parameters were used to prepare samples on LAO substrates, to enable comparison to the samples shown before on CaF_2 . The laser energy was 20 mJ and the deposition temperature was set to 750 °C as optimized before (see chap. 2.2.3). All other parameters, such as positions, frequency and number of pulses were kept at same level to films on CaF_2 . The total amount of BHO was again controlled by the number of BHO interlayers of constant 12 pulses BHO per layer. For 1.03 mol% the targets were exchanged nine times and a cap layer of 1,800 pulses of Ba122 was added. The number of exchanges for 1.59 mol% amounted to 39 and the Ba122 cap layer consisted of 450 pulses. For 3.85 mol% of BHO, 143 exchanges and a cap layer of 125 pulses was deposited.

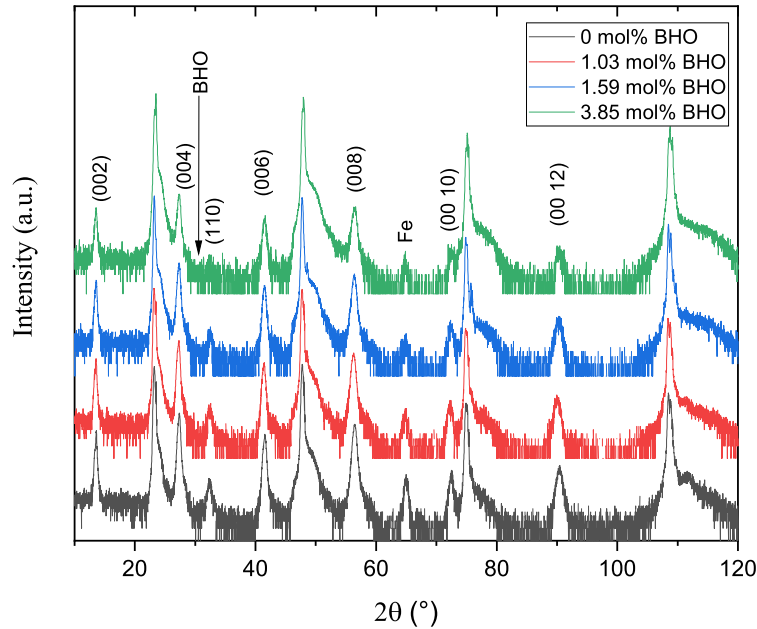


Figure 2.18: θ - 2θ scans of $\text{Ba}(\text{Fe}_{0.92}\text{Co}_{0.08})_2\text{As}_2$ films grown on LAO with different doping levels of BHO.

The $\theta - 2\theta$ scans in fig. 2.18 indicate c-axis texture of each film as well as for films grown on CaF_2 . The c-oriented growth of the $\text{Ba}(\text{Fe}_{0.92}\text{Co}_{0.08})_2\text{As}_2$ is preserved throughout the different doping levels. A slight hint of a BHO peak can be observed for 3.85 mol% BHO at an angle of around 30 °. The peaks do not tend to shift to higher angles at a doping level of 3.85 mol%. The c-axis parameter (1.30234 nm to 1.30274 nm) does not change significantly. The c-axis parameter of the pristine film is close to the c-axis parameter mentioned in the literature (see chap. 1.2.3), consequently Ba122 grows unstrained on LAO, even with implemented BHO. The implementation of BHO into the matrix does not cause any significant strain to the film.

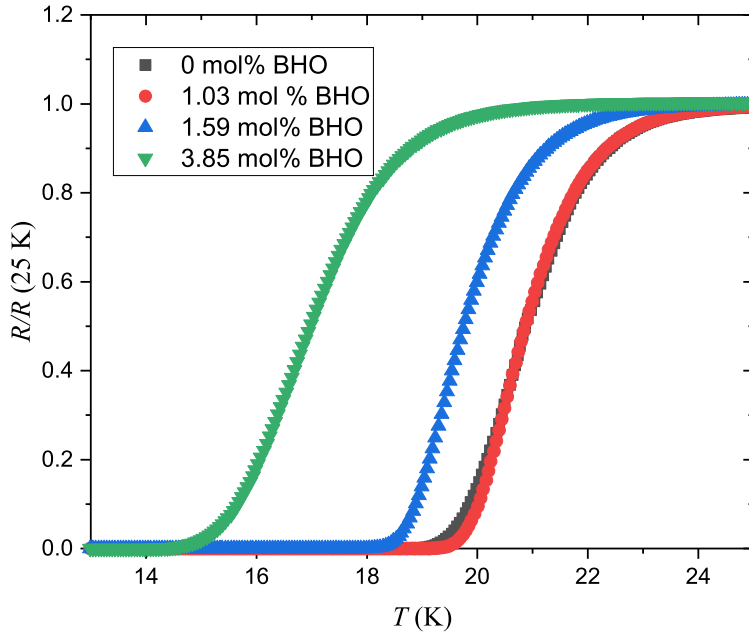
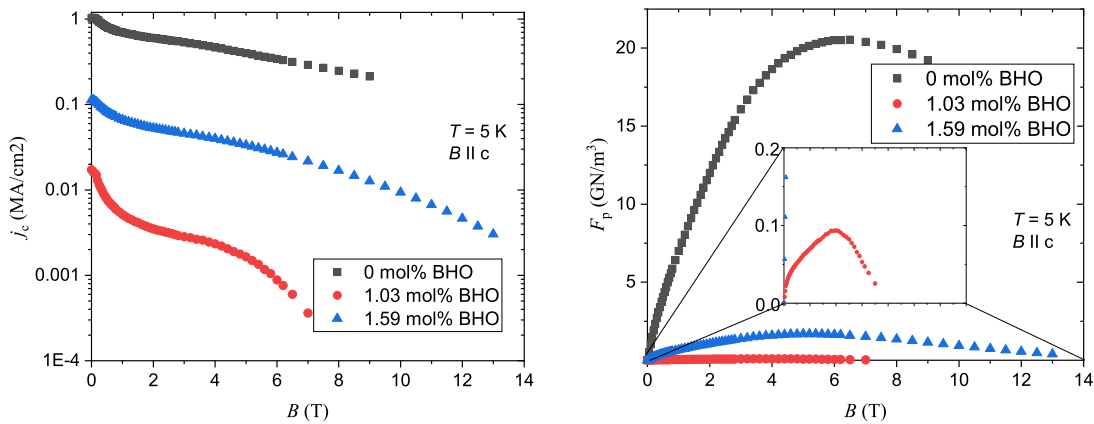


Figure 2.19: Temperature dependence of the resistance normalized to the value above T_c for three different levels of incorporated BHO in Co-doped Ba122 films grown on LAO.

The $T_{c,0}$ -values (see fig. 2.19) decrease with increasing doping level as expected, although the sample with 1.03 mol% has a slightly higher T_c -value than the pristine sample. The difference is only 0.2 K and within the usual experimental scatter.



(a) Critical current density j_c plotted as a function of the external magnetic field.

(b) The pinning force density F_p plotted as a function of the external magnetic field. The small inset shows the course of the sample with 1.03 mol% in particular.

Figure 2.20: a) Critical current density j_c and the b) pinning force density F_p plotted as a function of the external magnetic field for three different levels of incorporated BHO in Co-doped Ba122 films grown on LAO measured at 5 K and with an applied external magnetic field parallel to the c-axis in the film.

The j_c - and F_p -values of $\text{Ba}(\text{Fe}_{0.92}\text{Co}_{0.08})_2\text{As}_2$ on LAO do not show the expected behavior as seen before with samples grown on CaF_2 . Samples with implemented BHO present decreased values, compared to the pristine sample. Even the sample with an amount of 1.59 mol% has a lower j_c -value and lower F_p -values as the pristine sample. The values for the sample with the highest content of 3.85 mol% could not be evaluated, as the U - I -measurement showed a high degree of scattering. Therefore, j_c , respectively F_p could not be calculated. The pinning force densities show a slight shift from pristine sample to the sample with the highest content of BHO of 1.59 mol% in the maximum F_p to higher applied magnetic fields.

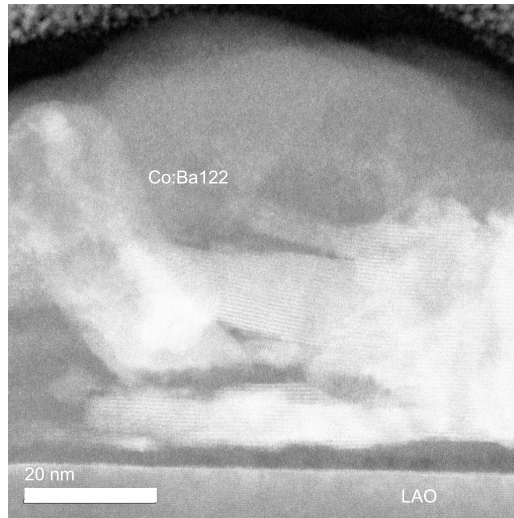
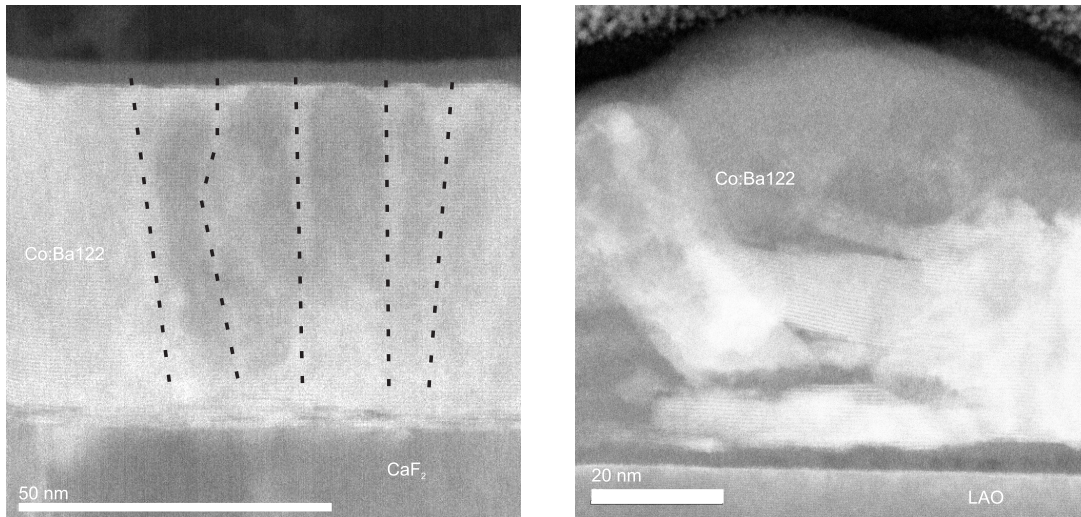


Figure 2.21: HR-STEM image of a Co-doped Ba122 sample with 3.85 mol% of BHO deposited on LAO. Several different orientations can be observed.

These results are reinforced by the TEM image taken of a sample prepared on LAO with 3.85 mol% of BHO (see fig. 2.21). Several different orientations and phases can be observed. This is most likely due to the occurrence of crystal twins on the substrate surface, forcing the deposited material to grow in different orientations.

2.3.3 Conclusion

The incorporation of the perovskites BHO and BZO proved the necessity of a certain film thickness, in order to provide enough volume for the equal distribution of the artificial pinning centers. The findings additionally revealed that the most suitable substrate for the application of the quasi-multilayer technique is CaF_2 . Samples grown on LAO showed that the pinning force density as well as the critical current density are not enhanced by increasing the content of the perovskite pinning material. The measurements showed large deviations. It is very likely that the crystal twins on the surface of the substrate create crystal displacements in the films growing on top, therefore creating pinning centers. By increasing the content of artificial pinning material, only the lattice presents increasing disturbance, which yields in the decrease of the superconducting properties. The $T_{c,0}$ -values are reduced linear to increasing lattice disturbance by the perovskites. The critical current density and the pinning force density values are already linked to the occurrence of twins and their effect on the film growth before the deposition.



(a) HR-STEM image of a Co-doped Ba122 sample with 3.85 mol% of BHO deposited on CaF_2 . Black dashed lines indicate BHO nanocolumns. (b) HR-STEM image of a Co-doped Ba122 sample with 3.85 mol% of BHO deposited on LAO. Several different orientations can be observed.

Figure 2.22: HR-STEM images of a Co-doped Ba122 sample with 3.85 mol% of BHO deposited on a) CaF_2 and b) LAO.

This is shown by TEM images of samples grown with the same pattern. Both samples have 3.85 mol% of BHO in the Co-doped Ba122 matrix. Fig. 2.22a shows a sample grown on CaF_2 , fig. 2.22b shows a sample deposited on LAO. The sample on CaF_2 exhibits BHO nanocolumns in the matrix (indicated by dashed lines in fig. 2.22a). The rest of the film consists of epitaxially grown Co-doped Ba122, displaying a layer-type structure. Conversely, several different orientations and phases can be observed in the image of the sample prepared on LAO. This happens most likely due to the occurrence

of crystal twins on the substrate surface, which force the deposited material to grow in different orientations [71]. Thus, LAO is not a suitable candidate for investigating implementation of artificial pinning centers since an amount of pinning centers already appears in the Ba122 compound during growth.

As the results on CaF_2 provided better results, further experiments were performed on this substrate with the implementation of BHO, to explore an entirely new field of research. Although, it was not possible to grow samples with the highest achievable T_c -values [19], due to strain caused by BaF_2 formation at higher laser energies. This formation could have disturbed the pinning effect by the BHO. Though, the achieved critical temperatures were high enough for experiments with implementation of artificial pinning centers.

The pristine films must exhibit highest possible crystalline quality and critical temperature, because the implementation of artificial pinning centers decreases the critical temperature with increasing doping level. If the critical temperature in the pristine sample is too low, the implementation of artificial pinning centers will destroy the superconductivity in the compound.

The X-ray analysis showed that the Ba122 lattice is preserved for all pinning material contents. The BHO peak could barely be observed at the highest amount of incorporated BHO of 3.85 mol%. The peak could not be observed at lower BHO levels most likely due to unoriented growth of the particles. The T_c decrease showed a linear dependence to the BHO level. The critical current density j_c increases by a factor of 3.62, the pinning force density F_p by a factor of 11.03. These results correspond to the findings of Lee et al. [23], who show similar enhancements of the values. With pinning force density values of 50.6 GN/m^3 at 11 T, the highest doped sample is in the range of reported samples, such as multilayer Co-Ba122/BaO-doped Co-Ba122 with 84 GN/m^3 at 22.5 T and 4.2 K [74] and BZO-P-Ba122 thin films with 59 GN/m^3 at 3 - 9 T and 5 K [20]. The technical relevant j_c values for NbTi cables and coils used by CERN are reported to exhibit values between $0.15 - 0.23 \text{ MA/cm}^2$ at operating temperatures of 4.2 K and magnetic fields of 4 respectively 6 T [17, 18]. The Chinese Academy of Science in Beijing produced 100 m long Ba122 tapes and reported values above the practical application level of 0.15 MA/cm^2 at 4.2 K and 10 T [15]. The implementation of artificial perovskite pinning centers could further improve these reported values since the measured values in this work already exceed the reported values. This applies even for the pristine Co-doped Ba122, which has not reached its highest reported j_c values of around 4 MA/cm^2 [12, 13] in this work's measurements, due to experimental setup limitations such as laser frequency and energy.

To determine the acting pinning mechanisms, the pinning force density plots can be evaluated based on the work of Dew-Hughes [37]. He calculated different courses of pinning force density plots for various types of pinning centers. For the pristine Co-doped Ba122 on CaF_2 sample the dominant pinning mechanism should be the normal core surface pinning [37, p. 298, 300] (see fig. 2.23 and 2.12b).

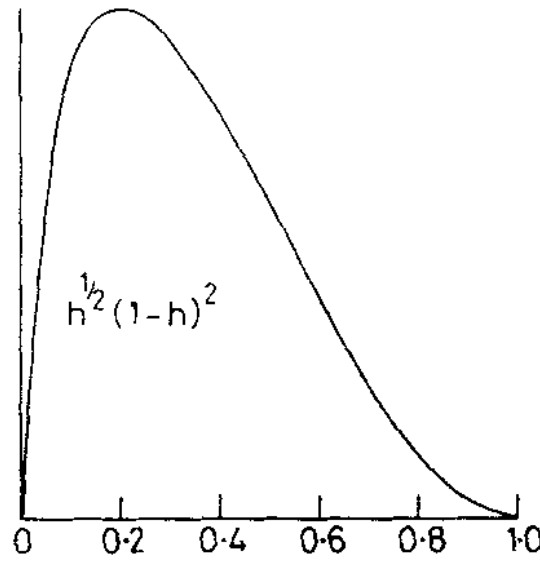


Figure 2.23: Theoretical pinning force density plot of normal core surface pinning by Dew-Hughes [37, p. 300].

The slope of the curve is steep until it a flat peak for low magnetic fields and decreases rather slowly at higher magnetic fields. This effect can be explained by grain boundaries, stacking faults and similar, as shown in fig. 2.16a.

With increasing BHO level, the pinning force density peak shifts to higher magnetic fields and slowly decreases beyond the peak. This fits to the core volume pinning mechanism mentioned by Dew-Hughes. He explains that for lower magnetic fields, the $\Delta\kappa$ core volume pinning (see fig. 2.24 and fig. 2.12b) is dominant, while beyond the maximum, the decrease can be described by normal core volume pinning [37, p. 298, 300, 301]. This is especially suitable for materials with a high κ and mixed microstructure.

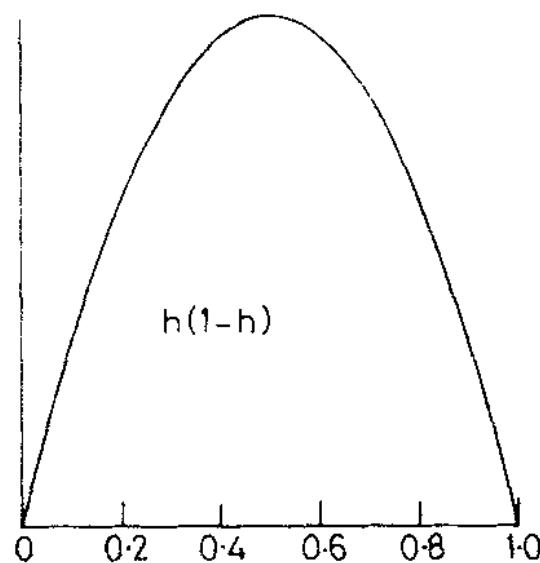


Figure 2.24: Theoretical pinning force density plot of $\Delta\kappa$ core volume pinning by Dew-Hughes [37, p. 300].

In comparison, samples grown on LAO present different mechanisms. The pristine sample shows normal core surface pinning [37, p. 298, 300] (fig. 2.23 and fig. 2.20b) due to twin boundaries at the surface of the LAO [71], causing stacking faults, various growth orientations and other defects. The forming of defects due to surface twins is substantiated by the TEM image in fig. 2.22b, which displays a sample with the highest BHO amount of 3.95 mol%. However, the high quantity of defects can not be explained solely by the implementation of BHO, as samples grown on CaF₂ with the same BHO amount do not exhibit such defect density.

With increasing BHO content, an overlap of the three before mentioned pinning mechanisms can be observed - as demonstrated by the sample with a BHO content of 1.03 mol%. For low magnetic fields, a peak appears after a steep slope. This area exhibits the normal core surface pinning mechanism (fig. 2.23 and fig. 2.20b) due to twin or grain boundaries and similar defects. Beyond the peak, the pinning force density however increases until it reaches another maximum at around 4 T. In this area the core volume pinning mechanism caused by the implementation of BHO takes over and decreases the pinning force density rapidly [37, p. 298, 300]. The overlap and therefore the existence of the normal core surface pinning mechanism for all samples shows that the surface twins of the LAO are the reason for defects shown in fig. 2.22b in both pristine and doped samples.

To ensure the right choice of pinning mechanisms, regardless of its reasonability or provability e.g. by TEM images, the necessity remains to measure the pinning force density of those samples at higher magnetic fields, to unveil the whole course of the plot.

The comparison to the samples investigated by Lee poses a problem since the targets used by Lee were premixed and not prepared by using the quasi-multilayer technique. Moreover, they were not investigated for their actual amount of BZO. Furthermore, Lee et al. calculated the j_c - and therefore the F_p -values based on the Bean model [119]. However, this would lead to lower values because of the lower field criterion. In this work, the values were measured by first etching a bridge into the sample and performing subsequent U - I -measurements. The samples in the work of Lee [23] have film thicknesses of 400 nm, whereas the samples in this work show a maximum thickness of 110 nm. Consequently, Lee bases certain values, such as bridge size, on assumptions, whereas in this work, certain errors such as deviations in the thickness and width of the bridge, lattice quality deviations in the bridge and possible suboptimal distribution of nanoparticles are taken into consideration. To enable further comparison of other results to the findings presented in this work, much more research needs to be done especially by using the quasi-multilayer technique. The research done by Lee et al. [23] and Miura et al. [24] is the only research yet performed on implementation of perovskites as pinning materials in FBS. Hence, Lee's findings reveal that the good results of the first quasi-multilayered Ba122 films are not the limit, but there is plenty of room for improvement.

2.4 Ba122 with incorporated InAs

To investigate and compare a possibly different pinning mechanism or an alternative nanoparticle incorporation with other phases in Co-doped Ba122, the decision was made to experiment with another pinning material, which has never been used before. This experiment is based on the concept and the idea, that arsenides can be incorporated easily in the Ba122 matrix, as they do not contain any oxygen, which could be incorporated in the Ba122 matrix, replacing As atoms and destroying superconducting properties. It has also been reported that deficiency or vacancies of As in Co-doped Ba122 films increase the critical current density [120] and may act as pinning centers [25]. However, the high vapor pressure of InAs, and therefore a possible loss of pinning material during deposition, is an issue of high temperature deposition (see chap. 1.3.1.4).

The first approach was to reproduce the samples grown on CaF_2 with InAs instead of BHO. Several deposition patterns were tested and the best results were obtained for a deposition pattern similar to the samples with 1.59 mol% BHO (see chap. 2.3.1). 39 exchanges were performed and the Ba122 cap layer consisted of 450 pulses. Thus, only the number of pulses for the InAs were changed to identify the best composition. The findings conclude, that only a number of pulses on InAs, ranging between 10 and 30 pulses per exchange, or 390 to 1170 in total, showed reasonable and reproducible results.

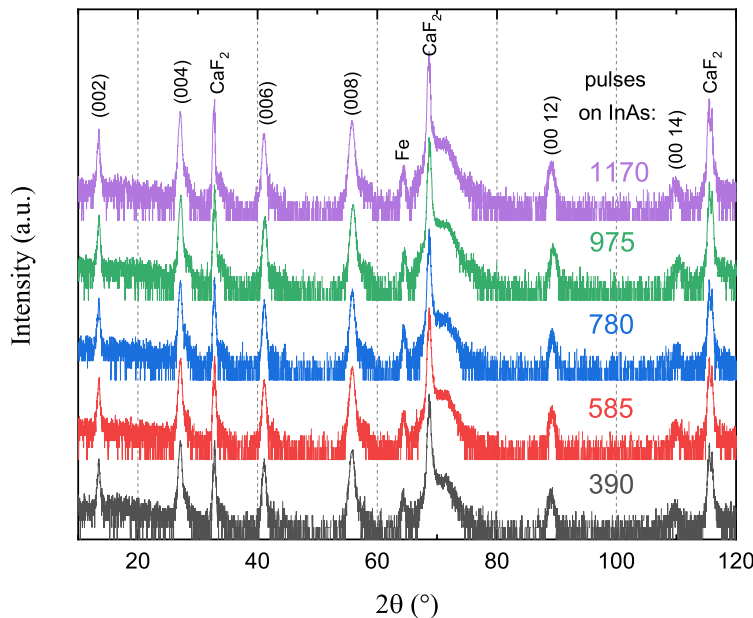


Figure 2.25: θ - 2θ scans of $\text{Ba}(\text{Fe}_{0.92}\text{Co}_{0.08})_2\text{As}_2$ films grown on CaF_2 with different doping levels of InAs.

The $\theta - 2\theta$ scans in fig. 2.25 indicate c-axis texture of each sample. There was no significant change of the c-axis parameter (1.31972 nm to 1.31729 nm) between

the pristine sample and the sample prepared with 1170 pulses InAs. These samples showed the expected behavior as already seen before with incorporation of BHO (see fig. 2.10). The samples were investigated by ICP measurements to determine the InAs content in the films. The sample with 390 pulses of InAs exhibited an amount of 0.8 mol%, 585 pulses exhibited 0.42 mol%, 780 pulses had 2.21 mol%, 975 pulses 0.97 mol% and 1170 pulses 1.05 mol%. Although indium could be detected by ICP measurements and a trend in content of indium with increasing number of pulses became apparent, the scatter was quite large and could not be described by a linear fit. Due to the small amounts, EDX and EELS measurements could not detect any indium.

As Engelmann et al. [120] reported, an As deficiency could be responsible for an increase of the critical temperature. In addition, Kurth et al. [25] note that vacancies of arsenic can act as pinning centers. Based on this knowledge and the fact that InAs could also add arsenic to the Ba122 layer, the influence of the additional arsenic from the InAs doping should not be neglected.

These findings supported the decision to not use the indium level as scale, but rather continue with pulses on InAs. The scatter of the data of the plot T_c over the pulse number (see fig. 2.26) correlated strongly with the scatter of the c-axis parameter. Therefore, the c-axis parameter and hence strain in such samples was considered an important secondary effect determining T_c .

This means, the scatter in the content of InAs matched the scatter in T_c values, which was due to the fact that arsenic is released from the InAs and incorporated into the Ba122 matrix. This increased the crystalline quality, which is substantiated by TEM measurements not showing any kind of defects. The stability of the InAs seemed to be fragile, causing it to split up. Another possible explanation for the deviation of the InAs content to the used number of pulses is the formation of droplets on the surface or large agglomerations of InAs which are not part of the pinning mechanism but are displayed in the ICP measurements.

The samples with 390, 585, 780, 975 and 1170 pulses of InAs are selected for further investigation since no difference between the samples could be observed in the XRD-diffractograms, not making any sample a more likely candidate.

The $R(T)$ measurements show an expected trend with decreasing T_c -values for increasing amount of pulses on the InAs target (therefore see fig. 2.26, where the $T_{c,0}$ values of several samples are plotted against the number of pulses on the InAs target). A small scatter is evident, but still in the range of experimental deviation.

There is no difference between the series in the growth parameters etc of samples. The samples were grown at different points of time to investigate if interruptions by different experiments and depositions have an influence on the quality of the films. Consequently, no influence of other experiments or degradation of the target could be observed.

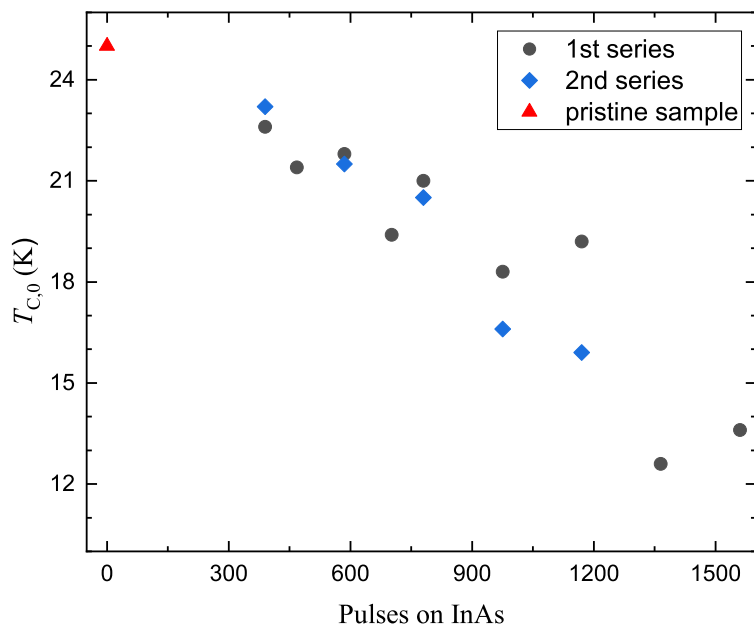


Figure 2.26: Critical temperature $T_{c,0}$ of several Co-doped Ba122 samples grown on CaF_2 with incorporated InAs as a function of the number of laser pulses on the InAs target of each iteration.

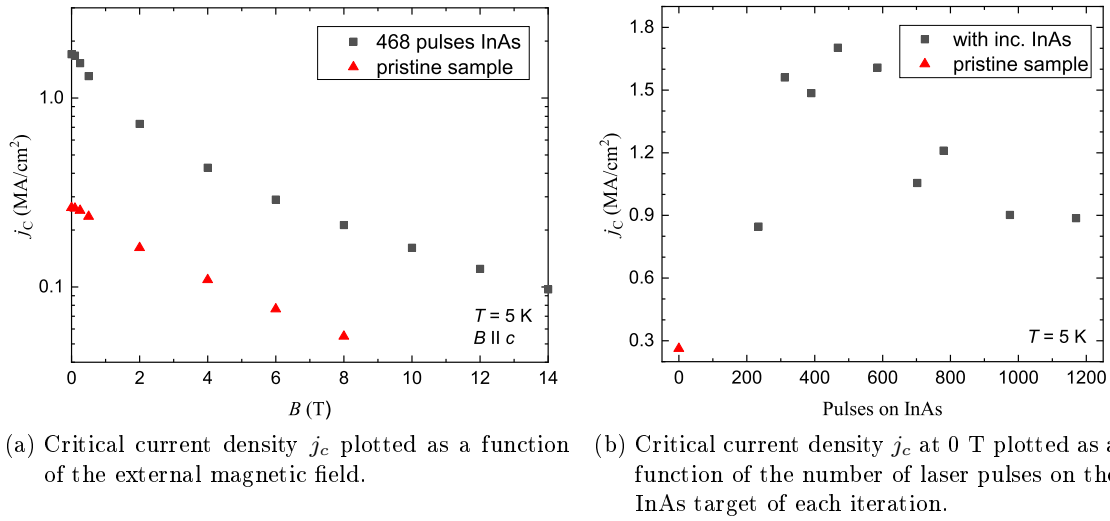


Figure 2.27: Critical current density j_c plotted as a function of the external magnetic field (a)) and plotted as a function of the number of laser pulses on the InAs target of each iteration at 0 T (b)) of several Co-doped Ba122 samples grown on CaF₂ with incorporated InAs (2nd series) measured at 5 K and with an applied external magnetic field parallel to the c-axis of the film.

The graph in fig. 2.27a of the critical current density values at 5 K, for an applied magnetic field parallel to the c-axis of the film, presents a strong increase by a factor of 6.48 for an amount of 468 pulses in comparison to the pristine film. This comparison was emphasized, because the sample with 468 pulses indicated the highest j_c -values. These values were measured for samples with different contents of InAs. The j_c -values without applied magnetic field at 5 K are displayed in fig. 2.27b. It can be observed that a so called dome forms around a maximum peak at 468 pulses on InAs. Samples containing lower or higher amounts of InAs than the sample with 468 pulses, show lower critical current densities. This leads to the assumption that for lower InAs contents, the pinning is not yet optimal, while for higher contents the disorder caused by implementing more InAs increases disorder in the lattice, weakening the pinning potential and thereby decreasing the superconducting properties.

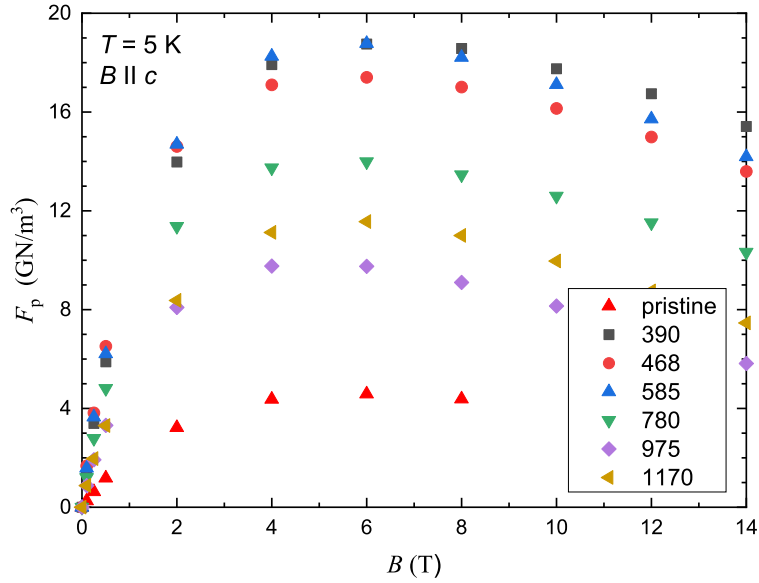


Figure 2.28: The pinning force density F_p plotted as a function of the external magnetic field for different levels of incorporated InAs (given in number of pulses) in Co-doped Ba122 films, grown on CaF_2 , measured at 5 K and with an applied external magnetic field parallel to the c-axis in the film.

The pinning force densities correspond with the trend given by the j_c dome in fig. 2.27b. However, the samples with 390 and 585 pulses, which show slightly lower j_c -values than the sample with 468 pulses, exhibit slightly higher pinning force densities.

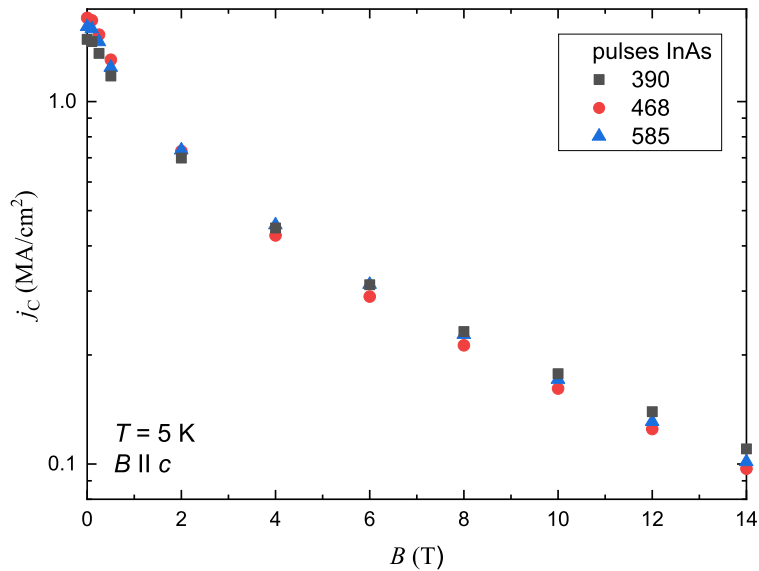
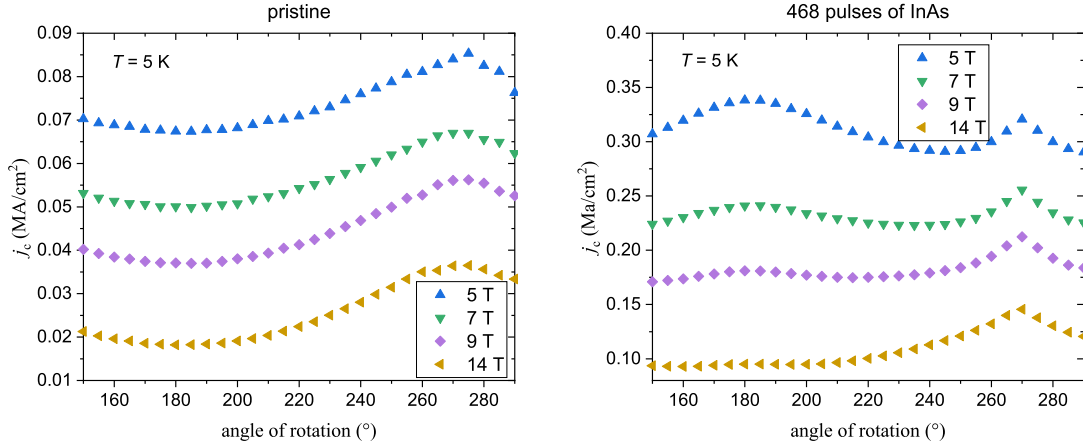


Figure 2.29: Critical current density j_c plotted as a function of the external magnetic field of three Co-doped Ba122 samples, grown on CaF_2 with incorporated InAs, measured at 5 K and with an applied external magnetic field parallel to the c-axis in the film.

This is due to fact that the 468 pulses sample shows higher j_c -values for low magnetic

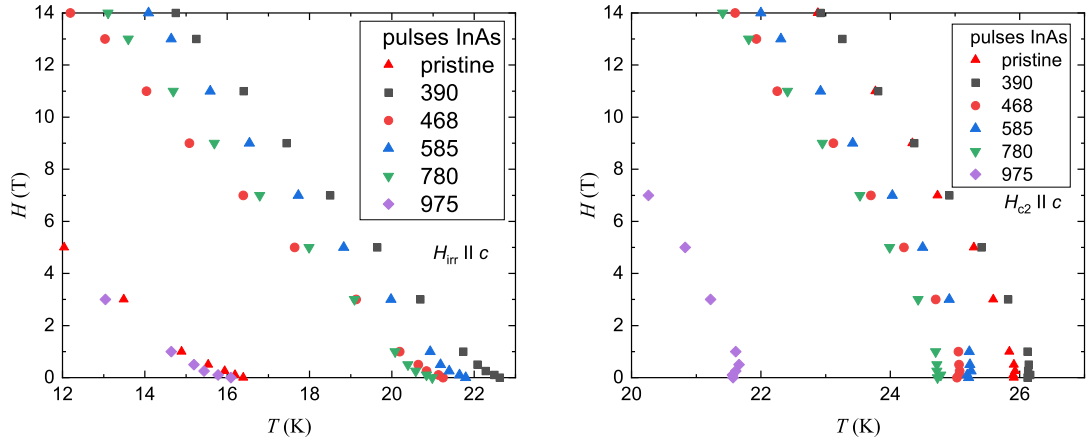
fields up to 2 T. With increasing applied magnetic field, the samples with 390, respectively 585 pulses show slightly higher j_c curves (see fig. 2.29). Since F_p is the product of $j_c \cdot H$ (see eq. 1.4, with $B = \mu \cdot H$), the deviation of the j_c -values is multiplied by the factor of the applied magnetic field and therefore more visible in the graph of the pinning force densities. No peak shift can be observed in the pinning force density plot (see fig. 2.28) The maximum for all samples is at 6 T except for the sample with 975 pulses. For this sample the maximum is slightly lower at around 5 T.



(a) The critical current density j_c is plotted as a function of the rotation angle in an applied external magnetic field for a pristine sample. (b) The critical current density j_c is plotted as a function of the rotation angle in an applied external magnetic field for a sample with 468 pulses of InAs.

Figure 2.30: Anisotropy plots of two different levels of incorporated InAs in Co-doped Ba122 films grown on CaF₂. The critical current density j_c is plotted as a function of the rotation angle in an applied external magnetic field.

The j_c -values were also measured for different applied magnetic fields and for angles in the range of 150 to 290 ° in the magnetic field for all samples. For the pristine sample a strong peak at 270 ° can be observed. This corresponds to the a/b-plane in the film. The sample with the highest j_c -value at 0 T (with 468 pulses InAs) shows a small peak at 180 °. This corresponds to the c-axis of the film. The peak corresponding to the a/b-plane also displays more evident than the peak of the pristine sample. The c-axis peak is almost completely suppressed for high magnetic fields. This peak appears strongest for applied magnetic fields of 5 T - the maximum pinning force. Theoretical considerations [121], simulations [122] and experiments [123] lead to the assumption that such strong and broad c-axis peaks can be associated with isotropic defects slightly larger than the coherence length. Whether those regions are InAs- or In-rich regions, with different critical temperatures and superconducting properties, could not be determined. There is no visible trend with increasing amounts of InAs in the samples, therefore only a comparison from pristine to the sample with the maximum j_c at 0 T is provided in fig. 2.30.



(a) Irreversibility field H_{irr} as a function of the temperature. (b) Critical magnetic field H_{c2} as a function of the temperature.

Figure 2.31: a) Irreversibility field H_{irr} and b) critical magnetic field H_{c2} as a function of the temperature for several levels of incorporated InAs in Co-doped Ba122 films grown on CaF_2 .

Furthermore, the irreversibility field H_{irr} and the critical magnetic field H_{c2} were determined (see fig. 2.31). For H_{irr} the irreversibility line for the sample with 390 pulses is higher than for the other samples, followed by the sample with 585 pulses and the sample with 780 pulses. For low magnetic fields, the sample with the highest j_c with 468 pulses of InAs has a higher irreversibility field than the sample with 780 pulses. It seems that the higher amount of InAs strongly reduces T_c due to implementation of more In. The As content is obviously also higher, thus the crystalline quality may be better for the sample with 780 pulses, allowing the superconductivity to be maintained further in the remaining superconducting regimes. The pristine sample shows almost the lowest irreversibility field except for the sample with 975 pulses, which presents the lowest irreversibility field. Furthermore, it can be observed that the H_{c2} -values tend to decrease with higher amount of InAs. Only the sample with 468 pulses of InAs, presenting values ranging between sample values for 585 pulses and 790 pulses, deviates from this trend. The H_{c2} -values of the sample with 390 pulses exhibits a similar course to the values of the pristine sample, although for lower magnetic fields higher temperature values can be observed.

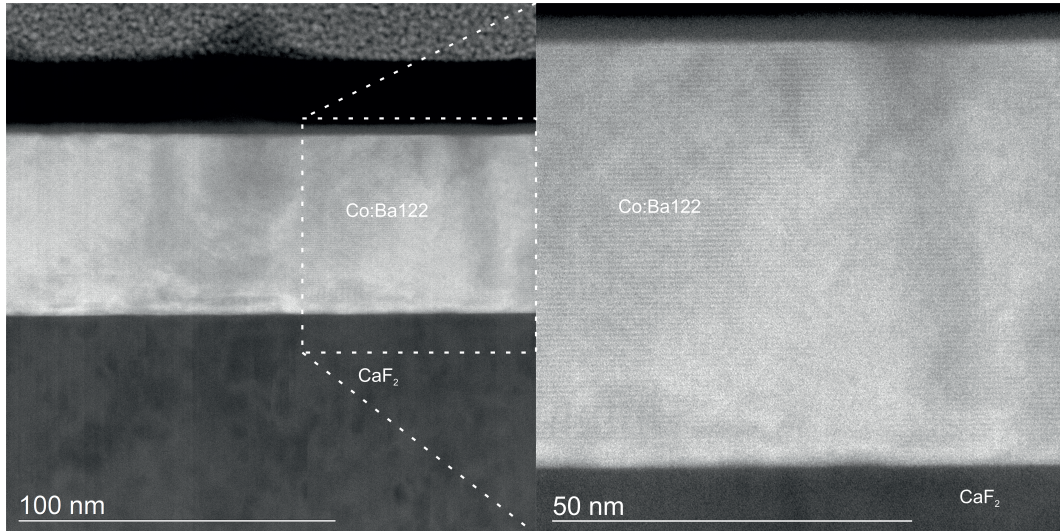


Figure 2.32: HR-STEM image of a Co-doped Ba122 sample with 1170 pulses of InAs deposited on CaF₂. The cloudy contrast variations are due to the electron bombardment during the TEM investigation.

TEM images of InAs doped samples do not show any hint of artificial pinning centers (e.g. fig. 2.32).

It is obvious, that c-axis pinning is enhanced for the optimal InAs level. However, no dependence on the number of pulses or content of InAs becomes visible in the anisotropy plots. Because the maximum pinning force density happens at magnetic fields of 6 T, smaller pinning centers, which are volatile under electron bombardment in the TEM, might hypothetically be the reason for pinning in these samples. This is supported by the curve of the anisotropy graph for the optimal doped sample. At high magnetic fields the c-axis peak almost vanishes. For low magnetic fields (e.g. 6 T) there are enough pinning centers for the number of flux vortices, but for higher fields the pinning centers interact with more than one vortex at a time [118]. Consequently, these vortices are not pinned and able to move through the superconducting film, causing a decrease of the critical current density. The pinning mechanism was determined, based on the work of Dew-Hughes, to normal core point pinning [37, p. 298, 300] (see fig. 2.33 and fig. 2.28).

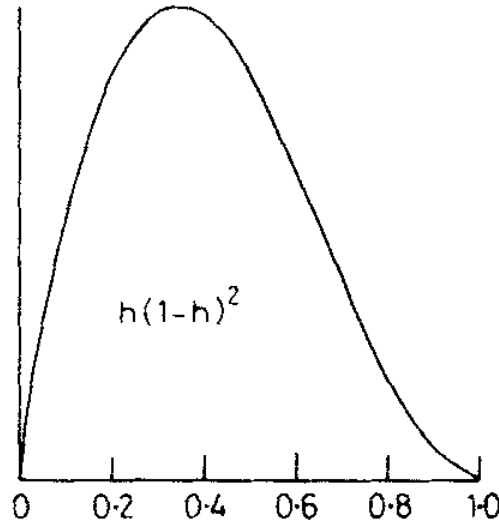


Figure 2.33: Theoretical pinning force density plot of normal core point pinning by Dew-Hughes [37, p. 300].

Reasons for that pinning mechanism are point defects, which can only interact with solely one flux line at a time [37, p. 295], confirming the hypothesis mentioned before. Hence, an increase of InAs content in the film results in an increasing number of point defects interacting with one flux line, until an optimum of critical current density is reached. Beyond this optimum, the increasing content only causes disorder in the lattice and the critical current density decreases again.

As for the samples with implemented BHO, the coherence lengths were calculated (see tab. 2.5).

pulses on InAs	390	468	585	780	975
ξ (nm)	2.22	2.30	2.41	2.26	2.52

Table 2.5: Calculated coherence length ξ for a Co-doped Ba122 sample deposited on CaF_2 with various amount of pulses of InAs.

The coherence lengths, compared to the nominal value of 2.5 nm [23], are in the range of scattering. The increase of the coherence length with increasing number of pulses is accompanied by a reduction of the critical temperature $T_{c,90}$, because of a higher amount of impurity phases. The only exception is the sample with 780 pulses. It could be that the arsenic is incorporated into the Ba122 matrix placed in As vacancies, thereby locally increasing the superconductivity. In this case this effect is highest for the sample with 780 pulses.

The distances between pinning centers could not be investigated, since no inflection point could be determined from the H_{irr} data. The inflection point only shows, if correlated pinning defects such as nanocolumns are present, resulting in the formation of a vortex glass. This leads to the conclusion that point defects are present in the films and therefore the vortex liquid phase is predominant.

2.4.1 Conclusion

The final experiment of this work included InAs as a pinning material, which has never been used before, neither in FBS nor in YBCO compounds. InAs is not an oxide and supplies the superconducting thin film with As, to avoid deficiencies and thereby theoretically ensure a predominantly intrinsic pinning center-free film. It was shown that the implementation of InAs decreases the critical temperature with increasing doping level, similar to the implementation of other materials such as BHO and BZO. The biggest limitation for InAs is its high vapor pressure. It has been reported that it grows at temperatures up to a maximum of 570 °C [82] which is significantly lower than the growth temperature of Ba122. The optimal deposition temperatures for Co-doped Ba122 on CaF₂ is 700 °C. It was not possible to grow Ba122 at lower temperatures, to approach the optimal growth temperature for InAs. However, with the deployed deposition pattern, it was possible to reproducibly prepare samples with expected crystalline quality and superconducting properties. The measured InAs contents do not correspond to the number of pulses most probably due to random re-evaporation of InAs during the deposition or formation of InAs-rich surface precipitates, not taking part in pinning mechanism, but detected by ICP measurements. This is the reason for using the number of pulses on InAs of each sample to create a better view on the nominal doping level.

The critical current density values were enhanced up to a factor of 6.48. With increasing number of pulses on the InAs target, a so called j_c dome formed in the graph of j_c as a function of pulses. The optimal number of pulses for highest critical current density resulted in 468 pulses. Higher amounts of pulses brought more disorder into the Ba122 matrix, causing a decrease of superconducting properties such as j_c most probably by decrease of T_c . For lower amounts of pulses, the pinning is most likely not yet optimal. Perhaps, not enough or not large enough pinning centers are present to contain the appearing flux lines. The pinning force densities correspond to this assumption, however for 390 pulses and for 585 pulses, the maximum pinning force densities are higher than for the sample prepared with 468 pulses. This is due to fact that the 468 pulses sample shows higher j_c -values for low magnetic fields up to 2 T. With increasing applied magnetic field, the samples with 390 respectively 585 pulses show slightly higher j_c curves (see fig. 2.29). Since F_p is the product of $j_c \cdot B$ (see eq. 1.4), the deviation of the j_c -values is multiplied by the factor of the applied magnetic field and therefore more visible in the graph of the pinning force densities. It is noticeable that no peak shift can be observed in the pinning force density plot (see fig. 2.28). The maximum for all samples is at 6 T. Compared to the samples with incorporated BHO, the maximum pinning force densities are located at significantly lower magnetic fields.

TEM images of the InAs doped samples do not exhibit any hint of artificial pinning centers (e.g. fig. 2.32). Smaller pinning centers, which are volatile under electron bombardment in the TEM, might hypothetically be the reason for pinning in these samples. This hypothesis is supported by the anisotropy plots for which the c-axis peak

vanishes at higher magnetic fields. Based on the work of Dew-Hughes, the pinning mechanism was determined to normal core point pinning [37, p. 298, 300]. To ensure the choice of pinning mechanism, it is necessary to measure the pinning force density of those samples at higher magnetic fields, to unveil the whole course of the plot.

The increase of the coherence length with increasing number of pulses is accompanied by a reduction of the critical temperature $T_{c,90}$, because of a higher amount of impurity phases.

The inflection point could not be determined from the H_{irr} data. The inflection point only shows, if correlated pinning defects such as nanocolumns are present, resulting in the formation of a vortex glass. Therefore, this fact supports the hypothesis that point defects are present in the films and the vortex liquid phase is predominant.

Since the pristine samples already showed critical current density values above the critical application level, the approach of incorporation of InAs pinning centers could further enhance the relevant properties, such as critical current densities, of future cables and wires. To enable this progress, the pinning mechanism and implementation of InAs in a Ba122 matrix has to be further investigated.

3 Summary

In this work, Ba122 compounds were investigated regarding the potential of introducing the quasi-multilayer technique for pulsed laser deposition to enable the growth of these compounds and implementation of other materials such as perovskites as pinning centers.

The first experiments aimed at maintaining reproducibility throughout the subsequent experiments. This ensured constant crystalline quality of Ba122 superconducting films on a suitable substrate for the existing experimental setup. Epitaxial Growth of superconducting Co and P-doped Ba122 films on MgO was achieved. However, a very narrow parameter window and alternating quality of the substrates limited the reproducibility of these samples.

The TEM and SEM measurements of the films on MgO (see fig. 2.2) often revealed foreign phases and orientations, which is due to the foreign atoms or elements present at the surface of the substrate. Similar occurrences had been reported by Lee et al. [62], who mention BaFeO₃ phases in BaTiO₃-templated Co-doped Ba122 films. The film thicknesses and their superconducting properties (e.g. T_c) were in the same range as reported in the literature [25, 107, 97]. The formation of a thin Fe layer could be observed, yet this formation was not linked to the visible Fe peak in the corresponding X-ray diffractograms. Large Fe phases in the films were identified as the cause for the formation of an Fe peak, as proven by TEM measurements and Nelson-Riley calculations. Primarily due to limited deposition temperatures caused by the experimental setup, it was decided to continue further experiments with Co-doped Ba122, since its deposition temperature is lower and can be handled easier with the heater.

To find suitable substrates with satisfying properties, which enable growth of reproducibly good quality iron-based superconducting films, LAO and CaF₂ were tested. Investigations showed the expected growth mode as well as the critical temperatures in the range of the samples reported in the literature. In chemical stoichiometry measurements of the LAO and CaF₂ substrates appear less foreign atoms or elements compared to MgO. Consequently, the reproducibility of good quality film growth could be maintained.

The implementation of the perovskites BHO and BZO revealed a certain critical film thickness of the samples necessary to provide enough volume for equal artificial pinning center distribution. The best suitable substrate for the application of the quasi-multilayer technique turned out to be CaF₂. Films grown on LAO showed that the

pinning force density as well as the critical current density were not enhanced by increased content of perovskite pinning material. The measurements of samples grown on LAO showed large deviations from the expected behavior. It can be assumed that crystal twins on the surface of the substrate created crystal displacements in the films growing on top, thereby creating pinning centers. An increase of the content of artificial pinning material only led to more disturbances of the lattice, yielding in decrease of the superconducting properties. As expected, $T_{c,0}$ -values were linearly reduced with increasing lattice disturbance by the perovskites. However, critical current densities and pinning force densities were linked to the occurrence of twins and their pinning center-causing effect.

TEM images supported this hypothesis. Films grown on CaF_2 exhibited BHO nanocolumns in the matrix, while the rest of the film was epitaxially grown Co-doped Ba122. Films on LAO showed several different orientations and phases, leading to the assumption that crystal twins on the substrate surface forced the deposited material to grow in different orientations.

Further experiments were performed on CaF_2 - due to better reproducibility and better crystal growth - with the implementation of BHO, to explore an entirely new field of research. However, it was not possible to grow samples with the highest achievable $T_{c,0}$ -values [19] in this setup, due to strain caused by BaF_2 forming at higher laser energies, which could have disturbed the pinning effect by the BHO. Resulting critical temperatures were high enough though, to maintain suitable values even when decreased by incorporation of artificial pinning centers.

X-ray analysis showed that the Ba122 lattice was preserved throughout all samples with different pinning material contents. The BHO peak barely appeared at the highest amount of incorporated BHO of 3.85 mol%. The peak could not be observed at lower BHO levels, most likely due to unoriented growth of the particles. T_c decrease followed linear dependence to the implemented perovskite level. The critical current density j_c increased by a factor of 3.62 and the pinning force density F_p by a factor of 11.03. This corresponds to the findings of Lee et al. [23] with similar enhancements. Pinning force density values of 50.6 GN/m^3 at 11 T for the highest doped sample with visible nanocolumns were in the range of reported samples such as multilayer Co-Ba122/BaO-doped Co-Ba122 with 84 GN/m^3 at 22.5 T and 4.2 K [74] and BZO-P-Ba122 thin films with 59 GN/m^3 at 3 - 9 T and 5 K [20]. This behaviour is due to increasing size and density of the pinning centers. At higher magnetic fields larger pinning centers allow more flux vortices to enter into each one [118]. The pinning mechanism was determined based on the work of Dew-Hughes [37]. For pristine Co-doped Ba122 samples grown on CaF_2 the normal core surface pinning center [37, p. 298, 300] was the dominant pinning mechanism which can be explained by grain boundaries, step defects and similar, as shown in fig. 2.16a. With increasing amount of BHO, a shift in the maximum peaks of the pinning force densities to higher applied magnetic fields and a slow decrease beyond the peak appeared. This shift could be explained by core volume pinning mechanism,

which is especially suitable for materials with a high κ and mixed microstructure. For lower magnetic fields, the $\Delta\kappa$ core volume pinning was dominant. Beyond the maximum, the decrease could be described by normal core volume pinning [37, p. 298, 300, 301].

Compared to this, Co-doped Ba122 films grown on LAO showed different pinning mechanisms. The pristine sample indicated normal core surface pinning [37, p. 298, 300], due to twin boundaries at the surface of the LAO [71] and therefore formation of various defects acting as pinning centers. With increasing BHO content, an overlap of the normal core surface, the core volume and the normal core volume pinning mechanism could be observed.

A comparison of samples grown with quasi-multilayer technique and samples by Lee proved to be problematic, since Lee's targets were premixed and only the nominal amount of BZO was given. Furthermore, Lee et al. calculated the j_c - and therefore the F_p -values with the Bean model [119]. For this work however, the values were measured over a bridge. The samples in the work of Lee exhibited film thicknesses of 400 nm, whereas the quasi-multilayered samples in this work show a maximum thickness of 110 nm. Consequently, Lee uses idealized values, whereas this work is influenced by various errors such as deviations in the thickness and width of the bridge, lattice quality deviations in the bridge as well as possibly suboptimal distribution of nanoparticles. The sample size for Ba122 samples with artificial perovskite pinning centers is too small, since the research done by Lee et al. [23] and Miura et al. [24] is the only research yet performed on implementation of perovskites as pinning materials in FBS. It requires more research to enable a veritable comparison of Lee's results and the results of this work.

The distances between the nanocolumns and their diameters in the TEM image of the sample with 3.85 mol% were measured within the TEM image.

The calculated distance values for the samples with 1.03 mol% and 1.59 mol% remained imprecise, because the inflection point could not be determined definitely and therefore had to be guessed. For some samples, more data points would have been of support, to enable determining a more exact matching field. However, the calculated diameter values matched the reported coherence length values in Co-doped Ba122 of circa 2.5 nm by Lee et al. [23]. The forming of vortex glass could be observed for the highest BHO content of 3.85 mol%. With increasing BHO content, the coherence lengths decrease (compressing the Cooper pairs) as well as the distance between pinning centers. For the sample with 1.59 mol% of BHO a small increase in distance could be observed, compared to the sample with 1.03 mol%. This could have most probably been evoked by inhomogeneous distribution of pinning centers in the sample with less BHO, as shown by TEM investigation.

The final investigation of this work focused on the implementation of InAs as a pinning material. The idea was to experiment with a material, which had never been used before, neither in FBS nor in YBCO compounds. Further criteria were that is

not an oxide and supplies the superconducting thin film with As in case of deficiency, to ensure a mostly pinning center free film despite implementation of artificial pinning centers. The implementation of InAs decreased the critical temperature with increasing doping level in the same manner other materials such as BHO and BZO do. The high vapor pressure of InAs was difficult to handle, to provide conditions for epitaxial growth of the superconductor and the pinning material. Optimal growth temperatures up to maximum 570 °C [82] were reported to lie significantly below the growth temperature of Ba122 on CaF₂ of 700 °C. The deployed deposition pattern made it possible to prepare samples with expected quality and properties. The measured InAs content did not correspond to the number of pulses most probably due to random re-evaporation of InAs during the deposition or formation of InAs-rich surface precipitates, which are not part of the pinning mechanism.

The critical current density values were enhanced by a factor of 6.48. A j_c dome formed in the graph of j_c as a function of pulses. The optimal number of pulses was 468 pulses. Higher amounts of pulses led to higher disorder, causing a decrease of superconducting properties such as j_c most probably by decrease of T_c . For lower amounts of pulses, the pinning is most likely not yet optimal. Perhaps, not enough or not large enough pinning centers are present to contain the appearing flux lines. The pinning force densities corresponded to this assumption, however for 390 pulses and for 585 pulses, pinning force densities showed higher values than for the highest j_c sample. The maximum pinning force density for all samples was identified at 6 T, which is fairly low compared to the samples with incorporated BHO. The pinning mechanism could be determined based on the work of Dew-Hughes to normal core point pinning [37, p. 298, 300]. The reason for this pinning mechanism were point defects, which can only interact with only one flux line at a time [37, p. 295] and an increase of InAs content, resulting in higher numbers of point defects interacting with one flux line until an optimum of j_c is reached. Beyond that optimum, the increasing content only caused disorder in the lattice and the critical current density decreased again. Obviously, c-axis pinning was enhanced for InAs level with highest j_c , despite no dependence on number of pulses. . Consequently, vortices were not properly pinned (liquid vortex) causing a decrease of the critical current density.

The calculated coherence lengths compared to the nominal value of 2.5 nm [23] were in the range of scattering.

4 Outlook

The results of this work are a first impression of possible future experiments and a glance into an undiscovered topic. The iron-based superconductors show great potential for further applications such as tapes, cables and coils by applying e.g. the powder-in-tube-technique [15]. Besides this work and its underlying literature, no research has been performed on the difficult quasi-multilayer technique to implement artificial pinning centers. Additional results for samples prepared with this technique would pave the way for further explorations and make the results of this work more comparable. The next step could be to retry the experiments mentioned in this work with premixed targets, to investigate the reproducibility of the results with regards to electrical transport properties. The pinning material content has to be determined by several experiments such as ICP-MS or EDX quantity measurements in TEM. In further investigations, it might be possible to calibrate the number of pulses to a certain amount of pinning material incorporated in the film, enabling a needs based preparation of samples with a defined content of pinning material for each experiment.

TEM investigations on pristine Co-doped Ba122 films on LAO substrate could show more clearly the effect on the film growth and superconducting properties of the twin boundaries on the substrate surface.

The transport measurements could be performed at higher external magnetic fields, allowing the defect structure to be identified more easily based on the work of Dew-Hughes [37], since the plots could only be identified for the first part of the curves. Including the last part of the curves could bring more detail and prove to the findings of the pinning mechanisms.

With those results powder-in-tube tapes can be produced to increase their current carrying capacity. The research on Ba122 PIT tubes already achieved critical current densities above the application relevant level [15] in the range of already in-use NbTi wires for high field applications, such as the Large Hadron Collider at CERN in Geneva [17, 18]. The continuation of this work's research can lead to a deeper understanding of the optimal doping or implementation process as well as level of artificial pinning centers, increasing the technically relevant properties of those Ba122 wires even further. This creates a wide range of opportunities for research - especially with new and larger particle accelerators to investigate the fundamental mechanisms of the universe. Besides the investigation approach, e.g. resolution capacities of computer tomography scanning can be enhanced, creating opportunities to detect and cure diseases such as cancer earlier and more efficient. In the future, it may be even possible to design the

optimal shape and distribution of pinning centers in such superconductors fitting to their application.

To achieve a complete understanding of the pinning mechanisms and implementation of artificial pinning centers in Ba122, the technical equipment for further experiments has to be adapted. The lasers for such experiments need higher energy densities as well as higher repetition frequencies to provide higher growth rates to improve the quality of the PLD-grown superconducting thin films [19, 70]. An approach could even be to experiment with a multi-laser system. One laser could be used for each target to obtain an optimal distribution of nanoparticles in the films. This could be very advantageous for a machine where long tapes or substrates will be coated. Another possibility could be a particle source supplying nanoparticles of artificial pinning material with a constant amount of material per time during the deposition process to obtain optimal nanoparticle distribution regardless of growth temperature, laser energy, frequency and deposition pattern.

Further experiments need to be performed regarding the implementation of InAs in FBS thin films. Different measures need to be taken to find the pinning centers and to ensure a reliable measurement of InAs content in the film. The usage of a particle source could be a perfect application for implementation of InAs to obtain optimal growth of InAs particles. Especially the way InAs is embedded in the matrix poses an interesting question. Is it split up in In and As and does the arsenic occupy possible As vacancies in the film?

Besides InAs, the attempt of using e.g. GaAs or other arsenides as pinning material, which are more stable and perhaps easier to handle with PLD, could yield further interesting findings.

Finally, measurements of resistance as a function of the applied magnetic field could also provide new information about the behavior of artificial pinning centers in FBS, especially the transitions such as glass-liquid transition etc.

Bibliography

- [1] ICHINOSE, A. ; NAOE, K. ; HORIDE, T. ; MATSUMOTO, K. ; KITA, R. ; MUKAIDA, M. ; YOSHIDA, Y. ; HORII, S.: Microstructures and critical current densities of YBCO films containing structure-controlled BaZrO₃ nanorods. In: *Superconductor Science and Technology* 20 (2007), Nr. 12, S. 1144–1150
- [2] KIESSLING, A. ; HÄNISCH, J. ; THERSLEFF, T. ; REICH, E. ; WEIGAND, M. ; HÜHNE, R. ; SPARING, M. ; HOLZAPFEL, B. ; DURRELL, J. ; SCHULTZ, L.: Nanocolumns in YBa₂Cu₃O_{7-x}/BaZrO₃ quasi-multilayers: formation and influence on superconducting properties. In: *Superconductor Science and Technology* 24 (2011), Nr. 5, S. 55018
- [3] KAMIHARA, Y. ; WATANABE, T. ; HIRANO, M. ; HOSONO, H.: Iron-Based Layered Superconductor La[O_{1-x}F_x]FeAs (x = 0.05-0.12) with T_c = 26 K. In: *Journal of the American Chemical Society* 130 (2008), Nr. 11, S. 3296–3297
- [4] YURI IZYUMOV, Ernst K.: *High-Tc Superconductors Based on FeAs Compounds*. Springer-Verlag GmbH, 2010 https://www.ebook.de/de/product/11903638/yuri_izyumov_ernst_kurmaev_high_tc_superconductors_based_on_feas_compounds.html. – ISBN 3642145299
- [5] CHEN, Xianhui ; DAI, Pengcheng ; FENG, Donglai ; XIANG, Tao ; ZHANG, Fu-Chun: Iron-based high transition temperature superconductors. In: *National Science Review* 1 (2014), jul, Nr. 3, S. 371–395. <http://dx.doi.org/10.1093/nsr/nwu007>. – DOI 10.1093/nsr/nwu007
- [6] IIDA, K. ; HÄNISCH, J. ; TARANTINI, C. ; KURTH, F. ; JAROSZYNSKI, J. ; UEDA, S. ; NAITO, M. ; ICHINOSE, A. ; TSUKADA, I. ; REICH, E. ; GRINENKO, V. ; SCHULTZ, L. ; HOLZAPFEL, B.: Oxypnictide SmFeAs(O,F) superconductor: a candidate for high-field magnet applications. In: *Scientific Reports* 3 (2013), S. 2139
- [7] TARANTINI, C. ; GUREVICH, A. ; JAROSZYNSKI, J. ; BALAKIREV, F. ; BELLINGERI, E. ; FERDEGHINI, I. Pallecchi C. ; SHEN, B. ; WEN, H. ; LARBALESTIER, D.: Significant enhancement of upper critical fields by doping and strain in iron-based superconductors. In: *Phys. Rev. B* 84 (2011), Nr. 18, S. 184522

- [8] PALLECCHI, Ilaria ; EISTERER, Michael ; MALAGOLI, Andrea ; PUTTI, Marina: Application potential of Fe-based superconductors. In: *Superconductor Science and Technology* 28 (2015), Nr. 114005. <http://dx.doi.org/10.1088/0953-2048/28/11/114005>. – DOI 10.1088/0953-2048/28/11/114005
- [9] PUTTI, M ; PALLECCHI, I ; BELLINGERI, E ; CIMBERLE, M R. ; TROPEANO, M ; FERDEGHINI, C ; PALENZONA, A ; TARANTINI, C ; YAMAMOTO, A ; JIANG, J ; JAROSZYNSKI, J ; KAMETANI, F ; ABRAIMOV, D ; POLYANSKII, A ; WEISS, J D. ; HELLSTROM, E E. ; GUREVICH, A ; LARBALESTIER, D C. ; JIN, R ; SALES, B C. ; SEFAT, A S. ; MCGUIRE, M A. ; MANDRUS, D ; CHENG, P ; JIA, Y ; WEN, H H. ; LEE, S ; EOM, C B.: New Fe-based superconductors: properties relevant for applications. In: *Superconductor Science and Technology* 23 (2010), feb, Nr. 3, S. 034003. <http://dx.doi.org/10.1088/0953-2048/23/3/034003>. – DOI 10.1088/0953-2048/23/3/034003
- [10] CHO, Kyuil ; FENTE, A. ; TEKNOWIJOYO, S. ; TANATAR, M. A. ; JOSHI, K. R. ; NUSRAN, N. M. ; KONG, T. ; MEIER, W. R. ; KALUARACHCHI, U. ; GUILLAMÓN, I. ; SUDEROW, H. ; BUD'KO, S. L. ; CANFIELD, P. C. ; PROZOROV, R.: Nodeless multiband superconductivity in stoichiometric single-crystalline $\text{CaKFe}_4\text{As}_4$. In: *Physical Review B* 95 (2017), mar, Nr. 10. <http://dx.doi.org/10.1103/physrevb.95.100502>. – DOI 10.1103/physrevb.95.100502
- [11] KATASE, T. ; HIRAMATSU, H. ; YANAGI, H. ; KAMIYA, T. ; HIRANO, M. ; HOSONO, H.: Atomically-flat, chemically-stable, superconducting epitaxial thin film of iron-based superconductor, cobalt-doped BaFe_2As_2 . In: *Solid State Commun.* 149 (2009), Nr. 47-48, S. 2121-2124
- [12] KATASE, T. ; HIRAMATSU, H. ; KAMIYA, T. ; HOSONO, H.: High Critical Current Density 4 MA/cm² in Co-Doped BaFe_2As_2 Epitaxial Films Grown on (La,Sr)(Al,Ta)O₃ Substrates without Buffer Layers. In: *Appl. Phys. Express* 3 (2010), Nr. 5, S. 055007
- [13] MAIOROV, B. ; KATASE, T. ; BAILY, S. A. ; HIRAMATSU, H. ; HOLESINGER, T. G. ; HOSONO, H. ; CIVALE, L.: Liquid vortex phase and strong c-axis pinning in low anisotropy $\text{BaCo}_x\text{Fe}_{2-x}\text{As}_2$ pnictide films. In: *Superconductor Science and Technology* 24 (2011), Nr. 055007. <http://dx.doi.org/10.1088/0953-2048/24/5/055007>. – DOI 10.1088/0953-2048/24/5/055007
- [14] WEISS, J. D. ; TARANTINI, C. ; JIANG, J. ; KAMETANI, F. ; POLYANSKII, A. A. ; LARBALESTIER, D. C. ; HELLSTROM, E. E.: High intergrain critical current density in fine-grain $(\text{Ba}_{0.6}\text{K}_{0.4})\text{Fe}_2\text{As}_2$ wires and bulks. In: *Nature Materials* 11 (2012), may, Nr. 8, S. 682-685. <http://dx.doi.org/10.1038/nmat3333>. – DOI 10.1038/nmat3333

-
- [15] YAO, C. ; MA, Y.: Recent breakthrough development in iron-based superconducting wires for practical applications. In: *Superconductor Science and Technology* 32 (2019), Nr. 2, S. 23002
- [16] MA, Yanwei: Progress in wire fabrication of iron-based superconductors. In: *Superconductor Science and Technology* 25 (2012), sep, Nr. 11, S. 113001. <http://dx.doi.org/10.1088/0953-2048/25/11/113001>. – DOI 10.1088/0953-2048/25/11/113001
- [17] ITOH, I. ; SASAKI, T.: Critical current density of superconducting NbTi/Nb/Cu multilayer composite sheets. In: *Cryogenics* 35 (1995), jun, Nr. 6, S. 403–404. [http://dx.doi.org/10.1016/0011-2275\(95\)99821-o](http://dx.doi.org/10.1016/0011-2275(95)99821-o). – DOI 10.1016/0011-2275(95)99821-o
- [18] BOUTBOUL, T. ; NAOUR, S. L. ; LEROY, D. ; OBERLI, L. ; PREVITALI, V.: Critical Current Density in Superconducting Nb-Ti Strands in the 100 mT to 11 T Applied Field Range. In: *IEEE Transactions on Applied Superconductivity* 16 (2006), jun, Nr. 2, S. 1184–1187. <http://dx.doi.org/10.1109/tasc.2006.870777>. – DOI 10.1109/tasc.2006.870777
- [19] LANGER, M. ; MEYER, S. ; ACKERMANN, K. ; GRÜNEWALD, L. ; KAUFFMANN-WEISS, S. ; ASWARTHAM, S. ; WURMEHL, S. ; HÄNISCH, J. ; HOLZAPFEL, B.: On the growth of Co-doped BaFe₂As₂ thin films on CaF₂. In: *Journal of Physics: Conference Series (JPCS)* (2019)
- [20] MIURA, Masashi ; MAIOROV, Boris ; KATO, Takeharu ; SHIMODE, Takashi ; WADA, Keisuke ; ADACHI, Seiji ; TANABE, Keiichi: Strongly enhanced flux pinning in one-step deposition of BaFe₂(As_{0.66}P_{0.33})₂ superconductor films with uniformly dispersed BaZrO₃ nanoparticles. In: *Nature Communications* 4 (2013), Nr. 2499. <http://dx.doi.org/doi:10.1038/ncomms3499>. – DOI doi:10.1038/ncomms3499
- [21] HÄNISCH, J. ; CAI, C. ; STEHR, V. ; HÜHNE, R. ; LYUBINA, J. ; NENKOV, K. ; FUCHS, G. ; SCHULTZ, L. ; HOLZAPFEL, B.: Formation and pinning properties of growth-controlled nanoscale precipitates in YBa₂Cu₃O_{7- δ} transition metal quasimultilayers. In: *Superconductor Science and Technology* 19 (2006), Nr. 6, S. 543–540
- [22] HORIDE, T. ; ISHIMARU, M. ; MATSUMOTO, K.: Observation of inhomogeneous depinning in YBa₂Cu₃O₇ composite multilayers. In: *Superconductor Science and Technology* 32 (2019), Nr. 8, S. 85001
- [23] LEE, Jongmin ; JIANG, Jianyi ; KAMETANI, Fumitake ; OH, Myeong J. ; WEISS, Jeremy D. ; COLLANTES, Yesusa ; SEO, Sehun ; YOON, Sejun ; TARANTINI, Chiara ; JO, Youn J. ; HELLSTROM, Eric E. ; LEE, Sanghan: High critical
-

- current density over 1 MA/cm² at 13 T in BaZrO₃ incorporated Ba(Fe,Co)₂As₂ thin film. In: *Superconductor Science and Technology* 30 (2017), Nr. 8. <http://dx.doi.org/10.1088/1361-6668/aa73f5>. – DOI 10.1088/1361-6668/aa73f5
- [24] MIURA, M. ; TSUCHIYA, G. ; HARADA, T. ; TANABE, K. ; KIUCHI, M. ; MATSUSHITA, T.: Enhanced critical current density in BaFe₂(As_{0.66}P_{0.33})₂ nanocomposite superconducting films. In: *Superconductor Science and Technology* 32 (2019), Nr. 6, S. 64005
- [25] KURTH, F. ; IIDA, K. ; TROMMLER, S. ; HÄNISCH, J. ; NENKOV, K. ; ENGELMANN, J. ; OSWALD, S. ; WERNER, J. ; SCHULTZ, L. ; HOLZAPFEL, B. ; HAINDL, S.: Electronic phase diagram of disordered Co doped BaFe₂As_{2-δ}. In: *Superconductor Science and Technology* 26 (2013), Nr. 025014. <http://dx.doi.org/10.1088/0953-2048/26/2/025014>. – DOI 10.1088/0953-2048/26/2/025014
- [26] KALSİ, S. S.: *Applications of High Temperature Superconductors to Electric Power Equipment*. Wiley-IEEE Press, 2011
- [27] W. BUCKEL, R. K.: *Superconductivity - Fundamentals and Applications*. 2nd. Wiley, 2004
- [28] TINKHAM, Michael: *Introduction to Superconductivity: Second Edition (Dover Books on Physics) (Vol I)*. 2. Dover Publications, 2004 <http://www.worldcat.org/isbn/0486435032>. – ISBN 0486435032
- [29] KURTH, Fritz: *High Magnetic Field Properties of Fe - Pnictide Thin Films*, Technische Universität Dresden, Diss., 2015
- [30] SPARING, Maria: *Integration von gasphasenkondensierten Nanopartikeln in YBa₂Cu₃O_{7-δ} Multilagen*, Technische Universität Dresden, Diss., 2012
- [31] AWAJI, Satoshi ; WATANABE, Kazuo ; KOBAYASHI, Norio: Crossover from intrinsic to extrinsic pinning for YBa₂Cu₃O₇ films. In: *Cryogenics* 39 (1999), jul, Nr. 7, S. 569–577. [http://dx.doi.org/10.1016/s0011-2275\(99\)00079-x](http://dx.doi.org/10.1016/s0011-2275(99)00079-x). – DOI 10.1016/s0011-2275(99)00079-x
- [32] KÜPFER, H. ; APFELSTEDT, I. ; FLÜKIGER, R. ; KELLER, C. ; MEIER-HIRMER, R. ; RUNTSCH, B. ; TUROWSKI, A. ; WIECH, U. ; WOLF, T.: Intragrain junctions in YBa₂Cu₃O_{7-x} ceramics and single crystals. In: *Cryogenics* 29 (1989), mar, Nr. 3, S. 268–280. [http://dx.doi.org/10.1016/0011-2275\(89\)90172-0](http://dx.doi.org/10.1016/0011-2275(89)90172-0). – DOI 10.1016/0011-2275(89)90172-0
- [33] CARDWELL, David A. ; GINLEY, David S.: *Handbook of Superconducting Materials*. Bd. I: Superconductivity, Materials and Processes. CRC Press, 2003

-
- [34] LEE, Y. ; YAMASAKI, H. ; FURUSE, M.: Magnetic-field angle dependent critical current densities and flux pinning in commercial YBCO tapes below liquid nitrogen temperatures. In: *Physica C: Superconductivity and its Applications* 471 (2011), Nr. 21, S. 1017–1020
- [35] DEMTRÖDER, W.: *Experimentalphysik 2: Elektrizität und Optik*. Bd. 5. Springer Verlag, 2009
- [36] MATSUSHITA, Teruo: *Flux Pinning in Superconductors*. Springer Berlin Heidelberg, 2010 https://www.ebook.de/de/product/13771338/teruo_matsushita_flux_pinning_in_superconductors.html. – ISBN 3642079458
- [37] DEW-HUGHES, D.: Flux pinning mechanisms in type II superconductors. In: *Philosophical Magazine* 30 (1974), Nr. 2, S. 293–305. <http://dx.doi.org/10.1080/14786439808206556>. – DOI 10.1080/14786439808206556
- [38] NEXANS: -. -. https://www.nexans.de/Germany/2013/bbr_070813_42_47_Hobl.pdf. Version: 29 of august 2020
- [39] NEXANS: -. -. https://www.nexans.de/Corporate/2014/1405_Nexans_AmpaCity_GB.pdf. Version: 29 of august 2020
- [40] LUCIO ROSSI: *Superconductivity and the LHC: the early days*. CERN COURIER. https://www.lhc-closer.es/taking_a_closer_look_at_lhc/0.magnetic_dipoles. Version: 2011
- [41] JONATHAN FILDES: *The 'new age' of super materials*. BBC News. <http://news.bbc.co.uk/2/hi/technology/6412057.stm>. Version: march 2007
- [42] THE JAPAN TIMES: -. -. <https://www.japantimes.co.jp/opinion/2014/10/22/editorials/maglev-line-gets-green-light/#.X0uFnItCSUk>. Version: 30th of august 2020
- [43] FLUCK, E.: New notations in the periodic table. In: *Pure and Applied Chemistry* 60 (1988), Nr. 3, S. 431–436
- [44] MANDRUS, David ; SEFAT, Athena S. ; MCGUIRE, Michael A. ; SALES, Brian C.: Materials Chemistry of BaFe₂As₂: A Model Platform for Unconventional Superconductivity. In: *Chemistry of Materials* 22 (2010), S. 715–723. <http://dx.doi.org/10.1021/cm9027397>. – DOI 10.1021/cm9027397
- [45] IIDA, K. ; HÄNISCH, J. ; HÜHNE, R. ; KURTH, F. ; KIDSZUN, M. ; HAINDL, S. ; WERNER, J. ; SCHULTZ, L. ; HOLZAPFEL, B.: Strong T_c dependence for strained epitaxial Ba(Fe_{1-x}Co_x)₂As₂ thin films. In: *Appl. Phys. Lett.* 95 (2009), Nr. 19, S. 192501
-

- [46] CHARAEV, I ; SEMENOV, A ; DOERNER, S ; GOMARD, G ; ILIN, K ; SIEGEL, M: Current dependence of the hot-spot response spectrum of superconducting single-photon detectors with different layouts. In: *Superconductor Science and Technology* 30 (2016), dec, Nr. 2, S. 025016. <http://dx.doi.org/10.1088/1361-6668/30/2/025016>. – DOI 10.1088/1361-6668/30/2/025016
- [47] ENGELMANN, J. ; GRINENKO, V. ; CHEKHONIN, P. ; SKROTZKI, W. ; EFREMOV, D.V. ; OSWALD, S. ; IIDA, K. ; HÜHNE, R. ; HÄNISCH, J. ; HOFFMANN, M. ; KURTH, F. ; SCHULTZ, L. ; HOLZAPFEL, B.: Strain induced superconductivity in the parent compound BaFe₂As₂. In: *Nature Communications* 4 (2013), Nr. 2877. <http://dx.doi.org/10.1038/ncomms3877>. – DOI 10.1038/ncomms3877
- [48] DUNCAN, W. J. ; WELZEL, O. P. ; HARRISON, C. ; WANG, X. F. ; CHEN, X. H. ; GROSCHE, F. M. ; NIKLOWITZ, P. G.: High pressure study of BaFe₂As₂ - the role of hydrostaticity and uniaxial stress. In: *Journal of Physics: Condensed Matter* 22 (2010), Nr. 5, S. 052201
- [49] ROTTER, Marianne ; TEGEL, Marcus ; JOHRENDT, Dirk: Superconductivity at 38 K in the iron arsenide (Ba_{1-x}K_x)Fe₂As₂. In: *Phys. Rev. Lett.* 101:107006 (2008)
- [50] LEE, N. H. ; JUNG, S.-G. ; KIM, D. H. ; KANG, W. N.: Potassium-doped BaFe₂As₂ superconducting thin films with a transition temperature of 40 K. In: *Appl. Phys. Lett.* 96 (2010), Nr. 20, S. 202505
- [51] JIANG, S. ; XING, H. ; XUAN, G. ; WANG, C. ; REN, Z. ; FENG, C. ; DAI, J. ; XU, Z. ; CAO, G.: Superconductivity up to 30 K in the vicinity of the quantum critical point in BaFe₂(As_{1-x}P_x)₂. In: *Journal of Physics: Condensed Matter* 21 (2009), Nr. 38, S. 382203
- [52] HIRAMATSU, Hidenori ; SATO, Hikaru ; KAMIYA, Toshio ; HOSONO, Hideo: BaFe₂(As_{1-x}P_x)₂ (x=0.22-0.42) thin films grown on practical metal-tape substrates and their critical current densities. In: *Superconductor Science and Technology* 30 (2017), Nr. 044003. <http://dx.doi.org/10.1088/1361-6668/aa621c>. – DOI 10.1088/1361-6668/aa621c
- [53] ADACHI, S ; SHIMODE, T ; MIURA, M ; CHIKUMOTO, N ; TAKEMORI, A ; NAKAO, K ; OSHIKUBO, Y ; TANABE, K: Pulsed laser deposition of BaFe₂(As,P)₂ superconducting thin films with high critical current density. In: *Superconductor Science and Technology* 25 (2012), sep, Nr. 10, S. 105015. <http://dx.doi.org/10.1088/0953-2048/25/10/105015>. – DOI 10.1088/0953-2048/25/10/105015
- [54] NI, N. ; TILLMAN, M. E. ; YAN, J.-Q. ; KRACHER, A. ; HANNAHS, S. T. ; BUD'KO, S. L. ; CANELD, P. C.: Effects of Co substitution on thermodynamic and transport properties and anisotropic H_{c2} in Ba(Fe_{1-x}Co_x)₂As₂ single crystals. In: *Phys. Rev. B* 78:214515 (2008)

-
- [55] DEMTRÖDER, W.: *Experimentalphysik 3: Atome, Moleküle und Festkörper*. Bd. 5. Springer Verlag, 2016
- [56] BAUER, E. ; POPPA, H.: Recent Advantages in Epitaxy. In: *Thin Solid Films* 12 (1972), S. 167–185
- [57] FRANK, F. C. ; MERWE, J. H. d.: One-Dimensional Dislocations. I. Static Theory Proceedings of the Royal Society of London. In: *Series A: Mathematical and Physical Sciences* 198 (1949), Nr. 1053, S. 205–216
- [58] FRANK, F. C. ; MERWE, J. H. d.: One-Dimensional Dislocations. II. Misfitting Monolayers and Oriented Overgrowth Proceedings of the Royal Society of London. In: *Series A: Mathematical and Physical Sciences* 200 (1949), Nr. 1060, S. 125–134
- [59] FRANK, F. C. ; MERWE, J. H. d.: One-Dimensional Dislocations. III. Influence of the Second Harmonic Term in the Potential Representation on the Properties of the Model Proceedings of the Royal Society of London. In: *Series A: Mathematical and Physical Sciences* 198 (1949), Nr. 1053, S. 216–225
- [60] VOLMER, M. ; A.WEBER: Keimbildung in übersättigten Gebilden. In: *Z. phys. Chem.* 119 (1926), S. 277–301
- [61] STRANSKI, I. N. ; KRASTANOV, L.: Zur Theorie der orientierten Ausscheidung von Ionenkristallen aufeinander. In: *Sitzungsber. Akad. Wiss. Wien. Math.-Naturwiss.* 146 (1938), S. 797–810
- [62] LEE, S. ; JIANG, J. ; ZHANG, Y. ; BARK, C.W. ; D.WEISS, J. ; TARANTINI, C. ; NELSON, C. T. ; JANG, H.W. ; FOLKMAN, C. M. ; BAEK, S. H. ; POLYANSKII, A. ; ABRAIMOV, D. ; YAMAMOTO, A. ; PARK, J.W. ; PAN, X. Q. ; HELLSTROM, E. E. ; LARBALESTIER, D. C. ; EOM, C. B.: Template engineering of Co-doped BaFe₂As₂ single-crystal thin films. In: *Nature Materials* 9 (2010), S. 397–402. <http://dx.doi.org/10.1038/nmat2721>. – DOI 10.1038/nmat2721
- [63] THERSLEFF, T. ; IIDA, K. ; HAINDL, S. ; KIDSZUN, M. ; POHL, D. ; HARTMANN, A. ; KURTH, F. ; HÄNISCH, J. ; HÜHNE, R. ; RELLINGHAUS, B. ; SCHULTZ, L. ; HOLZAPFEL, B.: Coherent interfacial bonding on the FeAs tetrahedron in Fe/Ba(Fe_{1-x}Co_x)₂As₂ bilayers. In: *Applied Physics Letters* 97 (2010), jul, Nr. 2, S. 022506. <http://dx.doi.org/10.1063/1.3457432>. – DOI 10.1063/1.3457432
- [64] SATO, Hikaru ; HIRAMATSU, Hidenori ; KAMIYA, Toshio ; HOSONO, Hideo: High critical-current density with less anisotropy in BaFe₂(As,P)₂ epitaxial thin films: Effect of intentionally grown c-axis vortex-pinning centers. In: *Applied Physics Letters* 104 (2014), Nr. 182603. <http://dx.doi.org/10.1063/1.4875956>. – DOI 10.1063/1.4875956
-

- [65] HAINDL, S. ; KIDSZUN, M. ; OSWALD, S. ; HESS, C. ; BÜCHNER, B. ; KÖLLING, S. ; WILDE, L. ; THERSLEFF, T. ; YURCHENKO, V. V. ; JOURDAN, M. ; HIRAMATSU, H. ; HOSONO, H.: Thin film growth of Fe-based superconductors: from fundamental properties to functional devices. A comparative review. In: *Reports on Progress in Physics* 77 (2014), apr, Nr. 4, 046502. <http://dx.doi.org/10.1088/0034-4885/77/4/046502>. – DOI 10.1088/0034-4885/77/4/046502
- [66] CONTARINO, D. ; LÖHNERT, C. ; JOHRENDT, D. ; GENOVESE, A. ; BERNINI, C. ; MALAGOLI, A. ; PUTTI, M.: Development and Characterization of P-doped Ba-122 Superconducting Tapes. In: *IEEE Transactions on Applied Superconductivity* 27 (2017), Nr. 4, S. 1–4
- [67] TSAIH, Wen-Chou ; HUANG, Chin-Kuan ; TSENG, Tseung-Yuen: Growth of CeO₂ Films on Sapphire and MgO by rf Magnetron Sputtering. In: *Journal of the American Ceramic Society* 78 (1995), Nr. 7, S. 1969–1973
- [68] DATASHEET MGO BY CRYSTEC GMBH: -. -. <http://www.crystec.de/mgo-e.html>. Version: März 22 of march 2020
- [69] DATASHEET LAO BY CRYSTEC GMBH: -. -. www.crystec.de/daten/laalo3.pdf. Version: März 22 of march 2020
- [70] HIRAMATSU, Hidenori ; SATO, Hikaru ; KATASE, Takayoshi ; KAMIYA, Toshio ; HOSONO, Hideo: Critical factor for epitaxial growth of cobalt-doped BaFe₂As₂ films by pulsed laser deposition. In: *Applied Physics Letters* 104 (2014), Nr. 172602. <http://dx.doi.org/10.1063/1.4874609>. – DOI 10.1063/1.4874609
- [71] LEHMANN, A. G. ; SANNA, C. ; LAMPIS, N. ; CONGIU, F. ; CONCAS, G. ; MARITATO, L. ; ARUTA, C. ; PETROV, A. Y.: Effect of the substrate ferroelastic transition on epitaxial La_{0.7}Sr_{0.3}MnO₃ films grown on LaAlO₃. In: *The European Physical Journal B* 55 (2007), feb, Nr. 4, S. 337–345. <http://dx.doi.org/10.1140/epjb/e2007-00077-7>. – DOI 10.1140/epjb/e2007-00077-7
- [72] KRISHNASWAMY, K. ; DREYER, C. E. ; JANOTTI, A. ; WALLE, C. G. V.: Structure and energetics of LaAlO₃(001) surfaces. In: *Physical Review B* 90 (2014), dec, Nr. 23. <http://dx.doi.org/10.1103/physrevb.90.235436>. – DOI 10.1103/physrevb.90.235436
- [73] DATASHEET CAF₂ BY CRYSTEC GMBH: -. -. www.crystec.de/caf2-d.html. Version: 22 of march 2020
- [74] TARANTINI, C. ; KAMETANI, F. ; LEE, S. ; JIANG, J. ; WEISS, J.D. ; JAROSZYNSKI, J. ; HELLSTROM, E.E. ; EOM, C. B. ; LARBALESTIER, D.C.: Development of very high J_c in Ba(Fe_{1-x}Co_x)₂As₂ thin films grown on CaF₂. In: *Scientific*

-
- Reports* 4 (2014), Nr. 7305. <http://dx.doi.org/10.1038/srep07305>. – DOI 10.1038/srep07305
- [75] ROTTER, Marianne ; HIEKE, Christine ; JOHRENDT, Dirk: Different response of the crystal structure to isoelectronic doping in $\text{BaFe}_2(\text{As}_{1-x}\text{P}_x)_2$ and $(\text{Ba}_{1-x}\text{Sr}_x)\text{Fe}_2\text{As}_2$. In: *Physical Review B* 82 (2010), 01
- [76] DATASHEET BZO₃ BY KURT J. LESKER COMPANY: -. -. https://de.lesker.com/newweb/deposition_materials/depositionmaterials_sputtertargets_1.cfm?pgid=bazro3. Version: 22 of march 2020
- [77] YAMANAKA, Shinsuke ; FUJIKANE, Masaki ; HAMAGUCHI, Tsuyoshi ; MUTA, Hiroaki ; OYAMA, Taku ; MATSUDA, Tetsushi ; KOBAYASHI, Shin ichi ; KUROSAKI, Ken: Thermophysical properties of BaZrO_3 and BaCeO_3 . In: *Journal of Alloys and Compounds* 359 (2003), sep, Nr. 1-2, S. 109–113. [http://dx.doi.org/10.1016/s0925-8388\(03\)00214-7](http://dx.doi.org/10.1016/s0925-8388(03)00214-7). – DOI 10.1016/s0925-8388(03)00214-7
- [78] BRETOS, I. ; SCHNELLER, T. ; M. ; BÄCKER, M. ; HOLLMANN, E. ; WÖRDENWEBER, R. ; MOLINA-LUNA, L. ; TENDELOO, G. V. ; EIBL, O.: Solution-derived $\text{YBa}_2\text{Cu}_3\text{O}_{7-\delta}$ (YBCO) superconducting films with BaZrO_3 (BZO) nanodots based on reverse micelle stabilized nanoparticles. In: *Journal of Materials Chemistry C* 3 (2015), Nr. 16, S. 3971–3979. <http://dx.doi.org/10.1039/c4tc02543a>. – DOI 10.1039/c4tc02543a
- [79] MATSUMOTO, Kaname ; MELE, Paolo: Artificial pinning center technology to enhance vortex pinning in YBCO coated conductors. In: *Superconductor Science and Technology* 23 (2009), dec, Nr. 1, S. 014001. <http://dx.doi.org/10.1088/0953-2048/23/1/014001>. – DOI 10.1088/0953-2048/23/1/014001
- [80] ZHANG, J. L. ; EVETTS, J. E.: BaZrO_3 and BaHfO_3 : preparation, properties and compatbility with $\text{YBa}_2\text{Cu}_3\text{O}_{7-x}$. In: *Journal of Materials Science* 29 (1994), S. 778–785
- [81] ERBE, M. ; HÄNISCH, J. ; HÜHNE, R. ; FREUDENBERG, T. ; KIRCHNER, A. ; MOLINA-LUNA, L. ; DAMM, C. ; TENDELOO, G. V. ; KASKEL, S. ; SCHULTZ, L. ; HOLZAPFEL, B.: BaHfO_3 artificial pinning centres in TFA-MOD-derived YBCO and GdBCO thin films. In: *Superconductor Science and Technology* 28 (2015), sep, Nr. 11, S. 114002. <http://dx.doi.org/10.1088/0953-2048/28/11/114002>. – DOI 10.1088/0953-2048/28/11/114002
- [82] OKIMURA, H. ; KANNEWURF, C. R. ; BRITAIN, J. O.: Preparation and electrical properties of InAs thin films. In: *Journal of Electronic Materials* 7 (1978), sep, Nr. 5, S. 627–637. <http://dx.doi.org/10.1007/bf02655438>. – DOI 10.1007/bf02655438
-

- [83] DATASHEET OF INAs BY ALINEASON MATERIALS TECHNOLOGY GMBH: -. - . <https://www.alineason.com/produkt/indiumarsenid/>. Version:22 of march 2020
- [84] LOWNDES, D. H. ; GEOHEGAN, D. B. ; PURETZKY, A. A. ; NORTON, D. P. ; ROULEAU, C. M.: Synthesis of Novel Thin-Film Materials by Pulsed Laser Deposition. In: *Science* 273 (1996), aug, Nr. 5277, S. 898–903. <http://dx.doi.org/10.1126/science.273.5277.898>. – DOI 10.1126/science.273.5277.898
- [85] KIENEL, G.: *Vakuumbeschichtung 4. Anwendungen*. Bd. 1. VDI Verlag, 1993
- [86] QUANTUM DESIGN: *Physical Property Measurement System - Hardware Manual*. -. https://web.njit.edu/~tyson/PPMS_Documents/PPMS_Manual/1070-150%20Rev.%20B5%20PQ%20%20PPMS%20Hardware.pdf. Version:29th of may 2020
- [87] HASEGAWA, S. ; GREY, F.: Electronic transport at semiconductor surfaces—from point-contact transistor to micro-four-point probes. In: *Surface Science* 500 (2002), mar, Nr. 1-3, S. 84–104. [http://dx.doi.org/10.1016/s0039-6028\(01\)01533-3](http://dx.doi.org/10.1016/s0039-6028(01)01533-3). – DOI 10.1016/s0039-6028(01)01533-3
- [88] SPIESS, Lothar ; TEICHERT, Gerd ; SCHWARZER, Robert ; BEHNKEN, Herfried ; GENZEL, Christoph: *Moderne Röntgenbeugung*. Bd. 2. Springer Fachmedien, 2019
- [89] NELSON, J. B. ; RILEY, D. P.: An experimental investigation of extrapolation methods in the derivation of accurate unit-cell dimensions of crystals. In: *Proceedings of the Physical Society* 57 (1944), Nr. 3, S. 160
- [90] ICSD DATABASE: -. <https://icsd.fiz-karlsruhe.de/search/basic.xhtml>, 22 of march 2020
- [91] MCMULLAN, D.: Scanning electron microscopy 1928-1965. In: *Scanning* 17 (2006), dec, Nr. 3, S. 175–185. <http://dx.doi.org/10.1002/sca.4950170309>. – DOI 10.1002/sca.4950170309
- [92] EGERTON, R. F.: *Physical Principles of Electron Microscopy, An Introduction to TEM, SEM and AEM*. Bd. 2. Springer International Publishing, 2016
- [93] GOLDSTEIN, J. I. ; JOSEPH, I. ; NEWBURY, D. E. ; MICHAEL, J.R. ; RITCHIE, N. W. M. ; SCOTT, J. H. J.: *Scanning Electron Microscopy and X-Ray Microanalysis*. Springer Verlag GmbH, 2017 https://www.ebook.de/de/product/33399151/joseph_i_goldstein_dale_e_newbury_joseph_r_michael_nicholas_w_m_ritchie_john_henry_j_scott_scanning_electron_microscopy_and_x_ray_microanalysis.html. – ISBN 9781493966769

-
- [94] WILLIAMS, D. B. ; CARTER, C. B.: *Transmission Electron Microscopy - A Textbook for Materials Science*. Springer Verlag, 2009
- [95] WILSCHEFSKI, S. ; BAXTER, M. R.: Inductively Coupled Plasma Mass Spectrometry: Introduction to Analytical Aspects. In: *Clinical Biochemist Reviews* 40 (2019), aug, Nr. 3, S. 115–133. <http://dx.doi.org/10.33176/aacb-19-00024>. – DOI 10.33176/aacb-19-00024
- [96] ZHANG, Nan ; SULEIMAN, Jibrin S. ; HE, Man ; HU, Bin: Chromium(III)-imprinted silica gel for speciation analysis of chromium in environmental water samples with ICP-MS detection. In: *Talanta* 75 (2008), apr, Nr. 2, S. 536–543. <http://dx.doi.org/10.1016/j.talanta.2007.11.059>. – DOI 10.1016/j.talanta.2007.11.059
- [97] IIDA, Kazumasa ; SATO, Hikaru ; TARANTINI, Chiara ; HÄNISCH, Jens ; JAROSZYNSKI, Jan ; HIRAMATSU, Hidenori ; HOLZAPFEL, Bernhard ; HOSONO, Hideo: High-field transport properties of a P-doped BaFe₂As₂ film on technical substrate. In: *Scientific Reports* 7 (2017), Nr. 39951. <http://dx.doi.org/10.1038/srep39951>. – DOI 10.1038/srep39951
- [98] KATASE, Takayoshi ; HIRAMATSU, Hidenori ; MATIAS, Vladimir ; SHEEHAN, Chris ; ISHIMARU, Yoshihiro ; KAMIYA, Toshio ; TANABE, Keiichi ; HOSONO, Hideo: Biaxially textured cobalt-doped BaFe₂As₂ films with high critical current density over 1 MA/cm² on MgO-buffered metal-tape flexible substrates. In: *Applied Physics Letters* 98 (2011), Nr. 242510. <http://dx.doi.org/10.1063/1.3599844>. – DOI 10.1063/1.3599844
- [99] YUAN, H. Q. ; SINGLETON, J. ; BALAKIREV, F. F. ; BAILY, S. A. ; CHEN, G. F. ; LUO, J. L. ; WANG, N. L.: Nearly isotropic superconductivity in (Ba,K)Fe₂As₂. In: *Nature* 457 (2009), Nr. 565. <http://dx.doi.org/10.1038/nature07676>. – DOI 10.1038/nature07676
- [100] MOHAN, S. ; TAEN, T. ; YAGYUDA, H. ; NAKAJIMA, Y. ; TAMEGAI, T. ; KATASE, T. ; HIRAMATSU, H. ; HOSONO, H.: Characterization of epitaxial Co-doped BaFe₂As₂ thin films. In: *Physica C: Superconductivity and its Applications* 471 (2011), nov, Nr. 21-22, S. 1181–1184. <http://dx.doi.org/10.1016/j.physc.2011.05.153>. – DOI 10.1016/j.physc.2011.05.153
- [101] IIDA, K. ; HAINDL, S. ; KURTH, F. ; HÄNISCH, J. ; SCHULZ, L. ; HOLZAPFEL, B.: BaFe₂As₂/Fe Bilayers with [001]-tilt Grain Boundary on MgO and SrTiO₃ Bicrystal Substrates. In: *Physics Procedia* 45 (2013), S. 189–192. <http://dx.doi.org/10.1016/j.phpro.2013.04.084>. – DOI 10.1016/j.phpro.2013.04.084
- [102] SCHERRER, P.: Nachrichten von der Gesellschaft der Wissenschaften zu Göttingen. In: *Mathematisch-Physikalische Klasse* 2 (1918), S. 98–100
-

- [103] LANGFORD, J. I. ; WILSON, A. J. C.: Scherrer after sixty years: A survey and some new results in the determination of crystallite size. In: *Journal of Applied Crystallography* 11 (1978), apr, Nr. 2, S. 102–113. <http://dx.doi.org/10.1107/s0021889878012844>. – DOI 10.1107/s0021889878012844
- [104] GIFFIN, Nick A. ; MASUDA, Jason D.: Reactivity of white phosphorus with compounds of the p-block. In: *Coordination Chemistry Reviews* 255 (2011), Nr. 11-12, S. 1342–1359. <http://dx.doi.org/10.1016/j.ccr.2010.12.016>. – DOI 10.1016/j.ccr.2010.12.016
- [105] RUDBERG, Erik ; LEMPERS, Joseph: The Vapor Pressure of Barium. In: *The Journal of Chemical Physics* 3 (1935), oct, Nr. 10, S. 627–631. <http://dx.doi.org/10.1063/1.1749565>. – DOI 10.1063/1.1749565
- [106] DAI, X. H. ; LIANG, J. T. ; SONG, J. M. ; ZHAO, L. ; GUO, J. X. ; ZHAO, H. D. ; WANG, Y. ; LIU, B. T.: Effects of Deposition Temperature on the Structural and Physical Properties of Ba(Fe_{1.8}Co_{0.2})₂As₂ Thin Film. In: *Journal of Superconductivity and Novel Magnetism* (2018), July, 1-7. <http://dx.doi.org/10.1007/s10948-018-4800-y>. – DOI 10.1007/s10948-018-4800-y
- [107] IIDA, Kazumasa ; HÄNISCH, Jens ; TROMMLER, Sascha ; HAINDL, Silvia ; KURTH, Fritz ; HÜHNE, Ruben ; SCHULTZ, Ludwig ; HOLZAPFEL, Bernhard: Thickness dependence of structural and transport properties of Co-doped BaFe₂As₂ on Fe buffered MgO substrates. In: *Superconductor Science and Technology* 24 (2011), Nr. 125009. <http://dx.doi.org/10.1088/0953-2048/24/12/125009>. – DOI 10.1088/0953-2048/24/12/125009
- [108] IIDA, K. ; HÄNISCH, J. ; TARANTINI, C.: Fe-based superconducting thin films on metallic substrates: Growth, characteristics, and relevant properties. In: *Applied Physics Reviews* 5 (2018), S. 31304
- [109] MEYER, Sven ; LANGER, Marco ; GRÜNEWALD, Lukas ; HÄNISCH, Jens ; GERTHSEN, Dagmar ; HOLZAPFEL, Bernhard: Pulsed Laser Deposition of quasi-multilayer superconducting Ba(Fe_{0.92}Co_{0.08})₂As₂-BaHfO₃ nanocomposite films. In: *Journal of Physics: Conference Series* 1559 (2020), jun, S. 012052. <http://dx.doi.org/10.1088/1742-6596/1559/1/012052>. – DOI 10.1088/1742-6596/1559/1/012052
- [110] WERTHAMER, N. R. ; HELFAND, E. ; HOHENBERG, P. C.: Temperature and Purity Dependence of the Superconducting Critical Field, H_{c2}. III. Electron Spin and Spin-Orbit Effects. In: *Physical Review* 147 (1966), jul, Nr. 1, S. 295–302. <http://dx.doi.org/10.1103/physrev.147.295>. – DOI 10.1103/physrev.147.295

-
- [111] HORIDE, Tomoya ; TAGUCHI, Kenta ; MATSUMOTO, Kaname ; MATSUKIDA, Naoki ; ISHIMARU, Manabu ; MELE, Paolo ; KITA, Ryusuke: Influence of matching field on critical current density and irreversibility temperature in $\text{YBa}_2\text{Cu}_3\text{O}_7$ films with BaMO_3 ($M = \text{Zr, Sn, Hf}$) nanorods. In: *Applied Physics Letters* 108 (2016), feb, Nr. 8, S. 082601. <http://dx.doi.org/10.1063/1.4942463>. – DOI 10.1063/1.4942463
- [112] HORIDE, T ; MATSUMOTO, K ; ICHINOSE, A ; MUKAIDA, M ; YOSHIDA, Y ; HORII, S: Matching field effect of the vortices in $\text{GdBa}_2\text{Cu}_3\text{O}_{7-\delta}$ thin film with gold nanorods. In: *Superconductor Science and Technology* 20 (2007), feb, Nr. 4, S. 303–306. <http://dx.doi.org/10.1088/0953-2048/20/4/001>. – DOI 10.1088/0953-2048/20/4/001
- [113] HORIDE, Tomoya ; OTSUBO, Koji ; KITA, Ryusuke ; MATSUKIDA, Naoki ; ISHIMARU, Manabu ; AWAJI, Satoshi ; MATSUMOTO, Kaname: Strong-c-axis correlated pinning and hybrid pinning in $\text{YBa}_2\text{Cu}_3\text{O}_{7-\delta}$ films containing BaHfO_3 nanorods and stacking faults. In: *Superconductor Science and Technology* 30 (2017), jun, Nr. 7, S. 074009. <http://dx.doi.org/10.1088/1361-6668/aa70d3>. – DOI 10.1088/1361-6668/aa70d3
- [114] HORIDE, Tomoya ; ISHIMARU, Manabu ; MATSUMOTO, Kaname: Observation of inhomogeneous depinning in $\text{YBa}_2\text{Cu}_3\text{O}_7$ composite multilayers. In: *Superconductor Science and Technology* 32 (2019), jun, Nr. 8, S. 085001. <http://dx.doi.org/10.1088/1361-6668/ab1d2c>. – DOI 10.1088/1361-6668/ab1d2c
- [115] FIGUERAS, J. ; PUIG, T. ; OBRADORS, X. ; KWOK, W. K. ; PAULIUS, L. ; CRABTREE, G. W. ; DEUTSCHER, G.: The loss of vortex line tension sets an upper limit to the irreversibility line in $\text{YBa}_2\text{Cu}_3\text{O}_7$. In: *Nature Physics* 2 (2006), may, Nr. 6, S. 402–407. <http://dx.doi.org/10.1038/nphys311>. – DOI 10.1038/nphys311
- [116] DOU, S. X. ; BRACCINI, V. ; SOLTANIAN, S. ; KLIE, R. ; ZHU, Y. ; LI, S. ; WANG, X. L. ; LARBALESTIER, D.: Nanoscale-SiC doping for enhancing J_c and H_{c2} in superconducting MgB_2 . In: *Journal of Applied Physics* 96 (2004), dec, Nr. 12, S. 7549–7555. <http://dx.doi.org/10.1063/1.1814415>. – DOI 10.1063/1.1814415
- [117] GLATZ, Andreas ; SADOVSKYY, Ivan A. ; WELP, Ulrich ; KWOK, Wai-Kwong ; CRABTREE, George W.: The Quest for High Critical Current in Applied High-Temperature Superconductors. In: *Journal of Superconductivity and Novel Magnetism* 33 (2019), sep, Nr. 1, S. 127–141. <http://dx.doi.org/10.1007/s10948-019-05255-w>. – DOI 10.1007/s10948-019-05255-w
- [118] WILLA, R. ; KOSHELEV, A. E. ; SADOVSKYY, I. A. ; GLATZ, A.: Strong-pinning regimes by spherical inclusions in anisotropic type-II superconductors. In: *Supercond. Sci. Technol.* 31 (2017), November, Nr. 1. <https://doi.org/10.1088/1361-6668/aa939e>
-

- [119] BEAN, C. P.: Magnetization of High-Field Superconductors. In: *Reviews of Modern Physics* 36 (1964), jan, Nr. 1, S. 31–39. <http://dx.doi.org/10.1103/revmodphys.36.31>. – DOI 10.1103/revmodphys.36.31
- [120] ENGELMANN, J. ; IIDA, K. ; KURTH, F. ; BEHLER, C. ; OSWALD, S. ; HÜHNE, R. ; HOLZAPFEL, B. ; SCHULTZ, L. ; HAINDL, S.: Fe/Ba(Fe_{1-x}Co_x)₂As₂ multilayers and quasi-multilayers with T_c=29K. In: *Physica C: Superconductivity* 494 (2013), nov, S. 185–188. <http://dx.doi.org/10.1016/j.physc.2013.04.014>. – DOI 10.1016/j.physc.2013.04.014
- [121] BEEK, C J. d. ; KONCZYKOWSKI, M ; PROZOROV, R: Anisotropy of strong pinning in multi-band superconductors. In: *Superconductor Science and Technology* 25 (2012), jul, Nr. 8, S. 084010. <http://dx.doi.org/10.1088/0953-2048/25/8/084010>. – DOI 10.1088/0953-2048/25/8/084010
- [122] MALMIVIRTA, Mika ; RIJCKAERT, Hannes ; PAASONEN, Ville ; HUHTINEN, Hannu ; HYNINEN, Teemu ; JHA, Rajveer ; AWANA, Veerpal S. ; DRIESSCHE, Isabel V. ; PATURI, Petriina: Enhanced flux pinning in YBCO multilayer films with BCO nanodots and segmented BZO nanorods. In: *Scientific Reports* 7 (2017), oct, Nr. 1. <http://dx.doi.org/10.1038/s41598-017-13758-6>. – DOI 10.1038/s41598-017-13758-6
- [123] YAMASAKI, H ; OHKI, K ; YAMADA, H ; NAKAGAWA, Y ; MAWATARI, Y: Strong flux pinning in YBa₂Cu₃O_{7-δ} thin films due to nanometer-sized precipitates. In: *Superconductor Science and Technology* 21 (2008), oct, Nr. 12, S. 125011. <http://dx.doi.org/10.1088/0953-2048/21/12/125011>. – DOI 10.1088/0953-2048/21/12/125011
- [124] CANFIELD, Paul C. ; BUD'KO, Sergey L.: FeAs-Based Superconductivity: A Case Study of the Effects of Transition Metal Doping on BaFe₂As₂. In: *Annual Review of Condensed Matter Physics* 1 (2010), S. 27–50. <http://dx.doi.org/10.1146/annurev-conmatphys-070909-104041>. – DOI 10.1146/annurev-conmatphys-070909-104041
- [125] COLOMBIER, E. ; TORIKACHVILI, M. S. ; NI, N. ; THALER, A. ; BUDKO, S. L. ; CANFIELD, P. C.: Electrical transport measurements under pressure for BaFe₂As₂ compounds doped with Co, Cr, or Sn. In: *Superconductor Science and Technology* 23 (2010), Nr. 054003. <http://dx.doi.org/10.1088/0953-2048/23/5/054003>. – DOI 10.1088/0953-2048/23/5/054003
- [126] ELEY, S. ; MIURA, M. ; MAIOROV, B. ; CIVALE, L.: Universal Lower Limit on Vortex Creep in Superconductors. In: *Nature Materials* 16 (2016), S. 409–413. <http://dx.doi.org/10.1038/nmat4840>. – DOI 10.1038/nmat4840

-
- [127] FANG, Lei ; LUO, Huiqian ; CHENG, Peng ; WANG, Zhaosheng ; JIA, Ying ; MU, Gang ; SHEN, Bing ; MAZIN, I. I. ; SHAN, Lei ; REN, Cong ; WEN, Hai-Hu: Roles of multiband effects and electron-hole asymmetry in the superconductivity and normal-state properties of $\text{Ba}(\text{Fe}_{1-x}\text{Co}_x)_2\text{As}_2$. In: *Physical Review B* 80 (2009), Nr. 140508. <http://dx.doi.org/10.1103/PhysRevB.80.140508>. – DOI 10.1103/PhysRevB.80.140508
- [128] GARITEZI, T. M. ; ROSA, P. F. S. ; ADRIANO, C. ; PAGLIUSO, P. G.: Transport critical current measurements on a Cu-substituted BaFe_2As_2 superconductor. In: *Journal of Applied Physics* 115 (2014), Nr. 17D704. <http://dx.doi.org/10.1063/1.4862525>. – DOI 10.1063/1.4862525
- [129] GHORBANI, S. R. ; WANG, X. L. ; SHABAZI, M. ; DOU, S. X. ; CHOI, K. Y. ; LIN, C. T.: Flux pinning and vortex transitions in doped BaFe_2As_2 single crystals. In: *Applied Physics Letters* 100 (2012), Nr. 072603. <http://dx.doi.org/10.1063/1.3685507>. – DOI 10.1063/1.3685507
- [130] IIDA, Kazumasa ; GRINENKO, Vadim ; KURTH, Fritz ; ICHINOSE, Ataru ; TSUKADA, Ichiro ; AHRENS, Eike ; PUKENAS, Aurimas ; CHEKHONIN, Paul ; SKROTZKI, Werner ; TERESIAK, Angelika ; HÜHNE, Ruben ; ASWARTHAM, Saicharan ; WURMEHL, Sabine ; MÖNCH, Ingolf ; ERBE, Manuela ; HÄNISCH, Jens ; HOLZAPFEL, Bernhard ; DRECHSLER, Stefan-Ludwig ; ; EFREMOV, Dmitri V.: Hall-plot of the phase diagram for $\text{Ba}(\text{Fe}_{1-x}\text{Co}_x)_2\text{As}_2$. In: *Scientific Reports* 6 (2016), June, Nr. 28390. <http://dx.doi.org/10.1038/srep28390>. – DOI 10.1038/srep28390
- [131] KANO, Mika ; KOHAMA, Yoshimitsu ; GRAF, David ; BALAKIREV, Fedor ; SEFAT, Athena S. ; MCGUIRE, Michael A. ; SALES, Brian C. ; MANDRUS, David ; TOZER, Stanley W.: Anisotropy of the Upper Critical Field in a Co-Doped BaFe_2As_2 Single Crystal. In: *Journal of the Physical Society of Japan* 78 (2009), Nr. 8. <http://dx.doi.org/10.1143/JPSJ.78.084719>. – DOI 10.1143/JPSJ.78.084719
- [132] KITAGAWA, Kentaro ; KATAYAMA, Naoyuki ; OHGUSHI, Kenya ; YOSHIDA, Makoto ; TAKIGAWA, Masashi: Commensurate Itinerant Antiferromagnetism in BaFe_2As_2 : ^{75}As -NMR Studies on a Self-Flux Grown Single Crystal. In: *Journal of the Physical Society of Japan* 77 (2008), Nr. 11. <http://dx.doi.org/10.1143/JPSJ.77.114709>. – DOI 10.1143/JPSJ.77.114709
- [133] KOSHELEV, A. E. ; KOLTON, A. B.: Theory and simulations on strong pinning of vortex lines by nanoparticles. In: *Physical Review B* 84 (2011), September, Nr. 104528. <http://dx.doi.org/10.1103/PhysRevB.84.104528>. – DOI 10.1103/PhysRevB.84.104528
- [134] MAIOROV, Boris: Combination of correlated and point-like pinning in low
-

- anisotropy $\text{Ba}(\text{Fe}_{1-x}\text{Co}_x)_2\text{As}_2$ thin films. In: *APS Meeting Boston* Los Alamos National Laboratory, 2012
- [135] MAIOROV, B. ; KATASE, T. ; USOV, I. O. ; WEIGAND, M. ; CIVALE, L. ; HIRAMATSU, H. ; HOSONO, H.: Competition and cooperation of pinning by extrinsic point-like defects and intrinsic strong columnar defects in BaFe_2As_2 thin films. In: *Physical Review B: Condensed Matter and Materials Physics* 86 (2012), Nr. 094513. <http://dx.doi.org/10.1103/PhysRevB.86.094513>. – DOI 10.1103/PhysRevB.86.094513
- [136] MISHEV, V. ; SEEBÖCK, W. ; EISTERER, M. ; IIDA, K. ; KURTH, F. ; HÄNISCH, J. ; REICH, E. ; HOLZAPFEL, B.: One-dimensional pinning behavior in Co-doped BaFe_2As_2 thin films. In: *Applied Physics Letters* 103 (2013), Nr. 232601. <http://dx.doi.org/10.1063/1.4838039>. – DOI 10.1063/1.4838039
- [137] NAKAJIMA, Yasuyuki ; TAEN, Toshihiro ; TAMEGAI, Tsuyoshi: Possible Superconductivity above 25K in Single-Crystalline Co-Doped BaFe_2As_2 . In: *Journal of the Physical Society of Japan* 78 (2009), Nr. 2. <http://dx.doi.org/10.1143/JPSJ.78.023702>. – DOI 10.1143/JPSJ.78.023702
- [138] NI, N. ; BUDKO, S. L. ; KREYSSIG, A. ; NANDI, S. ; RUSTAN, G. E. ; GOLDMAN, A. I. ; GUPTA, S. ; CORBETT, J. D. ; KRACHER, A. ; CANFIELD, P. C.: Anisotropic thermodynamic and transport properties of single-crystalline $\text{Ba}_{1-x}\text{K}_x\text{Fe}_2\text{As}_2$ ($x=0$ and 0.45). In: *Physical Review B* 78 (2008), Nr. 014507. <http://dx.doi.org/10.1103/PhysRevB.78.014507>. – DOI 10.1103/PhysRevB.78.014507
- [139] PAGLIONE, Johnpierre ; GREENE, Richard L.: High-temperature superconductivity in iron-based materials. In: *Nature Physics* 6 (2010), S. 645–658. <http://dx.doi.org/10.1038/nphys1759>. – DOI 10.1038/nphys1759
- [140] PERVAKOV, K. S. ; VLASENKO, V. A. ; KHLYBOV, E. P. ; ZALESKI, A. ; PUDALOV, V. M. ; ELTSEV, Yu F.: Bulk magnetization and strong intrinsic pinning in Ni-doped BaFe_2As_2 single crystals. In: *Superconductor Science and Technology* 26 (2013), Nr. 015008. <http://dx.doi.org/10.1088/0953-2048/26/1/015008>. – DOI 10.1088/0953-2048/26/1/015008
- [141] SATO, Hikaru ; HIRAMATSU, Hidenori ; KAMIYA, Toshio ; HOSONO, Hideo: Enhanced critical-current in P-doped BaFe_2As_2 thin films on metal substrates arising from poorly aligned grain boundaries. In: *Scientific Reports* 6 (2016), Nr. 36828. <http://dx.doi.org/10.1038/srep36828>. – DOI 10.1038/srep36828
- [142] SATO, Hikaru ; HIRAMATSU, Hidenori ; KAMIYA, Toshio ; HOSONO, Hideo: Vortex Pinning Properties of Phosphorous-Doped BaFe_2As_2 Epitaxial Films: Compari-

-
- son Between (La, Sr)(Al, Ta)O₃ and MgO Substrates. In: *IEEE Transactions on Applied Superconductivity* 25 (2015), Nr. 3
- [143] SHAHBAZI, M. ; WANG, X. L. ; LIN, Z. W. ; ZHU, J. G. ; DOU, S. X. ; CHOI, K. Y.: Magnetoresistance, critical current density, and magnetic flux pinning mechanism in nickel doped BaFe₂As₂ single crystals. In: *Journal of Applied Physics* 109 (2011), Nr. 07E151. <http://dx.doi.org/10.1063/1.3563057>. – DOI 10.1063/1.3563057
- [144] SUN, D. L. ; LIU, Y. ; LIN, C. T.: Comparative study of upper critical field H_{c2} and second magnetization peak H_{sp} in hole- and electron-doped BaFe₂As₂ superconductor. In: *Physical Review B* 80 (2009), Nr. 144515. <http://dx.doi.org/10.1103/PhysRevB.80.144515>. – DOI 10.1103/PhysRevB.80.144515
- [145] TARANTINI, C. ; LEE, S. ; KAMETANI, F. ; JIANG, J. ; WEISS, J. D. ; JAROSZYNSKI, J. ; FOLKMAN, C. M. ; HELLSTROM, E. E. ; EOM, C. B. ; LARBALESTIER, D. C.: Artificial and self-assembled pinning centers in Ba(Fe_{1-x}Co_x)₂As₂ thin films as a route to very high current density. In: *Physical Review B* 86 (2012), Nr. 214504. <http://dx.doi.org/10.1103/PhysRevB.86.214504>. – DOI 10.1103/PhysRevB.86.214504
- [146] TARANTINI, C. ; LEE, S. ; ZHANG, Y. ; JIANG, J. ; BARK, C. W. ; WEISS, J. D. ; POLYANSKII, A. ; NELSON, C. T. ; JANG, H. W. ; FOLKMAN, C. M. ; BAEK, S. H. ; PAN, X. Q. ; GUREVICH, A. ; HELLSTROM, E. E. ; EOM, C. B. ; LARBALESTIER, D. C.: Strong vortex pinning in Co-doped BaFe₂As₂ single crystal thin films. In: *Applied Physics Letters* 96 (2010), Nr. 142510. <http://dx.doi.org/10.1063/1.3383237>. – DOI 10.1063/1.3383237
- [147] VINOD, K. ; SHARMA, Shilpam ; SATYA, A. T. ; SUNDAR, C. S. ; BHARATHI, A.: High intrinsic flux pinning strength of BaFe_(2-x)Co_xAs₂ superconductor. In: *Condensed Matter Physics Division* (2011). https://www.researchgate.net/publication/51917970_High_intrinsic_flux_pinning_strength_of_BaFe2-xCoxAs2_superconductor
- [148] WANG, X. F. ; WU, T. ; WU, G. ; CHEN, H. ; XIE, Y. L. ; YING, J. J. ; YAN, Y. J. ; LIU, R. H. ; CHEN, X. H.: Anisotropy in the Electrical Resistivity and Susceptibility of Superconducting BaFe₂As₂ Single Crystals. In: *Physical Review Letters* 102 (2009), Nr. 117005. <http://dx.doi.org/10.1103/PhysRevLett.102.117005>. – DOI 10.1103/PhysRevLett.102.117005
- [149] WANG, Xiao-Lin ; GHORBANI, S. R. ; LEE, Sung-Ik ; DOU, S. X. ; LIN, C. T. ; JOHANSEN, T. H. ; MÜLLER, K.-H. ; CHENG, Z. X. ; PELECKIS, G. ; SHABAZI, M. ; QVILLER, A. J. ; YURCHENKO, V. V. ; SUN, G. L. ; SUN, D. L.: Very strong intrinsic flux pinning and vortex avalanches in (Ba,K)Fe₂As₂ superconducting
-

- single crystals. In: *Physical Review B* 82 (2010), Nr. 024525. <http://dx.doi.org/10.1103/PhysRevB.82.024525>. – DOI 10.1103/PhysRevB.82.024525
- [150] YAMAMOTO, A. ; JAROSZYNSKI, J. ; TARANTINI, C. ; BALICAS, L. ; JIANG, J. ; GUREVICH, A. ; LARBALESTIER, D. C. ; JIN, R. ; SEFAT, A. S. ; MCGUIRE, M. A. ; SALES, B. C. ; CHRISTEN, D. K. ; MANDRUS, D.: Small anisotropy, weak thermal fluctuations, and high field superconductivity in Co-doped iron pnictide $\text{Ba}(\text{Fe}_{(1-x)}\text{Co}_x)_2\text{As}_2$. In: *Applied Physics Letters* 94 (2009), Nr. 062511. <http://dx.doi.org/10.1063/1.3081455>. – DOI 10.1063/1.3081455
- [151] ZABOLOTNYY, V. B. ; INOSOV, D. S. ; EVTUSHINSKY, D. V. ; KOITZSCH, A. ; KORDYUK, A. A. ; SUN, G. L. ; PARK, J. T. ; HAUG, D. ; HINKOV, V. ; BORIS, A. V. ; LIN, C. T. ; KNUPFER, M. ; YARESKO, A. N. ; BÜCHNER, B. ; VARYKHALOV, A. ; FOLLATH, R. ; BORISENKO, S. V.: $((\pi, \pi))$ electronic order in iron arsenide superconductors. In: *Nature* 457 (2009), S. 569–572. <http://dx.doi.org/10.1038/nature07714>. – DOI 10.1038/nature07714
- [152] ZHANG, Yi ; NELSON, Christopher T. ; LEE, Sanghan ; JIANG, Jianyi ; BARK, Chung W. ; WEISS, Jeremy D. ; TARANTINI, Chiara ; FOLKMAN, Chad M. ; BAEK, Seung-Hyub ; HELLSTROM, Eric E. ; LARBALESTIER, David C. ; EOM, Chang-Beom ; PAN, Xiaoqing: Self-assembled oxide nanopillars in epitaxial BaFe_2As_2 thin films for vortex pinning. In: *Applied Physics Letters* 98 (2011), Nr. 042509. <http://dx.doi.org/10.1063/1.3532107>. – DOI 10.1063/1.3532107
- [153] BARDEEN, J. ; COOPER, L. N. ; SCHRIEFFER, J. R.: Theory of Superconductivity. In: *Phys. Rev.* 108 (1957), Dec, 1175-1204. <http://dx.doi.org/10.1103/PhysRev.108.1175>. – DOI 10.1103/PhysRev.108.1175
- [154] OHM, G. S.: Vorläufige Anzeige des Gesetzes, nach welchen Metalle die Contactelektricität leiten sowie Späterer Nachtrag. In: *J. C. Poggendorff (Hrsg.) Annalen der Physik und Chemie* 80 (1825), S. 79–88
- [155] MIURA, Masashi ; ADACHI, Seiji ; SHIMODE, Takashi ; WADA, Keisuke ; TAKEMORI, Akira ; CHIKUMOTO, Noriko ; NAKAO, Koichi ; TANABE, Keiichi: Anisotropy and Superconducting Properties of $\text{BaFe}_2(\text{As}_{1-x}\text{P}_x)_2$ Films with Various Phosphorus Contents. In: *Applied Physics Express* 6 (2013), sep, Nr. 9, S. 093101. <http://dx.doi.org/10.7567/apex.6.093101>. – DOI 10.7567/apex.6.093101
- [156] CENTRAL JAPAN RAILWAY COMPANY: -. -. CentralJapanRailwayCompany. Version: 30th of august 2020

Danksagung

Ich möchte an dieser Stelle allen danken, die es mir ermöglicht haben diese Arbeit zu verfassen. Zu allererst bedanke ich mich bei Prof. Dr. Bernhard Holzapfel, der mir die Chance gegeben hat meine Doktorarbeit und die Experimente, welche zu dieser Arbeit führten, durchzuführen, sowie für seine Hilfe, Ratschläge und seinen Zuspruch.

Ich bedanke mich bei meinem Gruppenleiter Herrn Doktor Jens Hänisch, der mich mit viel Geduld vieles gelehrt und mich maßgeblich bei dieser Arbeit unterstützt hat. Ich bin sehr dankbar dafür, dass ich viele Ideen, sowohl technisch als auch experimentell, umsetzen durfte. Durch den gemeinsamen Austausch habe ich viel gelernt und nehme viele bereichernde Erfahrungen mit.

Ich bedanke mich bei allen Mitgliedern der SuSchi-Gruppe für die Unterstützung. Vielen Dank an meine Mitdoktoranden und Arbeitskollegen für die vielen tollen Gespräche und die lehrreiche Zeit. Eure Erfahrungen und Anregungen waren mir immer eine willkommene Hilfe.

Ich danke Nico Beisig für seine Beiträge und bin stolz dein Betreuer gewesen zu sein.

Vielen Dank an Hannes Rijkaert, Lukas Grünewald und Thomas Bergfeldt für ihre Messungen und Input zu Messergebnissen.

Vielen Dank an Kazumasa Iida für die tollen und lehrreichen Gespräche bei den Messzeiten.

Ich bedanke mich ganz besonders bei meiner Frau Grace Muraa für ihre Geduld, Ermutigung und Unterstützung zu jedem Zeitpunkt. Ohne dich wäre all das niemals möglich gewesen! Du hast auf so viele Sachen verzichtet, damit ich diese Arbeit fertigstellen kann.

Ein großer Dank geht auch an meine Eltern, für ihre Unterstützung.

Diese Arbeit wurde teilweise gefördert durch die Deutsche Forschungsgemeinschaft (DFG) - Projektnummer 410414581.

This work was partially funded by Deutsche Forschungsgemeinschaft (DFG) - project number 410414581.

Hiermit versichere ich, dass ich diese Arbeit mit dem Titel „Introduction of quasi-multilayer pulsed laser deposition for enhanced superconducting properties of $\text{Ba}(\text{Fe}_{0.92}\text{Co}_{0.08})_2\text{As}_2$ thin films” eigenständig und nur unter der Verwendung der angegebenen Hilfsmittel und Quellen angefertigt habe. Alle Stellen, die wörtlich oder sinngemäß aus anderen Schriften entnommen sind, habe ich als solche kenntlich gemacht.

Mannheim, den 14.10.2020

